UHECR FLUX FROM SHDM ANNIHILATION IN GC-LIKE SUBSTRUCTURES

A Thesis Submitted to the College of
Graduate Studies and Research
in Partial Fulfilment of the Requirements
for the degree of Master of Science
in the Department of Physics
and Engineering Physics
at the University of Saskatchewan

By
Kai Erik Wunderle

Permission to Use

In presenting this thesis in partial fulfilment of the requirements for a Postgraduate degree from the University of Saskatchewan, I agree that the Libraries of this University may make it freely available for inspection. I further agree that permission for copying of this thesis in any manner, in whole or in part, for scholarly purposes may be granted by the professor or professors who supervised my thesis work or, in their absence, by the Head of the Department or the Dean of the College in which my thesis work was done. It is understood that any copying or publication or use of this thesis or parts thereof for financial gain shall not be allowed without my written permission. It is also understood that due recognition shall be given to me and to the University of Saskatchewan in any scholarly use which may be made of any material in my thesis.

Requests for permission to copy or to make other use of material in this thesis in whole or part should be addressed to:

Head of the Department of Physics and Engineering Physics
162 Physics Building
116 Science Place
University of Saskatchewan
Saskatoon, Saskatchewan S7N 5E2
Canada

Abstract

The objective of this thesis is to outline a relation between the measured Ultra High Energy Cosmic Ray (UHECR) flux and theoretical models for Super Heavy Dark Matter (SHDM) annihilation in Globular Cluster (GC)-like substructures in our Galaxy. Thus a possible solution for these two puzzling phenomena in present day astroparticle physics is presented.

A possible connection between GC-like substructures and UHECR sources was identified by combining the theoretical results for the annihilation of SHDM with the core densities derived from Dark Matter (DM)-profile fits to the GC data by Harris.

The annihilation fluxes were derived for the Navarro, Frenk, and White-profile, the Moore-profile and a new constant density core approach. To compute the core densities of the GC-like substructures the GC-data by Harris were fitted to the most commonly used DM-profiles as well as to a more general DM-profile with variable inner power law index. The core densities were then calculated by making assumptions on the distribution of the masses in the GC-like substructure system as well as on the relation between the substructure mass and the core density.

Numerical simulations for the constant density core approach show that it is possible to reproduce the amount of substructure of the GC system of our Galaxy by choosing the mass fraction of the clumped dark matter to $\xi = 0.1$ and the fraction of the heaviest substructure to $\eta = 0.01\xi$, which corresponds to a mass of $10^9\, M_\odot$ for the most massive substructure. These simulation parameters then predict a product of the s-wave unitary bound with the fraction of the density of the Sun of $\zeta\nu \approx 10^{-4}$. Fits of the GC data to the DM-profiles reveal that all commonly used DM-profiles have to be rejected. Instead the profile with variable inner power law index is in good agreement with the GC data. The core densities are then calculated to range from $10^2\, M_\odot \mathrm{pc}^{-3}$ to $10^8\, M_\odot \mathrm{pc}^{-3}$.

Therfore it can be concluded that SHDM annihilation in GC-like subclumps in our Galaxy presents a promising possibility to explain the measured UHECR flux.

Acknowledgements

I am indebted to my supervisor R. Dick for his help and advice throughout my whole time in the Masters program as well as for proof-reading the final thesis. In addition I greatfully acknowledge having drawn from his previous work on decay and annihilation of SHDM with a NFW-profile. I also would like to thank the graduate students K.M. Hopp and D. Janzen for constructive discussions on the topic. Finally, I want to thank C.E. Soteros, T.G. Steele, K. Tanaka, and C. Xiao for their invaluable remarks and suggestions.

The thesis is supported by NSERC Canada, two University Graduate Scholarships and a William Rowles Fellowship.

Dedication

To my wife and my family.

Contents

Permission to Use i

Abstract ii

Acknowledgements iii

Dedication iv

Contents v

List of Figures vii

List of Tables xi

List of Abbreviations xii

1 Introduction 1

1.1 Ultra High Energy Cosmic Ray 2
1.2 Density Profiles 3
1.3 Dark Matter Candidates 6
1.4 The Greisen-Zatsepin-Kuzmin Cutoff 7
1.5 Globular Cluster 9

2 Ultra High Energy Cosmic Ray Flux From Superheavy Dark Matter 13

2.1 Navarro, Frenk, and White-Profile 18
2.2 Moore-Profile 21
2.3 Subclumps with Constant Density Core 24
2.4 Simulation Results 26

3 DM-Profile for Globular Clusters 30

3.1 Navarro, Frenk, and White-profile with core 32
3.2 Moore-profile with core 36
3.3 King-profile 39
3.4 Isothermal profile with core 42
3.5 Navarro, Frenk, and White-profile 45

3.6 Moore-profile 47
3.7 Conclusions 49

4 Profile with Variable α 51

5 Core Density of Globular Clusters 56
5.1 Gaussian Mass Distribution 59
5.1.1 Core Density from Structure Parameter δ 60
5.1.2 Core Density from M/L-ratio 62
5.2 Power Law Distribution 63
5.2.1 Core Density from Structure Parameter δ 66
5.2.2 Core Density from M/L-ratio 68
5.3 Conclusion 68

6 Final Results 70

A Greisen-Zatsepin-Kuzmin Cutoff 72

B Navarro, Frenk, and White-Profile 74

C Moore-Profile 102

D Constant Density Subclumps 106

List of Figures

1.1 Comparison of dark matter densities. The graph shows the common logarithm of the dark matter density for different commonly used dark matter profiles over the distance from the center of the distribution. . 3

1.2 Distances of the Globular Clusters from the Sun. The histogram plot displays the number of Globular Clusters over the distance from the Sun in kpc. A bin contains all Globular Clusters with a distance from the Sun of $r_{\min} \leq r < r_{\max}$. 10

1.3 Core radii of the Globular Clusters. The histogram plot displays the number of Globular Clusters over the core radius d_c of the Globular Cluster in pc. A bin contains all Globular Clusters with a core radius of $d_{\min} \leq d_c < d_{\max}$. 11

1.4 Tidal Radii of the Globular Clusters. The histogram plot displays the number of Globular Clusters over the tidal radius d_t of the Globular Cluster in pc. A bin contains all Globular Clusters with a tidal radius of $d_{\min} \leq d_t < d_{\max}$. 12

2.1 Number of subclumps in simulated galaxy 2D (low resolution). The graph shows the number of subclumps in a simulated galaxy over the ratio ξ/η together with a linear fit to the simulation results. The range of the parameters in the simulation was defined to be $0.001 \leq \xi \leq 0.1$ and $0.01\xi \leq \eta \leq \xi$. 27

2.2 Number of subclumps in simulated galaxy 1D (high resolution). The graph displays the number of subclumps in a simulated galaxy over the ratio ξ/η. The parameter $\xi = 0.1$ was chosen to be constant while η was varied within a range of $0.001\xi \leq \eta \leq \xi$. 28

2.3 $\zeta\nu$ in simulated galaxies. The graph displays the product $\zeta\nu$ over the ratio ξ/η for a range of $5 \leq \xi/\eta \leq 100$. The parameter $\xi = 0.1$ was chosen to be constant while the fraction of the heaviest subclump was varied between $0.001\xi \leq \eta \leq \xi$. 29

3.1 Relationships between d_h and d_t for the NFW-profile with core for the case $d_h \leq d_c$. The three lines represent numerical solutions to equation (3.9, I) for $d_s = 0$ (solid, lower line), $d_s = d_c$ (dotted, middle line), and $d_s = d_t$ (dashed, upper line). The points display the measured relations for the Globular Clusters. 33
3.2 Relationships between d_h and d_t for the NFW-profile with core for the case $d_h > d_c$. The three lines represent numerical solutions to equation (3.9, II) for $d_s = 0$ (solid, lower line), $d_s = d_c$ (dotted, middle line), and $d_s = d_t$ (dashed, upper line). The points display the measured relations for the Globular Clusters. 34
3.3 Relationships between d_h and d_t for the Moore-profile with core for the case $d_h \leq d_c$. The three lines represent numerical solutions to equation (3.9, I) for $d_s = 0$ (solid, lower line), $d_s = d_c$ (dotted, middle line), and $d_s = d_t$ (dashed, upper line). The points display the measured relations for the Globular Clusters. 37
3.4 Relationships between d_h and d_t for the Moore-profile with core for the case $d_h \leq d_c$. The three lines represent numerical solutions to equation (3.9, II) for $d_s = 0$ (solid, lower line), $d_s = d_c$ (dotted, middle line), and $d_s = d_t$ (dashed, upper line). The points display the measured relations for the Globular Clusters. 38
3.5 Relationship between d_h and d_t for the King-profile. The solid line represents the numerical solution to equation (3.22). The points display the measured relations for the Globular Clusters. 40
3.6 Relationship between d_h and d_t for the isothermal profile with core for the case $d_h \leq d_c$. The line represents the numerical solutions to equation (3.26, I). The points display the measured relations for the Globular Clusters. 42
3.7 Relationship between d_h and d_t for the isothermal profile with core for the case $d_h > d_c$. The line represents the numerical solutions to equation (3.26, II). The points display the measured relations for the Globular Clusters. 43
3.8 Relationships between d_h and d_t for the NFW-profile. The two lines represent numerical solutions to equation (3.31) for $d_s = d_c$ (dotted, lower line) and $d_s = d_t$ (dashed, upper line). The points display the measured relations for the Globular Clusters. 45

3.9 Relationship between d_h and d_t for the Moore-profile. The two lines represent numerical solutions to equation (3.37) for $d_s = d_c$ (dotted, lower line) and $d_s = d_t$ (dashed, upper line). The points display the measured relations for the Globular Clusters. 48

4.1 Averaged inner power law index of the Globular Clusters. The histogram plot shows the number of Globular Clusters over the averaged inner power law index. A bin contains all Globular Clusters with an averaged inner power law index of $\alpha_{\min} \leq \alpha < \alpha_{\max}$. 54
4.2 Scale radius of the Globular Clusters. The histogram plot shows the number of Globular Clusters over the scale radius in units of the core radius. A bin contains all Globular Clusters with a scale radius of $d_{\min} \leq d_s < d_{\max}$. 55

5.1 Normalised Gaussian mass distribution. The graph shows the normalised Gaussian mass distribution for the first Globular Cluster of the Harris catalogue. It represents the possibility of the Globular Cluster having a certain mass over the mass in units of $10^6\,M_\odot$. . . . 57
5.2 Number distribution for the Globular Cluster system in our Galaxy. The histogram plot displays the number of Globular Clusters in our Galaxy that can be expected to be in a certain mass range in units of $10^6\,M_\odot$. Each bin represents the expected number of Globular Clusters within its range $M_{\min} \leq M_{\rm GC} < M_{\max}$. 58
5.3 Number of Globular Clusters over the core density from structure parameter. The histogram plot displays the number of Globular Clusters over the common logarithm of the core density in units of $M_\odot \mathrm{pc}^{-3}$ as derived from the structure parameter δ. Each bin represents the expected number of Globular Clusters within its range $\rho_{\min} \leq \rho < \rho_{\max}$. 61
5.4 Number of Globular Clusters over the core density from M/L-ratio. The histogram plot displays the number of Globular Clusters over the common logarithm of the core density in units of $M_\odot \mathrm{pc}^{-3}$ as derived from the M/L-ratio. Each bin represents the expected number of Globular Clusters within its range $\rho_{\min} \leq \rho < \rho_{\max}$. 62
5.5 Normalised power law mass distribution. The graph shows the normalised power law mass distribution for the first Globular Cluster of the Harris catalogue. It represents the possibility of the Globular Cluster having a certain mass over the mass in units of $10^6\,M_\odot$. . . . 64

5.6 Number distribution for the Globular Cluster system in our Galaxy. The histogram plot displays the number of Globular Clusters in our Galaxy that can be expected to be in a certain mass range in units of $10^6\,M_\odot$. Each bin represents the expected number of Globular Clusters within its range $M_{\min} \leq M_{\mathrm{GC}} < M_{\max}$. 65

5.7 Number of Globular Clusters over the core density from structure parameter. The histogram plot displays the number of Globular Clusters over the common logarithm of the core density in units of $M_\odot \mathrm{pc}^{-3}$ as derived from the structure parameter δ. Each bin represents the expected number of Globular Clusters within its range $\rho_{\min} \leq \rho < \rho_{\max}$. 66

5.8 Number of Globular Clusters over the core density from M/L-ratio. The histogram plot displays the number of Globular Clusters over the common logarithm of the core density in units of $M_\odot \mathrm{pc}^{-3}$ as derived from the M/L-ratio. Each bin represents the expected number of Globular Clusters within its range $\rho_{\min} \leq \rho < \rho_{\max}$. 67

List of Tables

3.1 Half mass radii and tidal radii for the NFW-profile with constant density core. The table summarises numerical results for the half mass radius from equation (Ia), (Ib), (IIa), and (IIb) for a range of values for the tidal radius. All radii are normalised to units of the core radius. 35

3.2 Half mass radii and tidal radii for the Moore-profile with constant density core. The table summarises numerical results for the half mass radius from equation (Ia), (Ib), (IIa), and (IIb) for a range of values for the tidal radius. All radii are normalised to units of the core radius. 36

3.3 Half mass radii and tidal radii for the King-profile. The table summarises numerical results for the half mass radius for a range of values for the tidal radius. All radii are normalised to units of the core radius. 41

3.4 Half mass radii and tidal radii for the isothermal profile with constant density core. The table summarises numerical results for the half mass radius from equation (I) and (II) for a range of values for the tidal radius. All radii are normalised to units of the core radius. 44

3.5 Half mass radii and tidal radii for the NFW-profile. The table summarises numerical results for the half mass radius from equation (a) and (b) for a range of values for the tidal radius. All radii are normalised to units of the core radius. 47

3.6 Half mass radii and tidal radii for the Moore-profile. The table summarises numerical results for the half mass radius from equation (a) and (b) for a range of values for the tidal radius. All radii are normalised to units of the core radius. 49

List of Abbreviations

AGASA	-	Akeno Giant Air Shower Array
CDM	-	Cold Dark Matter
CMB	-	Cosmic Microwave Background
DM	-	Dark Matter
GC	-	Globular Cluster
GZK cutoff	-	Greisen-Zatsepin-Kuzmin cutoff
HiRes	-	High Resolution Fly's Eye
IMBH	-	Intermediate Mass Black Hole
LSP	-	Lightest Supersymmetric Particle
ly	-	light-year ($1\,\mathrm{ly} = 0.3066\,\mathrm{pc} = 9.4605 \cdot 10^{15}\,\mathrm{m}$)
M/L-ratio	-	Mass to Light ratio
MSSM	-	Minimal Supersymmetric extension of the Standard Model
MW	-	Milky Way
NC	-	Nuclear Cluster
NFW-profile	-	Navarro, Frenk, and White-profile
pc	-	parsec ($1\,\mathrm{pc} = 3.262\,\mathrm{ly} = 3.0857 \cdot 10^{16}\,\mathrm{m}$)
SHDM	-	Super Heavy Dark Matter
SUGAR	-	Sydney University Giant Air Shower Recorder
UHECR	-	Ultra High Energy Cosmic Ray
WIMP	-	Weakly Interacting Massive Particle
WMAP	-	Wilkinson Microwave Anisotropy Probe

Chapter 1

Introduction

One of the most puzzling phenomena in present day astroparticle physics is the detection of Ultra High Energy Cosmic Rays (UHECRs) that exceed the expected cutoff energy given by the Greisen-Zatsepin-Kuzmin (GZK) cutoff. These particles contradict all currently accepted models for standard generation of cosmic rays.

Since the first detection of UHECRs took place during the Volcano Ranch experiment between 1959 and 1976, every major experiment, including AGASA, HiRes and Fly's Eye, detected UHECRs.

Detections of UHECRs have become even more mysterious because their origin has to be within a radius of 100 Mpc around Earth based on the GZK cutoff condition. It thus should be possible to detect their sources. However, it has been impossible to find an unambiguous connection between the detected UHECRs and astronomical sources in our direct neighbourhood such as black holes, active galactic nuclei, neutron stars or more exotic sources like magnetars. Although the AGASA collaboration claims to have noted a clustering they were not able to locate specific sources in these directions.

This motivated different yet promising explanations that involved decaying or annihilating superheavy dark matter (SHDM) particles. In the decay scenarios these particles must have decay rates that are slow enough to yield sufficient relic DM densities. The SHDM models are of special interest because they make predictions for possible outcomes of observations, e.g. those at the Pierre Auger Observatory. Such experiments might be able to verify whether the UHECR flux increases towards the Galactic Center which would indicate a link between the UHECRs and the galactic halo.

In case of the SHDM model the question arises which galactic sources can have a density high enough to provide an UHECR flux that is of the right order of mag-

nitude. After a wide range of ordinary and exotic sources failed to be the source of UHECRs Globular Cluster-like objects are proposed as potential sources. The number of Globular Clusters in our Galaxy agrees with the predicted amount of substructure in dark matter halos. In addition it is assumed that they contain enough dark matter to be considered as reasonable candidates.

The following subchapters will give a short introduction into UHECRs, dark matter density profiles, dark matter candidates, the GZK cutoff, and Globular Clusters. In Chapter 2 the different contributions to the UHECR flux will be introduced and explicit calculations for the most common dark matter profiles as well as for a new profile independent approach will be performed. Chapter 3 discusses the fit of the Globular Cluster data by Harris to the most common cuspy and cored dark matter profiles. Afterwards, in Chapter 4 a profile with a variable inner power law index is introduced and fitted to the data. Finally, Chapter 5 discusses the calculation of the core density of Globular Clusters.

1.1 Ultra High Energy Cosmic Ray

UHECRs can be defined as cosmic rays with energies exceeding $10^{19}\,\mathrm{eV}$ [1]. The pioneering measurements of UHECRs took place at the Volcano Ranch experiment that was performed between 1959 and 1976 by Lindesley. These results were recently reviewed by Dova *et al.* [2]. Other instruments that were built before 1966, when the GZK cutoff was first proposed, are Haverah Park, SUGAR, and Yakutsk. Recent experiments were performed by AGASA, HiRes and Fly's Eye. They showed that UHECRs up to the order of $10^{20}\,\mathrm{eV}$ exist. So far there are several hundred measured UHECR events with $E \geq 10^{19}\,\mathrm{eV}$ and 13 super GZK events with $E \geq 10^{20}\,\mathrm{eV}$, 11 detected by AGASA and 2 by HiRes. The highest energy ever detected was found by the Fly's Eye experiment at about $3 \cdot 10^{20}\,\mathrm{eV}$ [1].

Although today the existence of UHECRs is widely accepted it has been so far impossible to determine a detailed shape of the energy spectrum. This is mainly caused by two reasons. The first reason is the rarity of the measured events that hampers all current efforts because of low statistical significance. In addition there exists an energy discrepancy of 30% between the curves for the UHECR fluxes as determined by the two major experiments, AGASA and HiRes [1] which indicates a systematic error in at least one if not both experiments. Both inaccuracies could be significantly reduced with the publication of the first results from the Pierre Auger Observatory which should be able to increase the number of measured UHECR events

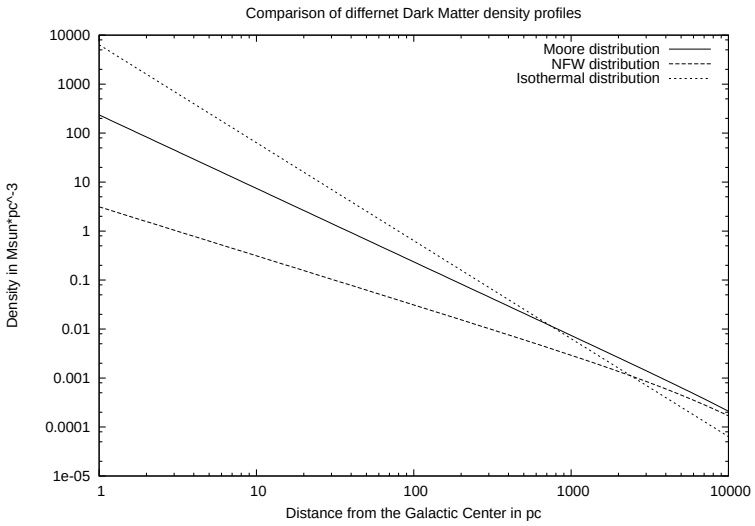

Figure 1.1: Comparison of dark matter densities. The graph shows the common logarithm of the dark matter density for different commonly used dark matter profiles over the distance from the center of the distribution.

and solve the energy discrepancy problem. Its detection rate for UHECR events per year is predicted to be 60 events above 10^{20} eV and about 6000 events above 10^{19} eV [3].

The composition of the primaries that initiate the detected air showers is difficult to establish. Dova *et al.* [2] and Watson [1] as well as the AGASA group propose a superposition of iron and protons as shower primaries but the reconstruction of the primary mass composition is subject to large theoretical uncertainties.

1.2 Density Profiles

Currently the real shape of dark matter distributions is unknown. In the most general case this could be any three dimensional density distribution without restricting spatial symmetries. Usually spherical symmetry of the dark matter halo is assumed and all commonly used dark matter profiles are solely radial dependent.

One of these profiles is the isothermal profile which has a wide application in physics

$$\rho_{\mathrm{iso}}(r) = \frac{\rho_0 r_s^2}{r^2}, \tag{1.1}$$

where r_s is the scale radius of the profile. A serious disadvantage of this profile is

that it does not agree with the widely accepted r^3 behaviour of dark matter halos for large radii, see e.g. [4, 5].

Another established profile that was initially proposed to describe the structure of star clusters but was also used for dark matter structures is the King-profile which was introduced in [6]

$$\rho_{\mathrm{King}}(r) = \frac{\rho_0 r_c^3}{(r^2 + r_c^2)^{\frac{3}{2}}}. \tag{1.2}$$

It agrees with the assumed large scale behaviour of dark matter halos and in addition has a flat core with core radius r_c. The existence of the core in the center is not a requirement but automatically avoids any unphysical divergences although it seems to contradict results from recent simulations of dark matter halos that favour cuspy dark matter profiles.

Based on numerical modelling of the gravitational collapse of dark matter halos it is now believed that, on large scales and beyond a certain threshold radius that is currently under discussion, the dark matter profile has the general form

$$\rho_H(r) = \frac{\rho_0}{\left(\frac{r}{r_s}\right)^{\alpha}\left(1+\frac{r}{r_s}\right)^{\gamma-\alpha}}, \tag{1.3}$$

where r_s is the scale radius, α is the inner power law index, and $\gamma = 3$ is the outer power law index that is assumed to be constant. The connection between the number density $n_H(r)$ and the density $\rho_H(r)$ is given by

$$\rho_H(r) = n_H(r) M_X, \tag{1.4}$$

where M_X is the mass of the SHDM particle. Similarly the normalisation constants ρ_0 and N_0 are related by $\rho_0 = N_0 M_X$.

Numerical simulations performed by Navarro, Frenk, and White (NFW) as well as those by Moore *et al.* have indicated an inner power law index of $1.0 \leq \alpha \leq 1.5$. These results lead to the following special case that is commonly used in present day articles and is usually referred to as the NFW-profile [4]

$$\rho_{\mathrm{NFW}}(r) = \frac{\rho_0}{\left(\frac{r}{r_s}\right)\left(1+\frac{r}{rs}\right)^2}. \tag{1.5}$$

Moore *et al.* developed a profile shape that differs slightly from the general form and

is referred to as the Moore-profile [5, 7]

$$\rho_{\mathrm{Moore}}(r) = \frac{\rho_0}{\left(\frac{r}{r_s}\right)^{1.5}\left(1+\left(\frac{r}{rs}\right)^{1.5}\right)}. \tag{1.6}$$

To compare the shape of the three cuspy profiles they are displayed together in Figure 1.1. One of the basic problems that these density distributions face is that they diverge at the origin. This leads to the cuspy halo problem that contradicts rotation curve measurements of dwarf spheroidal galaxies and dwarf irregular galaxies as well as observations of Low Surface Brightness Galaxies. Restrictions extracted from the measurements suggest that these objects have constant density cores [8, 9].

Recently, several authors argued that the cuspy behaviour of the dark matter halos is an artifact of the mass resolution limit of the performed simulations, e.g. a particle mass of $m_{\mathrm{res}} = 2.14 \cdot 10^7\, M_\odot$ in [10], and that it is only possible to resolve the density profile to a scale of about $0.1 r_s$. Based on these arguments it is possible that the NFW-profile as well as the Moore-profile have to be modified to account for a constant density core that is not yet resolvable with the resolution of present day simulations. The size r_c and density ρ_0 of the core only depend on the total mass of the dark matter halo. It has to be pointed out that ρ_0 now represents the density of a real core contrary to core densities that arise solely from the normalisation of the cuspy profiles in equation (1.3), (1.5), and (1.6). Provided that a core exists it is assumed to be smaller than 0.03 pc given by [11] while more conservative restrictions based on the resolution of the numerical simulations lead to a core size smaller than approximately $0.1 r_s$, that is of the order of a few kpc for a galaxy the size of our own.

Another very important feature of the mass distribution is the amount of substructure present. Even if only a small amount of the halo mass is bound in subclumps the contribution of these subclumps is not negligible. Most of the recent N-body simulations have found a large amount of substructure in the simulated galaxies, see e.g. [7]. However, if it is assumed that visible matter tracks dark matter on substructure scales there is a lack of observational proof in our own neighbourhood. These studies also predict that satellite galaxies have dark matter halos on their own [8, 10, 12]. The results of Colin *et al.* [8] show that dwarf halos are downscaled copies of massive halos and that the amount of substructure in a galaxy is mass independent. Unlike their more massive parent galaxies satellite galaxies are affected by external forces and their profile should be modified. Hayashi *et al.* [13] suggested that the resulting profile is simply a modified NFW-profile to account for

the tidal stripping effect. Tidal stripping is not able to redistribute the mass in the center significantly [10].

1.3 Dark Matter Candidates

Most recent results from the WMAP project predict a mass distribution in the presumably flat universe with cosmological density parameters of

$$\Omega_t = 1.0,\ \Omega_b = 0.044,\ \Omega_m = 0.27, \text{ and } \Omega_\Lambda = 0.73. \tag{1.7}$$

This shows that non-baryonic cold dark matter (CDM), $\Omega_{\text{CDM}} = \Omega_m - \Omega_b$, accounts for about 23 percent of the energy density in the universe. The rest of this section introduces some of the most likely CDM candidates and their association with UHECRs is discussed.

It has recently been shown that neutrinos are massive and therefore could qualify as non-baryonic dark matter [14]. Their mass, which only slightly differs from zero, excludes them from the beginning as UHECR sources but if their number density is taken into consideration they have the potential to make up a significant fraction of the non-baryonic dark matter. Unfortunately, neutrinos can only be hot dark matter and therefore do not qualify as cold dark matter.

Another candidate is Weakly Interacting Massive Particles (WIMPs) which arise from supersymmetric models [11] or are motivated from other extensions of the standard model of particle physics. Their generic coupling and mass ranges give a relic density in the required range to explain halo dark matter [14]. In most models, like the Minimal Supersymmetric extension of the Standard Model (MSSM), the Lightest Supersymmetric Particle (LSP) is the lightest neutralino. Its mass is assumed to be of the order of $50\,\text{GeV} < m_\chi < 500\,\text{GeV}$ [12]. The restriction given by Oguri *et al.* [15] is less stringent and an upper bound of 5 TeV is assumed, while Bergström [14] even assumes an upper bound of 10 TeV. Nevertheless, the mass of the WIMPs is still too small by about a factor of 10^9 to make WIMP decay or annihilation a possible source of UHECRs.

Dark matter candidates whose decay or annihilation radiation may be the origin of UHECRs have to fulfil several requirements. Their mass has to be at least of the order of $M_X \geq 10^{12}\,\text{GeV}$, SHDM, and their lifetime has to be sufficiently large. Therefore they might have a decay rate Γ [15, 16] that is slow enough to explain their presence in our universe. Together with the decaying DM scenario a DM

lifetime about the age of the universe is able to explain several phenomena such as the abundance of clusters of galaxies, the origin of UHECRs, and improve the fit of Type Ia supernovae observations and the evolution of mass to light ratios in clusters [15].

It is obvious that regions with high dark matter densities should dominate the anisotropy signal in top-down models. Therefore stellar structures with the highest densities in our neighbourhood are the most promising candidates, although, dark matter substructures do not necessarily have to coincide with stellar substructures because baryonic matter does not need to trace dark matter on subhalo scales. Among the structures of interest is the Galactic Center [17, 18], especially the innermost $1 - 100\,\mathrm{pc}$. Another potential source for the detection of SHDM annihilation radiation in our neighbourhood is the center of M32 that has the highest known density in nearby systems. The density there likely exceeds $10^7 M_\odot\,\mathrm{pc}^{-3}$ [17].

At this point it is worth mentioning that while WIMPs do not play a role in the explanation of UHECRs the model calculations in Chapter 2 are valid for them as well. The only difference is that the energy spectrum of the WIMP decay or annihilation radiation is many orders of magnitude smaller than for the SHDM case.

1.4 The Greisen-Zatsepin-Kuzmin Cutoff

The Cosmic Microwave Background (CMB) is nearly isotropic, except for temperature variations of the order of μK, and originates in the Big Bang. The CMB-photons have an energy of about $2 \cdot 10^{-4}\,\mathrm{eV}$ that corresponds to a temperature of $2.73\,\mathrm{K}$ and their density can be approximated with about 400 CMB-photons per cm^3. If the energy of an initial proton is sufficiently high, a collision between the proton and the CMB-photons can cause photoproduction of pions

$$\gamma + p \to n + \pi^+ \quad \text{or} \quad \gamma + p \to p + \pi^0. \tag{1.8}$$

This reaction reduces the initial energy of the proton. Thus we do not expect to detect protons above this energy if their source is distant enough to have almost surely collided with a CMB-photon on their way to us. This limit was first proposed by Greisen, Zatsepin, and Kuzmin in 1966 [19] and for this reason it is called the GZK cutoff. Its derivation follows mostly the calculations outlined in [20].

To simplify the derivation only the first interaction will be discussed in detail because the calculations for the second interaction are identical and the differences

in the final results are negligible. Furthermore it is useful to perform the calculations in the center of mass frame of the proton and the CMB-photon. In this frame the total momentum at any given time is zero and the equations for the conservation of momentum before and after the interaction can be written down separately

$$\vec{\mathbf{p}}_\gamma + \vec{\mathbf{p}}_p = 0 \quad \text{and} \quad \vec{\mathbf{p}}_n + \vec{\mathbf{p}}_{\pi^+} = 0. \tag{1.9}$$

At the threshold energy the initial energy of the proton and the CMB-photon is just enough to create a neutron and a pion at rest. Therefore the second equation is trivial and the momentum of the incoming proton and photon are equal and opposite as defined by the center of mass frame

$$\vec{\mathbf{p}}_\gamma = -\vec{\mathbf{p}}_p. \tag{1.10}$$

An equation for the cutoff energy can be derived by using the conservation of the four momentum $p = (E, \vec{\mathbf{p}})$ in a particle interaction, where the speed of light is set to unity, $c = 1$, for the rest of this section. For an interaction as described in equation (1.8) the conservation of 4-momentum implies

$$(p_\gamma + p_p)^\alpha (p_\gamma + p_p)_\alpha = (p_n + p_{\pi^+})^\alpha (p_n + p_{\pi^+})_\alpha . \tag{1.11}$$

At this stage it is useful to evaluate both sides of the equation independently.

$$\begin{aligned} &\text{(lhs):} \quad (p_\gamma + p_p)^\alpha (p_\gamma + p_p)_\alpha &&= -4E_\gamma E_p - m_p^2 \\ &\text{(rhs):} \quad (p_n + p_{\pi^+})^\alpha (p_n + p_{\pi^+})_\alpha &&= -(m_p + m_{\pi^+})^2 \end{aligned} \tag{1.12}$$

To evaluate the four momenta equation and simplify the results as much as possible the relations $E_\gamma = \left|\vec{\mathbf{p}}_\gamma\right|$, $m_p \approx m_n$, and $E_p \approx \left|\vec{\mathbf{p}}_p\right|$ for $E_p \gg m_p$ were used. A more detailed derivation that outlines all steps of the calculation can be found in Appendix A. The equation for the cutoff energy can now easily be found by substituting the intermediate results into equation (1.11) for the conservation of the four momentum and solving for the proton energy

$$E_p = \frac{m_p m_{\pi^+}}{2E_\gamma} \left(1 + \frac{m_{\pi^+}}{2m_p}\right). \tag{1.13}$$

This equation for the cutoff energy depends solely on well known parameters. A numerical value for the cutoff energy can be computed by inserting the appropriate numbers for the proton mass $m_p = 938.3\,\text{MeV}$, the pion masses $m_{\pi^0} = 135\,\text{MeV}$ and

$m_{\pi^+} = 139\,\mathrm{MeV}$, and the energy of the CMB-photons $E_\gamma = 2 \cdot 10^{-4}\,\mathrm{eV}$. It results in a GZK-cutoff energy of

$$E_{\mathrm{GZK}} \approx 3.5 \cdot 10^{20}\,\mathrm{eV}. \tag{1.14}$$

It has to be pointed out that this calculation of the GZK-cutoff energy is only a crude approximation and a more elaborate analysis yields a result that is about one order of magnitude lower. Nevertheless it represents a good assumption on the upper limit of the GZK-cutoff energy.

Another tremendously important parameter is the mean free path of the proton. It can be calculated from

$$\lambda_{\mathrm{CMB}} = \frac{1}{\sigma N_\gamma}. \tag{1.15}$$

With the substitution of the corresponding numbers for the cross section of the reaction of about $2 \cdot 10^{-28}\,\mathrm{cm}^2$ and the number density of the CMB-photons of $400\,\mathrm{cm}^{-3}$, a mean free path of $\lambda_{\mathrm{CMB}} \approx 10^7\,\mathrm{ly} \approx 3\,\mathrm{Mpc}$ is found. It only takes a small number of mean free paths for the proton energy to degrade. Thus, protons with energies of about or in excess of the GZK-cutoff energy cannot have an origin that is too far away. The assumption that has been made in most present day papers is that the distance for the GZK cutoff is about 50 Mpc to 100 Mpc.

1.5 Globular Cluster

Globular Clusters (GCs) provide critical observational boundary conditions on cosmology and galaxy formation, the evolution of low-mass stars, stellar dynamics, the properties of variable and binary stars, and galactic structure dynamics [21]. They are groups of stars that contain between 3000 and 27000 individual stars which have been formed at the same time [22, 23]. For this reason the chemical composition of the stars in a GC is the same and they only differ in mass [24]. To characterise the density distribution of a GC it is sufficient to measure three parameters. These parameters vary in the discussion by different authors and are chosen to be the core radius, the tidal radius and a richness factor by King [6] while Walcher *et al.* chose the velocity dispersion, the effective radius and the surface brightness [25].

Currently 150 GCs are known in our own Galaxy, although, the discovery of an anomalously faint GC indicates that this list might not be complete and that there are other faint undetected GCs in our galactic halo [26]. The measured parameters

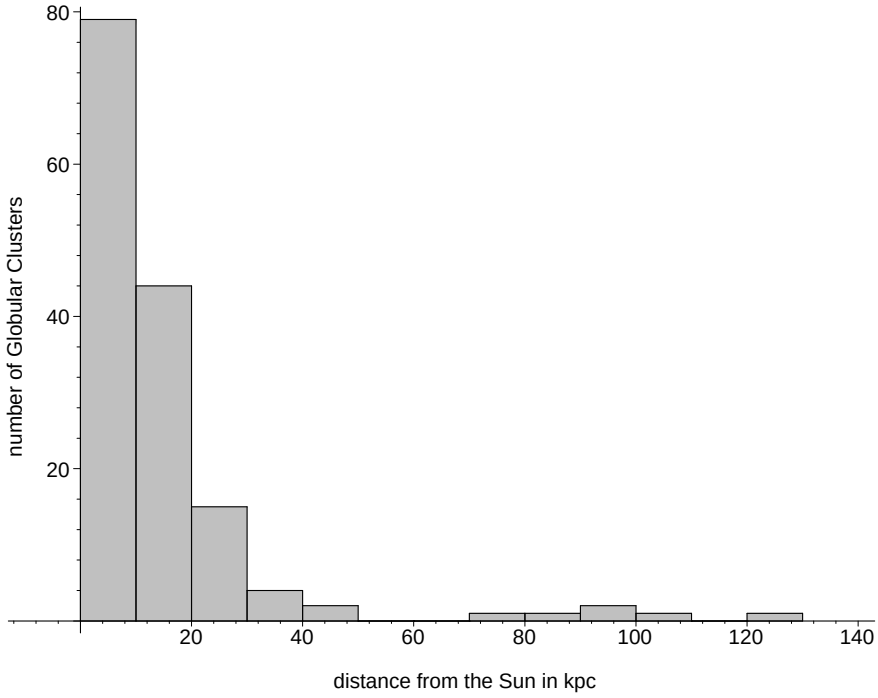

Figure 1.2: Distances of the Globular Clusters from the Sun. The histogram plot displays the number of Globular Clusters over the distance from the Sun in kpc. A bin contains all Globular Clusters with a distance from the Sun of $r_{\min} \leq r < r_{\max}$.

of these GCs were summarised by Harris [21] whose catalogue represents the most complete and up to date dataset for GCs. Some of the most important Globular Cluster parameters listed are the distance from the Sun, the core radius, the half mass radius, the tidal radius and the visual magnitude. To show the general properties of some of these parameters the distance from the Sun, the core radius and the tidal radius are displayed in Figures 1.2 to 1.4.

In Figure 1.2 the number of Globular Clusters is shown over the distance from our Sun in kpc. From the histogram plot it can be concluded that most Globular Clusters are less than 30 kpc away from our solar system which itself is approximately located at a distance of 8 kpc from the center of our Galaxy. This indicates a clustering of Globular Clusters around the Galactic Center. An additional analysis of the distance from the Galactic Center which is not of further relevance for the calculations confirms that most of the Globular Clusters are indeed located close to the center of the Galaxy while there are only a few Globular Clusters in the outer regions.

Figure 1.3 depicts the number of Globular Clusters over the core radius d_c in pc. It is obvious that most Globular Clusters have a small core with a radius of less than

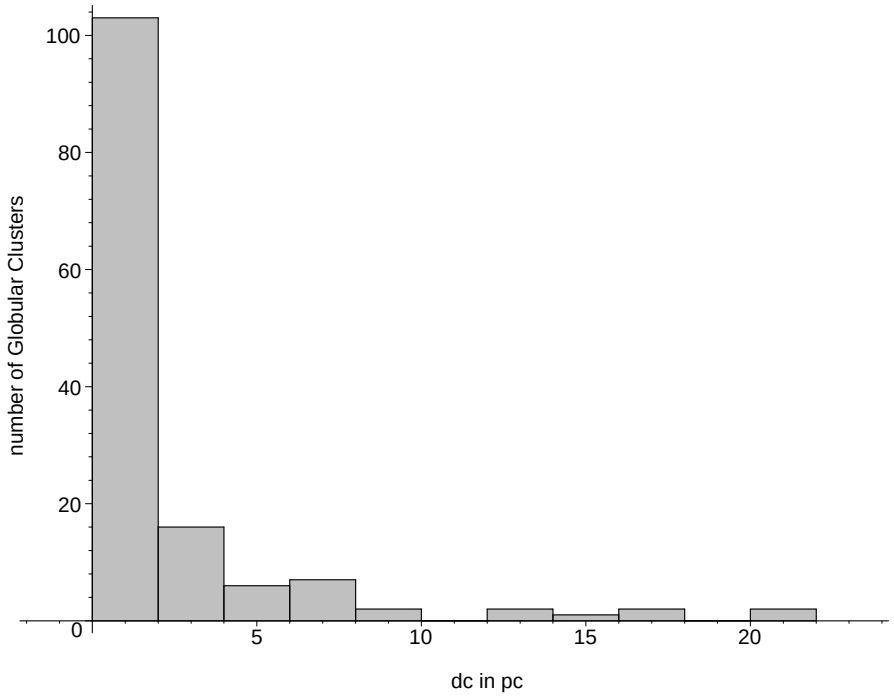

Figure 1.3: Core radii of the Globular Clusters. The histogram plot displays the number of Globular Clusters over the core radius d_c of the Globular Cluster in pc. A bin contains all Globular Clusters with a core radius of $d_{\min} \leq d_c < d_{\max}$.

2 pc, although, some of the Globular Clusters have significantly larger cores.

In the last histogram plot, Figure 1.4, the number of Globular Clusters is displayed over the tidal radius d_t in units of the core radius. The maximum of the distribution is located at approximately 30 core radii while the upper common range for the tidal radius reaches up to 120 core radii.

The distinction between GCs, Nuclear Clusters (NCs), Dwarf Spheroidal Galaxies, and Super Star Clusters is sometimes ambiguous because of the overlapping mass ranges [25, 26]. The dynamical mass of a GC is approximately $10^4\,M_\odot$ to $10^6\,M_\odot$ [27] which is about one order of magnitude smaller than the masses of Nuclear Clusters [25]. Other authors extend the mass range of GCs up to $10^8\,M_\odot$ [28, 29] which easily overlaps the mass range of Nuclear Clusters. The higher range is due to an assumed ratio between the stellar mass $M_\star$ and DM $M_{\rm DM}$ of $\chi \equiv M_\star/M_{\rm DM} = 0.008$ that lies between the universal baryonic to DM density ratio $\Omega_{\rm b}/\Omega_{\rm DM} = 0.2$ and the fraction of baryons in GCs in the modern universe of approximately 0.0025 [28]. Based on these values for the GC masses the central density of a GC falls in the range between $10^4\,M_\odot{\rm pc}^{-3}$ and $10^6\,M_\odot{\rm pc}^{-3}$ which is comparable to the densest star forming regions in the Milky Way (MW) [30, 31].

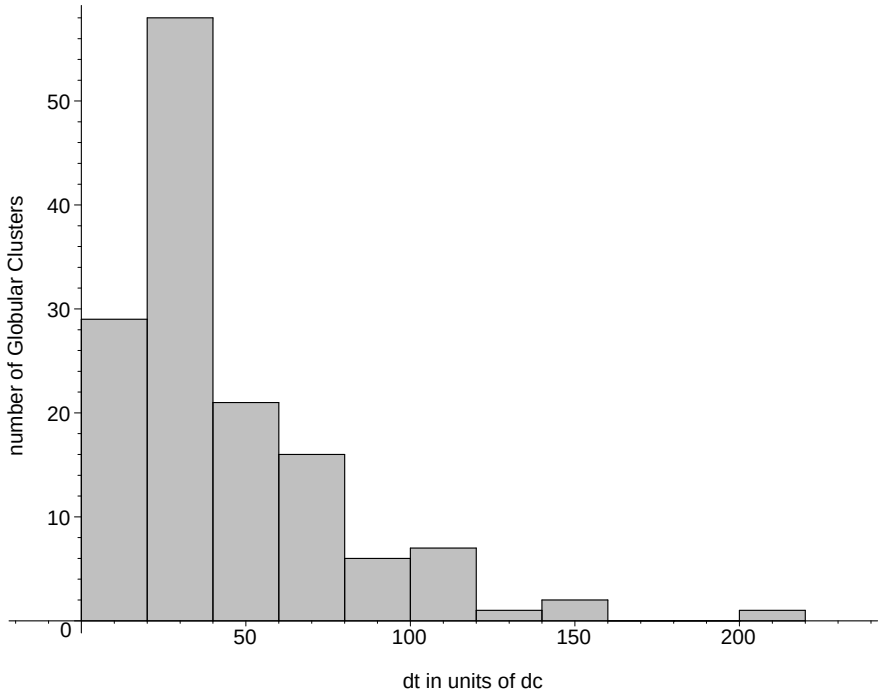

Figure 1.4: Tidal Radii of the Globular Clusters. The histogram plot displays the number of Globular Clusters over the tidal radius d_t of the Globular Cluster in pc. A bin contains all Globular Clusters with a tidal radius of $d_{\min} \leq d_t < d_{\max}$.

Over the last years there is increasing evidence for the possibility of Intermediate Mass Black Holes (IMBHs) with masses $125\,M_\odot \leq M_{\mathrm{BH}} \leq 1000\,M_\odot$ in the centres of some GCs [35]. The investigation of the initial sample that contained data for 37 Globular Clusters revealed that 5 of them are in good agreement with predictions for Globular Cluster with a central IMBH. The density cusp in these GCs may not be apparent because a cuspy density profile does not imply a cusp in luminosity. Furthermore potential central cusps are smeared because of optical resolution limits.

To explain why Nuclear Clusters are not considered in our model it is necessary to have a more detailed look at them. Nuclear Clusters have general cluster properties much like Globular Clusters but they are located in the direct proximity of the Center of the Galaxy in which they reside. According to Böker *et al.* [32, 33] Nuclear Clusters are a common feature for Late-Type Spiral Galaxies. Our own Galaxy has exactly one of these Nuclear Clusters located around Sagittarius A^* which is thought to be a supermassive black hole in the centre of our Galaxy [34]. In addition it seems that the most luminous stars in this Cluster originate in a star formation burst within the last 10 Myrs which is in contrast to the populations in Globular Clusters which usually have ages of the order of Gyrs.

Chapter 2

Ultra High Energy Cosmic Ray Flux From Superheavy Dark Matter

The first part of this chapter outlines the calculations necessary to derive the UHECR flux from the annihilation and decay of SHDM. Within this outline no specific dark matter profile is chosen and none of the profile dependent calculations are evaluated. Thus the equations are kept as general as possible. Explicit calculations are deferred to the subchapters where the UHECR flux is discussed for three different dark matter profiles: the NFW-profile, the Moore-profile, and a constant density approach.

The shape of the dark matter density profile has a more or less significant influence on the detectable flux of UHECRs. This is dependent on whether the UHECRs originate in the decay or the annihilation of SHDM. In the scenario of decaying SHDM the UHECR flux is linearly dependent on the profile of the dark matter number distribution $n_H(r)$

$$\mathcal{F} = 2\frac{\mathrm{d}N(E, E_{\mathrm{jet}})}{\mathrm{d}E}\Gamma_X \int \mathrm{d}^3\vec{r}\,\frac{n_H(r)}{4\pi\left|\vec{r}-\vec{r}_{\odot}\right|^2}, \tag{2.1}$$

while the dependence is quadratic in the case of SHDM annihilation as a generation process for UHECRs [36, 37]

$$\mathcal{F} = 2\frac{\mathrm{d}N(E, E_{\mathrm{jet}})}{\mathrm{d}E}\langle\sigma v\rangle \int d^3\vec{r}\,\frac{n_H^2(r)}{4\pi\left|\vec{r}-\vec{r}_{\odot}\right|^2}. \tag{2.2}$$

In these equations $\mathrm{d}N(E, E_{\mathrm{jet}})/\mathrm{d}E$ specifies the fragmentation spectrum resulting from a primary particle with energy E_{jet}. Furthermore, Γ_X is the decay rate of SHDM particles, $\langle\sigma v\rangle$ is the product of the annihilation cross section of SHDM particles with

their relative speed, and $r_\odot$ is the distance of the Sun from the Galactic Center. All models that assume the decay or the annihilation of SHDM as the origin of UHECRs are based on these two general equations. Therefore the evaluation of the UHECR flux is primarily dependent on the density distribution of the SHDM particles.

To perform any explicit calculations it is necessary to initially specify the dark matter distribution. The most common profiles were introduced in Section 1.2 as well as the usually assumed symmetries. To maintain generality an arbitrary spherically symmetric profile will be used for the rest of the introduction for this chapter

$$n_H(r) = \frac{\rho_H(r)}{M_X} \quad \text{for } r \geq 0, \tag{2.3}$$

where the density $\rho_H(r)$ and the number density $n_H(r)$ are proportional to each other and M_X is the mass of the SHDM particle.

Before the dark matter profile can be used in calculations it has to be normalised. This can be done by integrating the dark matter density, as specified in equation (2.3), over the volume of the dark matter halo. The integration over the solid angle yields a 4π prefactor because the density distribution is only radially dependent

$$M_H = 4\pi \int_0^{r_t} \mathrm{d}r\, \rho_H(r) r^2. \tag{2.4}$$

For the radial integration it is necessary to introduce a cutoff radius to avoid a non-physical divergence of the halo mass. This cutoff radius is chosen to be the tidal radius r_t of the galaxy beyond which particles are no longer gravitationally bound to the dark matter halo.

After the normalisation of the profile the decay flux from the smoothly distributed SHDM fraction in the DM halo can be calculated by inserting the normalised DM number density, as defined in equation (2.3), into equation (2.1) for the decay flux. As for the normalisation of the dark matter profile the equation for the decay flux can be simplified to a radial integral

$$\mathcal{F} = \frac{\mathrm{d}N(E, E_{\mathrm{jet}})}{\mathrm{d}E} \Gamma_X \frac{1}{r_\odot} \int_0^{r_t} \mathrm{d}r\, r n_H(r) \ln \frac{r + r_\odot}{|r - r_\odot|}. \tag{2.5}$$

Similarly the annihilation flux can be derived by plugging the DM number density from equation (2.3) into equation (2.2) for the annihilation flux

$$\mathcal{F} = \frac{\mathrm{d}N(E, E_{\mathrm{jet}})}{\mathrm{d}E} \langle \sigma v \rangle \frac{1}{r_\odot} \int_0^{r_t} \mathrm{d}r\, r n_H^2(r) \ln \frac{r + r_\odot}{|r - r_\odot|}. \tag{2.6}$$

Up to this point the model does not account for any kind of substructure that was found in all recent DM simulations. This can be achieved by assuming that a certain fraction ξ of the DM in the halo is clumped. It is estimated that this fraction is of the order of $\xi \approx 0.1$.

Like for the DM halo of a galaxy it is necessary to make an assumption on the distribution of the DM within a subclump. Recent simulations showed that dwarf halos are downscaled versions of massive halos. Therefore the most straightforward assumption is that the density distribution within a subclump is the same as within the host galaxy. It is defined in analogy to the number density of the halo profile and only the radii have to be replaced with the corresponding equivalents for the subclump

$$n_X(d, r) = \frac{\rho_X\,(d, r)}{M_X}, \tag{2.7}$$

where the number density of the subclump $n_X(d, r)$ is now dependent on the distance d from the center of the subclump as well as on the distance r of the subclump from the Galactic Center. To better distinguish between the radii for the halo and those for the subclumps this notation will be used for the rest of the thesis unless otherwise stated.

The only major difference between the halo density and the subclump density is the normalisation. The subclump density is normalised such that the subclump density at the tidal radius d_t of the subclump is equal to the density of the parent halo at distance r of the subclump from the Galactic Center. This is reasonable because the distance of a subclump from the Galactic Center is much bigger than its tidal radius, $r \gg d_t$, and therefore the density of the parent halo is approximately constant throughout the whole volume of the subclump. The subclump profile is normalised by integrating the subclump density over the volume of the subclump

$$M_{\mathrm{cl}} = 4\pi \int_0^{d_t} \mathrm{d}d\, \rho_X(d, r) d^2. \tag{2.8}$$

The result of the integration can either be solved exactly for the tidal radius d_t of the subclump or it can be approximated by assuming that the scale radius d_s of the subclump is much smaller than its tidal radius, $d_s \ll d_t$. In both cases the tidal radius of the subclump is dependent on the distance of the subclump from the Galactic Center and the mass of the Globular Cluster.

The next step in the derivation of the annihilation flux from the clumped com-

ponent is to calculate the annihilation rate within an individual subclump

$$\mathcal{R}(r, M_{\rm cl}) = 4\pi\langle\sigma v\rangle \int_0^{d_t} \mathrm{d}d\, n_X^2(d, r) d^2, \tag{2.9}$$

where the tidal radius of the subclump was derived from equation (2.8).

During the calculations for the tidal radius and the annihilation rate only the contribution of a single subclump was considered. For the total annihilation flux it is important how the independent subclumps are distributed within the galaxy. This distribution can be found by simulations but can also be approximated by direct measurements of the substructure, e.g. Globular Cluster distribution, in our own galaxy. It has to be pointed out that for the direct measurement method it is assumed that the dark matter substructure has the same characteristics as the substructure of the observed stellar matter.

The distribution of subclumps in the galaxy is independent of the actual shape of the dark matter profile. For the rest of the thesis this subclump distribution function is assumed to be

$$n_{\rm cl}(r, M_{\rm cl}) = n_{\rm cl}^0 \left(\frac{M_H}{M_{\rm cl}}\right)^{\alpha} \frac{{R_c^{\rm cl}}^3}{\left({R_c^{\rm cl}}^2 + r^2\right)^{\frac{3}{2}}}, \tag{2.10}$$

where $n_{\rm cl}^0$ is the normalisation constant of the subclump distribution, the parameter $\alpha = 1.9$ is determined experimentally, and the scale radius $R_{\rm c}^{\rm cl}$ of the subclump distribution is of the order of $10\,\mathrm{kpc} \leq R_c^{\rm cl} \leq 20\,\mathrm{kpc}$ [36]. It has to be emphasised that the parameter α in the subclump distribution has no connection with the inner power law index α from equation (1.3) that will play an important role in Chapter 4.

The normalisation constant of the subclump distribution can be found by integrating the product of the subclump distribution with the subclump mass over the volume of the parent halo and the possible range of subclump masses

$$\xi M_H = 4\pi \frac{n_{\rm cl}^0 M_H^2 \eta^{2-\alpha} {R_c^{\rm cl}}^3}{2-\alpha} \left\{ \ln\left(\frac{r_t + \sqrt{{R_c^{\rm cl}}^2 + r_t^2}}{R_c^{\rm cl}}\right) - \frac{r_t}{\sqrt{{R_c^{\rm cl}}^2 + r_t^2}} \right\}. \tag{2.11}$$

The parameter η in this equation arises from the integration over the mass and specifies the maximum possible fraction of the halo mass that a substructure can have. It is evident that this fraction has to be smaller than the fraction of clumped

dark matter in the halo, $\eta \leq \xi$, and is assumed to be in the range $0.01\xi \leq \eta \leq \xi$. For $\eta = \xi$ this can be interpreted as a single massive subclump orbiting in the DM halo of the parent galaxy. The equation for the clumped mass fraction of the dark matter halo can easily be solved for the normalisation constant of the subclump distribution

$$n_{\mathrm{cl}}^{0} = \frac{\xi\,(2-\alpha)}{4\pi M_H \eta^{2-\alpha} {R_c^{\mathrm{cl}}}^3 \left\{ \ln\left(\frac{r_t + \sqrt{{R_c^{\mathrm{cl}}}^2 + r_t^2}}{R_c^{\mathrm{cl}}} \right) - \frac{r_t}{\sqrt{{R_c^{\mathrm{cl}}}^2 + r_t^2}} \right\}}. \tag{2.12}$$

The expression for the normalisation constant can be approximated because the scale radius of the subclump distribution is of the order of $10\,\mathrm{kpc} \leq R_c^{\mathrm{cl}} \leq 20\,\mathrm{kpc}$ while the tidal radius of the galaxy is much larger $r_t \approx 250\,\mathrm{kpc}$. This approximation does not eliminate any of the parameters from the exact result for the normalisation constant and is therefore irrelevant at this point. Nevertheless it is useful to keep this approximation possibility in mind for the explicit calculations in the following subchapters.

Finally it is possible to calculate the annihilation flux from the clumped component by integrating the convolution of the annihilation rate of a subclump at radius r from the center of the halo with the subclump distribution over the volume of the halo and over the possible range of subclump masses

$$\mathcal{F} = \frac{\mathrm{d}N}{\mathrm{d}E} \frac{1}{r_\odot} \int_0^{r_t} \mathrm{d}r\, r \ln \frac{r + r_\odot}{|r - r_\odot|} \int_0^{\eta M_H} \mathrm{d}M_{\mathrm{cl}}\, n_{\mathrm{cl}}(r, M_{\mathrm{cl}}) \mathcal{R}(r, M_{\mathrm{cl}}). \tag{2.13}$$

The factors involved in this equation for the annihilation flux from the clumped dark matter fraction have to be replaced with the previous results for the subclump distribution from equations (2.10) and (2.12) and the expression for the annihilation rate from equation (2.9).

After this detailed derivation of the expected flux from the smooth and clumped DM component these calculations are explicitly performed for different DM profiles. First the NFW-profile will be discussed. Then the same calculations will be repeated for the Moore profile. At last a new approach will be introduced to achieve a rough approximation. This approach assumes that the clumped component is given by a discrete subclump distribution where every subclump has a constant density.

2.1 Navarro, Frenk, and White-Profile

In this section the previously outlined calculations are performed by assuming that the DM halo has the form of a NFW-profile. To improve the legibility of this section and especially shorten it only the results of the calculations are shown. A detailed summary of the calculations and approximations is deferred to Appendix B.

The NFW-profile is given by equation (1.5) and the number density is defined by relation (2.3)

$$n_H(r) = \frac{\rho_H(r)}{M_X} = \frac{N_0 r_s^3}{r\left(r + r_s\right)^2}, \tag{2.14}$$

where M_X is the mass of the SHDM particle, N_0 is the normalisation constant of the number density, and r_s is the scale radius of the NFW-profile. The normalisation constant N_0 can then be calculated by inserting the NFW density distribution from equation (2.14) into equation (2.4) for the halo mass. For the NFW-profile the radial integral can be solved analytically and the halo mass can be written as

$$M_H = 4\pi N_0 M_X r_s^3 \left(\ln\frac{r_t + r_s}{r_s} - \frac{r_t}{r_t + r_s}\right). \tag{2.15}$$

This equation can easily be solved for the normalisation constant

$$N_0 = \frac{M_H}{4\pi M_X r_s^3 \left(\ln\frac{r_t+r_s}{r_s} - \frac{r_t}{r_t+r_s}\right)}. \tag{2.16}$$

The decay flux from the smoothly distributed SHDM fraction can now be calculated by replacing the general dark matter number density in equation (2.5) with the NFW number density as defined in equation (2.14). After solving the radial integral the decay flux is given by

$$\begin{aligned}\mathcal{F} = \frac{\mathrm{d}N}{\mathrm{d}E}\Gamma_X N_0 \frac{r_s^3}{r_\odot}\Bigg\{&\frac{1}{r_t + r_s}\ln\frac{r_t - r_\odot}{r_t + r_\odot} + \frac{1}{r_s - r_\odot}\ln\frac{r_s\left(r_t + r_\odot\right)}{r_\odot\left(r_t + r_s\right)} \\ &+\frac{1}{r_s + r_\odot}\ln\frac{r_\odot\left(r_t + r_s\right)}{r_s\left(r_t - r_\odot\right)}\Bigg\}.\end{aligned} \tag{2.17}$$

Similarly it is possible to calculate the flux from the annihilation of SHDM particles in the galactic halo by inserting the NFW number density from equation (2.14) into

equation (2.6)

$$\begin{aligned}\mathcal{F} = \frac{\mathrm{d}N}{\mathrm{d}E}\langle\sigma v\rangle N_0^2 \frac{r_s^2}{r_\odot}\Bigg\{ & \frac{\pi^2}{3} - \ln\frac{r_s}{r_s - r_\odot}\ln\frac{r_s + r_\odot}{r_\odot} + \frac{1}{2}\ln^2\frac{r_s + r_\odot}{r_s - r_\odot} \\ & + L_2\left(\frac{r_s}{r_s - r_\odot}\right) + L_2\left(\frac{r_\odot}{r_s + r_\odot}\right) + \frac{4 r_\odot r_s \left(2r_s^2 - r_\odot^2\right)}{3\left(r_s^2 - r_\odot^2\right)^2} \\ & - \frac{2 r_\odot r_s \left(3r_\odot^4 - 8 r_\odot^2 r_s^2 + 9 r_s^4\right)}{3\left(r_s^2 - r_\odot^2\right)^3}\ln\frac{r_s}{r_\odot}\Bigg\},\end{aligned} \tag{2.18}$$

where $L_2(x)$ defines the dilogarithm of x.

So far the model only includes the smoothly distributed part of the dark matter. Any substructure that is predicted by recent simulations was neglected. This can be resolved by simply assuming that a certain fraction $\xi = 0.1$ of the dark matter in the halo is clumped. Furthermore it is assumed that the subclumps are downscaled versions of the parent halo and have a NFW-profile as well. The NFW-profile for a subclump can then be written as

$$n_X(d, r) = \frac{\rho_X(d, r)}{M_X} = n_H(r)\frac{d_t\left(d_t + d_s\right)^2}{d\left(d + d_s\right)^2}, \tag{2.19}$$

which is dependent on the distance d from the center of the subclump as well as on the distance r of the subclump from the Galactic Center. The density profile of the subclump was renormalised in a way that the density at the tidal radius of the subclump is equal to the density of the parent halo at distance r of the subclump from the Galactic Center. This is reasonable because the radius of a subclump is much smaller than its distance from the Galactic Center and therefore the halo density is approximately constant throughout the volume of the subclump.

The tidal radius of a subclump can be calculated in the same way as the normalisation constant of the dark matter density of the halo by integrating the subclump density, introduced in equation (2.19), over the volume of the subclump

$$M_{\mathrm{cl}} = 4\pi n_H(r) M_X d_t\left(d_t + d_s\right)^2\left(\ln\frac{d_t + d_s}{d_s} - \frac{d_t}{d_t + d_s}\right). \tag{2.20}$$

Unfortunately this equation cannot be solved analytically for the tidal radius and it is necessary to either find a numerical solution to the problem or make an acceptable approximation. Numerical results for the tidal radius can easily be found if the scale radius is known. If the scale radius is unknown it is more appropriate to find an approximation that represents a good fit for the whole expected range of the relation

between the scale radius and the tidal radius. An obvious choice for an approximation is given by calculations that determined the most common range of the tidal radius to be $5d_s \leq d_t \leq 50d_s$. This shows that the tidal radius is much larger than the scale radius, $d_t \gg d_s$, but finite. It turns out that within this range $d_t^2\,(d_t + d_s) \approx d_t^3$ and $\left(\ln \frac{d_t+d_s}{d_s} - \frac{d_t}{d_t+d_s}\right) \approx 2$ is nearly constant and therefore equation (2.20) can be approximated by

$$M_{\rm cl} \approx 8\pi n_H(r) M_X d_t^3 \tag{2.21}$$

for the whole range of interest. This simplified solution for the subclump mass can now easily be solved for the tidal radius of the subclump

$$d_t = d_t(r, M_{\rm cl}) \approx \sqrt[3]{\frac{M_{\rm cl}}{8\pi n_H(r) M_X}}. \tag{2.22}$$

However, the tidal radius of the subclump remains dependent on the distance of the subclump from the Galactic Center and the mass of the subclump.

The next step in the calculation of the expected annihilation flux from the clumped component is to derive the annihilation rate within an individual subclump. This is done by inserting the previously defined number density of the subclump, equation (2.19), into equation (2.9) for the annihilation rate within a subclump and solving the radial integral

$$\mathcal{R}\,(r, M_{\rm cl}) = \frac{4\pi}{3}\langle\sigma v\rangle n_H^2(r) d_t^2\,(d_t + d_s)\left\{\frac{(d_t + d_s)^3}{d_s^3} - 1\right\}, \tag{2.23}$$

where the tidal radius of the subclump has to be computed from equation (2.20). As for the tidal radius the approximation $d_t \gg d_s$ can be used to simplify the annihilation rate. By using $d_t^2\,(d_t + d_s)\left\{\frac{(d_t+d_s)^3}{d_s^3} - 1\right\} \approx \frac{d_t^6}{d_s^3}$ and the approximated result for the tidal radius from equation (2.22) the annihilation rate can be expressed in a very simple form

$$\mathcal{R} \approx \frac{1}{48\pi}\langle\sigma v\rangle \frac{M_{\rm cl}^2}{M_X^2 d_s^3} \tag{2.24}$$

that is only dependent on the annihilation cross section $\langle\sigma v\rangle$, the SHDM particle mass M_X, the mass of the subclump $M_{\rm cl}$, and the scale radius of the subclump d_s.

Finally it is possible to derive the annihilation flux from the clumped dark matter fraction by inserting the annihilation rate from equation (2.23) and the previously

derived subclump distribution from equation (2.10) into equation (2.13) for the annihilation flux from the clumped component

$$\mathcal{F} = \frac{4\pi}{3}\frac{\mathrm{d}N}{\mathrm{d}E}\langle\sigma v\rangle N_0^2 n_{\mathrm{cl}}^0 M_H^\alpha \frac{r_s^6 {R_c^{\mathrm{cl}}}^3}{r_\odot}\int_0^{r_t}\mathrm{d}r\,\frac{1}{r\left(r+r_s\right)^4\left({R_c^{\mathrm{cl}}}^2+r^2\right)^{\frac{3}{2}}}\ln\frac{r+r_\odot}{|r-r_\odot|} \\ \times\int_0^{\eta M_H}\mathrm{d}M_{\mathrm{cl}}\,M_{\mathrm{cl}}^{-\alpha}d_t^2\left(d_t+d_s\right)\left\{\frac{\left(d_t+d_s\right)^3}{d_s^3}-1\right\}, \tag{2.25}$$

where $d_t = d_t(r, M_{\mathrm{cl}})$ is the mass and radial dependent tidal radius of the subclump. Neither the radial integral nor the integration over the subclump mass can be solved exactly, but can instead be simplified by assuming that $d_t \gg d_s$ and $r_t \gg R_c^{\mathrm{cl}}$. The approximated annihilation flux from subclumps with NFW-profile is thus given by

$$\mathcal{F} = \frac{1}{48\pi}\frac{\mathrm{d}N}{\mathrm{d}E}\langle\sigma v\rangle n_{\mathrm{cl}}^0\frac{\eta^{3-\alpha}M_H^3}{(3-\alpha)\,M_X^2}\frac{{R_c^{\mathrm{cl}}}^3}{r_\odot d_s^3\sqrt{r_\odot^2+{R_c^{\mathrm{cl}}}^2}} \\ \times\ln\left(1+\frac{2r_\odot}{\sqrt{{R_c^{\mathrm{cl}}}^2+r_\odot^2}-r_\odot}\right). \tag{2.26}$$

2.2 Moore-Profile

As indicated at the beginning of this chapter it is crucial to specify the distribution of the dark matter first. For the rest of this section it is assumed that the dark matter is distributed according to a Moore profile which is defined in equation (1.6). The number density of dark matter particles is therefore given by

$$n_H(r) = \frac{\rho_H(r)}{M_X} = \frac{N_0 r_s^3}{r^{\frac{3}{2}}\left(r^{\frac{3}{2}}+r_s^{\frac{3}{2}}\right)}. \tag{2.27}$$

As for the NFW-profile the complete calculations for the Moore-profile are very lengthy and only the results are shown in this section. The calculations and approximations are summarised in detail in Appendix C.

The profile can be normalised by substituting the Moore-profile as defined in equation (2.27) into equation (2.4) for the halo mass and performing the radial integration

$$M_H = \frac{8\pi}{3}N_0 M_X r_s^3\ln\left(1+\left(\frac{r_t}{r_s}\right)^{\frac{3}{2}}\right), \tag{2.28}$$

where the tidal radius of the dark matter halo r_t is the cutoff radius for the simulated galaxy. This yields a normalisation constant of

$$N_0 = \frac{3M_H}{8\pi M_X r_s^3 \ln\left(1 + \left(\frac{r_t}{r_s}\right)^{\frac{3}{2}}\right)}. \tag{2.29}$$

Now it is possible to calculate the flux from SHDM decay by inserting the normalised number density from equation (2.27) into the general equation for the decay flux (2.1)

$$\mathcal{F} = \frac{\mathrm{d}N}{\mathrm{d}E}\frac{\Gamma_X N_0 r_s^3}{r_\odot}\int_0^{r_t} \mathrm{d}r\, \frac{1}{\sqrt{r}\left(r^{\frac{3}{2}} + r_s^{\frac{3}{2}}\right)} \ln\frac{r + r_\odot}{|r - r_\odot|}. \tag{2.30}$$

Respectively the annihilation flux from SHDM can be derived by substituting the number density form equation (2.27) into equation (2.2) for the annihilation flux

$$\mathcal{F} = \frac{\mathrm{d}N}{\mathrm{d}E}\frac{\langle\sigma v\rangle N_0^2 r_s^6}{r_\odot}\int_0^{r_t} \mathrm{d}r\, \frac{1}{r^2\left(r^{\frac{3}{2}} + r_s^{\frac{3}{2}}\right)^2} \ln\frac{r + r_\odot}{|r - r_\odot|}. \tag{2.31}$$

For the Moore profile neither equation can be solved analytically. To obtain explicit values for the radial integrals it is necessary to apply numerical methods.

So far only the smoothly distributed part of the dark matter is considered. The clumped fraction can be included by using the same arguments as in the introduction and the previous section for the NFW-profile. It is assumed that a fraction $\xi \approx 0.1$ of the dark matter is clumped and the subclumps show a Moore-profile like the parent halo does.

The substructure profile is defined similar to the halo profile and only has to be properly renormalised. It is normalised such that the subclump density at the tidal radius is equal to the background density $n_H(r)$ of the smoothly distributed dark matter halo at distance r of the subclump from the Galactic Center

$$n_X(d, r) = \frac{d_t^{\frac{3}{2}}\left(d_t^{\frac{3}{2}} + d_s^{\frac{3}{2}}\right)}{d^{\frac{3}{2}}\left(d^{\frac{3}{2}} + d_s^{\frac{3}{2}}\right)} n_H(r), \tag{2.32}$$

where d_s is the scale radius of the subclump and d_t is the tidal radius of the subclump.

The tidal radius of the subclump can now be derived by integrating the subclump

density as given in equation (2.32) over the volume of the subclump

$$M_{\mathrm{cl}} = \frac{8\pi}{3} M_X n_H(r) d_t^{\frac{3}{2}} \left(d_t^{\frac{3}{2}} + d_s^{\frac{3}{2}} \right) \ln \left(1 + \left(\frac{d_t}{d_s} \right)^{\frac{3}{2}} \right). \tag{2.33}$$

Based on this equation for the subclump mass it is possible to find a numerical result for the tidal radius of the subclump with respect to the subclump mass and the distance of the subclump from the Galactic Center.

Now the annihilation rate within an individual subclump with mass M_{cl} and tidal radius d_t can be derived. To avoid the unphysical divergence of the annihilation rate for $d \to 0$ for the Moore-profile an inner cutoff radius d_c has to be introduced which can be interpreted as the radius of a core with constant and finite density ρ_0 in the central region of the Moore-profile. The general formula for the annihilation rate, equation (2.9), already accounts for this possibility and a core can easily be included in the calculation for the annihilation rate. This yields an annihilation rate of

$$\begin{aligned} \mathcal{R}(r, M_{\mathrm{cl}}) = \frac{4\pi}{3} \langle \sigma v \rangle n_H^2(r) d_t^3 \left(d_t^{\frac{3}{2}} + d_s^{\frac{3}{2}} \right)^2 \Bigg\{ & \frac{1}{\left(d_c^{\frac{3}{2}} + d_s^{\frac{3}{2}} \right)^2} \\ & + \frac{2}{d_s^3} \left(3 \ln \frac{d_t}{d_c} - \ln \frac{d_t^{\frac{3}{2}} + d_s^{\frac{3}{2}}}{d_c^{\frac{3}{2}} + d_s^{\frac{3}{2}}} + \frac{d_s^{\frac{3}{2}}}{d_t^{\frac{3}{2}} + d_s^{\frac{3}{2}}} - \frac{d_s^{\frac{3}{2}}}{d_c^{\frac{3}{2}} + d_s^{\frac{3}{2}}} \right) \Bigg\} \end{aligned} \tag{2.34}$$

that is dependent on the distance of the subclump from the Galactic Center and the tidal radius of the subclump which itself depends on the subclump mass. The contribution of the flat core is constant and depends significantly on its size. Two possible extrema are given by $d_c = 0$ and $d_c = d_t$. In the first case the subclump has no flat core and the profile is a real Moore-profile with central cusp while in the second case the whole subclump has a constant density. This might occur if tidal stripping removes all mass in the outer regions of the subclump and only the flat core remains.

Based on the results of N-body simulations the subclump distribution in a galaxy is not constant and depends instead on the distance from the Galactic Center as well as on the subclump mass. It is defined in equation (2.10) and the normalisation constant for the subclump distribution is given by equation (2.12). Together with the previous result for the annihilation rate from equation (2.34) it is possible to find

an expression for the annihilation flux of the clumped SHDM

$$\mathcal{F} = \frac{\mathrm{d}N}{\mathrm{d}E}\frac{1}{r_\odot}\int_0^{r_t} \mathrm{d}r\, r \ln\frac{r + r_\odot}{|r - r_\odot|}\int_0^{\eta M_H} \mathrm{d}M_{\mathrm{cl}}\, n_{\mathrm{cl}}(r, M_{\mathrm{cl}})\mathcal{R}(r, M_{\mathrm{cl}}). \tag{2.35}$$

As for the decay and the annihilation flux it is not possible to find an analytical solution for this integral. To compute a result it is again necessary to employ numerical methods.

2.3 Subclumps with Constant Density Core

The third section of this chapter introduces a new approach for the approximation of the annihilation flux from SHDM. It abandons the assumption that the subclumps are downscaled parent halos and instead assumes that the subclumps have a constant density core. This is a very interesting possibility if tidal stripping is able to remove most of the mass in the outer regions of the subclumps [8, 10]. Then the remaining mass is mainly concentrated in the flat cores and therefore the flux originating in the core regions dominates the total flux of the subclumps and the contributions from the outer regions of the subclumps are negligible. This does not just simplify the results for the subclump calculations but more importantly introduces a simple order of magnitude prediction for the annihilation flux from the clumped component of the SHDM in our Galaxy.

The density of a subclump with a flat core can thus be defined as

$$\rho_X = \begin{cases} \nu\rho_\odot & \text{for } 0 \le d \le d_t, \\ 0 & \text{for } d > d_t, \end{cases} \tag{2.36}$$

where the core density was chosen to be a fraction ν of the density of the Sun $\rho_\odot$. The number density of the SHDM particles can be calculated from equation (2.36)

$$n_X = \nu\frac{\rho_\odot}{M_X}, \tag{2.37}$$

where the case for $d > d_t$ was neglected because the density vanishes per definition. It has to be emphasised that this choice for the subclump density does not affect the behaviour or shape of the DM halo. Unlike the sections on the NFW-profile and the Moore-profile calculations on the decay and annihilation flux from the smooth component of the DM halo are not included in this section because no assumption on the smoothly distributed fraction of the DM is made and only the contribution

from the clumped fraction is discussed.

The radius of the i-th subclump $d_{\mathrm{cl}}^{(i)}$ can be calculated by inserting the subclump density as defined in equation (2.36) into equation (2.8)

$$M_{cl}^{(i)} = \frac{4\pi}{3}\nu\rho_{\odot}{d_{\mathrm{cl}}^{(i)}}^3. \tag{2.38}$$

This equation for the cluster mass can easily be solved for the radius of the i-th subclump

$$d_{\mathrm{cl}}^{(i)} = \sqrt[3]{\frac{3M_{\mathrm{cl}}^{(i)}}{4\pi\nu\rho_{\odot}}}. \tag{2.39}$$

After the radius of the i-th subclump is known it is possible to calculate the annihilation rate in the i-th subclump by inserting equation (2.36) into the general equation for the annihilation rate in a subclump, equation (2.9),

$$\mathcal{R}\Big(M_{\mathrm{cl}}^{(i)}\Big) = \langle\sigma v\rangle\frac{\nu\rho_{\odot}M_{\mathrm{cl}}^{(i)}}{M_X^2}. \tag{2.40}$$

The annihilation cross section can be expressed as a fraction ζ of the s-wave unitary bound for a SHDM mass of $M_X = 10^{21}\,\mathrm{eV}$ and velocity $v = 100\,\mathrm{km/s}$ as discussed in [37]

$$\begin{aligned}\langle\sigma v\rangle &= \zeta \times \tfrac{4\pi\hbar^2}{M_X^2 v} \\ &= \zeta \times 4.4 \cdot 10^{-43}\,\tfrac{\mathrm{m}^3}{\mathrm{s}}.\end{aligned} \tag{2.41}$$

The annihilation flux from the subclump system is considered to be a superposition of the contributions of pointlike subclumps because their distances from the Sun are much larger than their actual radii, $r \gg d_{\mathrm{cl}}^{(i)}$. Therfore it is possible to write the total annihilation rate for the subclump distribution as a sum of annihilation rates over all individual subclumps

$$\mathcal{R}_{\mathrm{tot}}\Big(r_i, M_{\mathrm{cl}}^{(i)}\Big) = \langle\sigma v\rangle\frac{\nu\rho_{\odot}}{M_X^2}\sum_i M_{\mathrm{cl}}^{(i)}. \tag{2.42}$$

To calculate the annihilation flux from a discrete subclump distribution it is necessary to modify equation (2.13) for a continuous distribution to an equation for a discrete distribution. In this modified equation the integration over the subclump mass is replaced by a sum over all pointlike subclumps with discrete mass $M_{\mathrm{cl}}^{(i)}$. In

addition the continuous subclump distribution has to be replaced by a sum of spatial delta functions to compensate for the pointlike behaviour of the discrete subclump distribution which is different from the previously used continuous subclump distribution. With these modifications it is possible to derive the annihilation flux from a pointlike subclump distribution

$$\mathcal{F} = \frac{\mathrm{d}N}{\mathrm{d}E} \int \mathrm{d}\vec{r} \frac{1}{2\pi \left|\vec{r} - \vec{r}_{\odot}\right|^2} \delta(\vec{r} - \vec{r}_i) \mathcal{R}_{\mathrm{tot}} \left(r_i, M_{\mathrm{cl}}^{(i)} \right). \tag{2.43}$$

The spatial integration in this equation for the annihilation flux from the clumped dark matter fraction can trivially be solved due to the delta function to get an exact result of the form

$$\mathcal{F} = \frac{1}{2\pi} \frac{\mathrm{d}N}{\mathrm{d}E} \langle \sigma v \rangle \frac{\nu \rho_{\odot}}{M_X^2} \sum_i \frac{M_{\mathrm{cl}}^{(i)}}{r_i^2}, \tag{2.44}$$

where $r_i = |\vec{r}_i - \vec{r}_{\odot}|$ denotes the distance of the i-th subclump from the Sun. By inserting the explicit parametrisation of the annihilation cross section from equation (2.41) the annihilation flux can be rewritten as

$$\mathcal{F} = 2 \frac{\mathrm{d}N}{\mathrm{d}E} \zeta \nu \frac{\rho_{\odot} \hbar^2}{M_X^4 v} \sum_i \frac{M_{\mathrm{cl}}^{(i)}}{r_i^2}, \tag{2.45}$$

which depends on the product $\zeta\nu$ of the fractions of the mass of the Sun and the s-wave unitary bound. It is also dependent on the mass of the i-th subclump $M_{\mathrm{cl}}^{(i)}$ and its distance from the Galactic Center r_i, which are simulation parameters. To test the accuracy of the constant density core approximation a series of numerical simulations was performed. The results of these simulations are summarised in the following section.

2.4 Simulation Results

The first simulations for the constant density core approach were not designed to determine exact values for the annihilation flux or the product of the s-wave unitary bound fraction ζ with the fraction of the density of the Sun ν. Instead they were meant to give an insight into the relation between the clumped fraction of the SHDM ξ and the fraction of the heaviest substructure η and their influence on the number of subclumps in a simulated galaxy as well as on the product $\zeta\nu$.

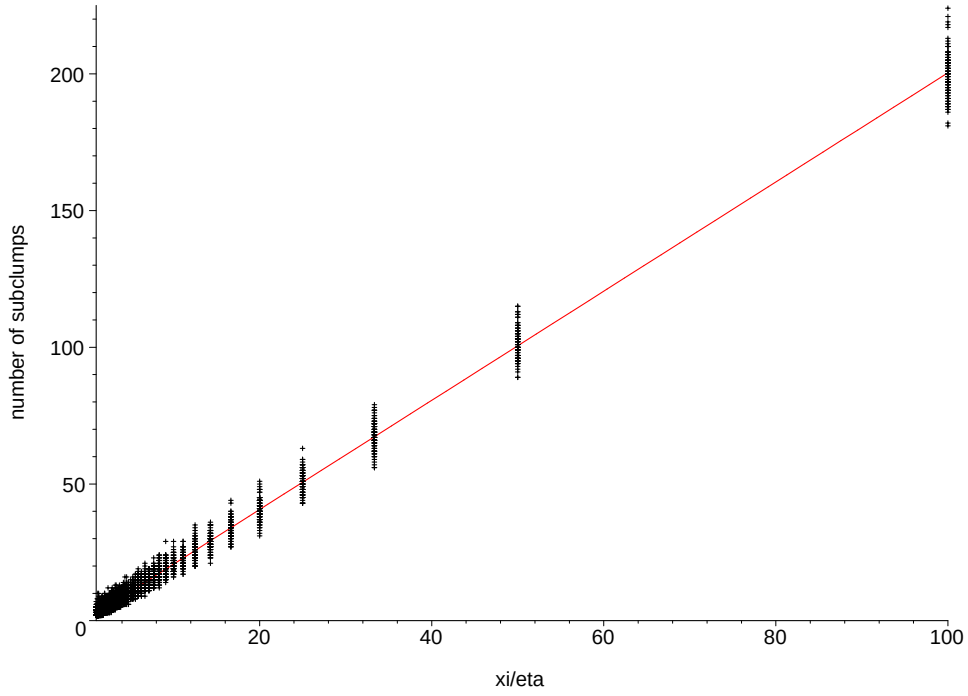

Figure 2.1: Number of subclumps in simulated galaxy 2D (low resolution). The graph shows the number of subclumps in a simulated galaxy over the ratio ξ/η together with a linear fit to the simulation results. The range of the parameters in the simulation was defined to be $0.001 \leq \xi \leq 0.1$ and $0.01\xi \leq \eta \leq \xi$.

One of the questions that arises from the beginning is how the parameters ξ and η have to be chosen to simulate a Galaxy that is similar to our own. In addition it is of immense interest whether these two parameters are independent of each other.

Therefore a simulation was performed that varied the fraction of the clumped SHDM between $0.001 \leq \xi \leq 0.1$ and the fraction of the heaviest sublump between $0.01\xi \leq \eta \leq \xi$. For each combination of ξ and η the number of subclumps in the simulated system was derived. A brief look at the results shows that the parameters ξ and η are not independent of each other. To demonstrate this dependence Figure 2.1 displays the number of subclumps in the simulated galaxy over the ratio ξ/η. It clearly shows that the number of subclumps is linearly dependent on the ratio ξ/η. The graph also reveals that the most interesting range for simulating a Galaxy similar to our own is given by $50 \leq \xi/\eta \leq 100$ where the number of subclumps in the simulation is of the order of the number of Globular Clusters in our Galaxy.

To improve the resolution in the range of interest it is necessary to decrease the interval length. Therefore a second simulation was performed that kept the parameter $\xi = 0.1$ fixed and only varied the fraction of the heaviest substructure.

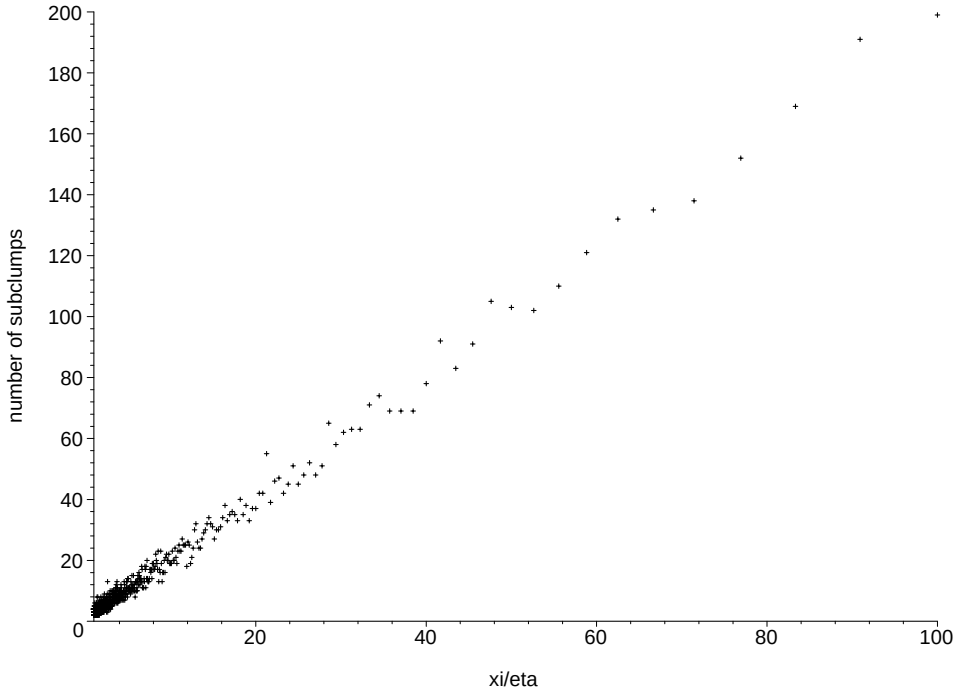

Figure 2.2: Number of subclumps in simulated galaxy 1D (high resolution). The graph displays the number of subclumps in a simulated galaxy over the ratio ξ/η. The parameter $\xi = 0.1$ was chosen to be constant while η was varied within a range of $0.001\xi \leq \eta \leq \xi$.

This time the interval was chosen to be larger than before $0.001\xi \leq \eta \leq \xi$ and the interval length was decreased. In addition to the number of subclumps the improved simulation also calculated the annihilation flux and more importantly the product $\zeta\nu$. The result for the calculation of the number of subclumps is shown in Figure 2.2. It confirms the range of interest that was determined by the first simulation and verifies the previously mentioned linear relation between the number of substructures and the ratio ξ/η throughout the whole range of interest. The trend of the relation shown in the graph also indicates that the measurements for $\xi/\eta \leq 10$ have to be treated very carefully due to the low number of high mass substructures which are prone to domination by one cluster located nearby. Therefore further analysis has to be restricted to simulation data with $\xi/\eta \geq 5$.

A value for the product $\zeta\nu$ can be derived by computing the total flux of a system of SHDM substructures for a specific energy, chosen to be 10^{20} eV for the simulations, and comparing the results to the measurements published by the AGASA and HiRes groups, which are $3 \cdot 10^{24}\,\mathrm{eV^2 m^{-2} s^{-1} sr^{-1}}$. These results are displayed in Figure 2.3 where the common logarithm of the product $\zeta\nu$ is displayed over the ratio between

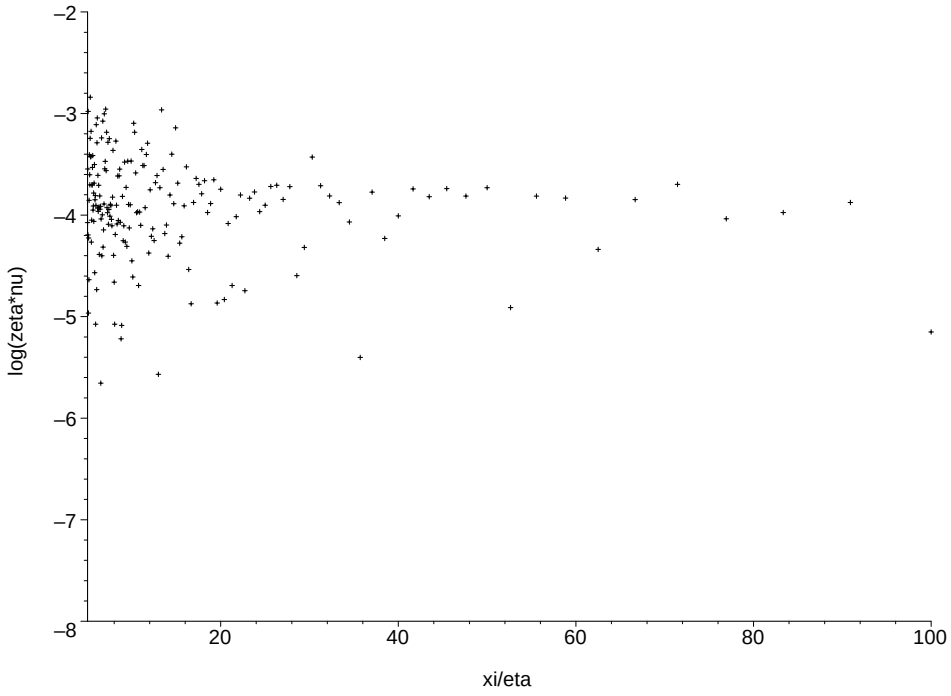

Figure 2.3: $\zeta\nu$ in simulated galaxies. The graph displays the product $\zeta\nu$ over the ratio ξ/η for a range of $5 \leq \xi/\eta \leq 100$. The parameter $\xi = 0.1$ was chosen to be constant while the fraction of the heaviest subclump was varied between $0.001\xi \leq \eta \leq \xi$.

ξ and η. The graph shows clearly that some scattering of the results between $-6 \leq \log_{10}(\zeta\nu) \leq -3$ occurs at the lower end of the ratio between ξ and η. But within the range for the ratio that can reproduce the amount of substructure in our Galaxy the scatter is much smaller and the product is given by $-4.5 \leq \log_{10}(\zeta\nu) \leq -3.5$. These final results are slightly smaller than $\zeta\nu = 10^{-3}$ given in [37] which is considered a conservative upper limit of the product.

Chapter 3

DM-Profile for Globular Clusters

The most important step in the calculation of the UHECR flux from DM in GC-like objects is to determine which density profile they have because these calculations are crucially dependent on the shape of the profile. This can be done by fitting the most prominent DM profiles to the GC data in the catalogue by Harris. Within the scope of this thesis fits to the NFW-profile with core, Moore-profile with core, King-profile, isothermal profile with core, NFW-profile, and Moore-profile are performed.

For all of the previously mentioned dark matter distributions it is possible to verify theoretically whether a fit to the measurements is possible or not. This verification process differs slightly between the profiles discussed but the overall procedure is the same for all of them.

Initially the calculations in this chapter were supposed to determine which of the chosen dark matter profiles fits the data best. Surprisingly it has turned out that none of the commonly used dark matter profiles was able to satisfactorily explain the Globular Cluster data. Therefore this chapter is now intended to prove the failure of these profiles and pave the way for a new approach. A new profile with variable inner power law index that is able to fit the Globular Cluster data is then introduced in Chapter 4.

Before the fit of the individual dark matter profiles to the data is discussed in the corresponding subchapters the general progression of calculations is briefly outlined. The first step is to specify the dark matter distribution to be fit. The difference in the radial behaviour between cusped profiles and profiles with core makes it necessary to define their general profiles separately. For cusped profiles, like the NFW-profile and the Moore-profile, the density distribution diverges for $d = 0$ and is otherwise

given by

$$\rho(d) = \rho_{\text{model}}(d) \quad \text{for } d > 0, \tag{3.1}$$

where a core density ρ_0 can be defined from the normalisation of the profile. For the cuspy profiles the core density has no physical meaning and it is nothing other than a normalisation constant but it proves to be useful for further calculations. Similarly, the density distribution for the profiles with core is defined as

$$\rho(d) = \begin{cases} \rho_0 & \text{for } d \leq d_c, \\ \rho_{\text{model}}(d) & \text{for } d > d_c, \end{cases} \tag{3.2}$$

where ρ_{model} are the density distributions for the NFW-profile with core, Moore-profile with core, King-profile, and isothermal profile with core. In this case the density is constant throughout the core while it is radially dependent if the radius is larger than the core radius. It has to be mentioned that although the density is defined separately for the two regions it is continuous at the boundary $\lim_{d \to d_c} \rho\,(d) = \rho_0$.

After the separate definition of cuspy profiles and profiles with core the following equations are written in a general form that can be used independent of the actual shape of the profiles. Integration over the volume of the Globular Cluster yields its mass. Due to spherical symmetry of all commonly used dark matter profiles the spatial integration can be simplified to a radial integral and the mass of a Globular Cluster is given by

$$M_{\text{GC}} = 4\pi \int_0^{d_t} \mathrm{d}d\, \rho(d) d^2, \tag{3.3}$$

where the tidal radius d_t acts as an upper cutoff radius. Based on the fact that a core density is defined for all investigated profiles it is possible to introduce a structure parameter

$$\delta = \frac{M_{\text{GC}}}{\rho_0}, \tag{3.4}$$

that can be dependent on the core radius, the scale radius, and the tidal radius. This structure parameter is the constant of proportionality between the cluster mass and the core density. The core radius and the tidal radius are given by Harris while the scale radius is the only parameter missing to calculate the structure parameter δ. Instead the set of data contains the half mass radius d_h that can be used to calculate

the scale radius by utilising the following equation for the half mass of a Globular Cluster

$$\frac{M_{\mathrm{GC}}}{2} = 4\pi \int_0^{d_h} \mathrm{d}d\, \rho(d) d^2. \tag{3.5}$$

For profiles with constant density core it is necessary to treat the two cases for $d_h \leq d_c$,(I) in the further discussion, and $d_h > d_c$, (II), separately because the integration over the volume yields different results for the half mass due to the change in the radial dependence of the density distribution at d_c. The calculations for the coreless profiles do not require a case separation because there is no change in the radial dependence and therefore the result for the half mass is unique. Equation (3.5) can then be solved for the structure parameter δ as well. The only major difference to the result from equation (3.4) is that the structure parameter is now dependent on the half mass radius instead of the tidal radius. Therefore the results for the mass and half mass imply an equation for each of the two cases, $d_h \leq d_c$ and $d_h > d_c$, that has the scale radius as the only unknown parameter.

To draw a conclusion as to whether the data can be fit by a profile, two basic requirements have to be fulfilled. Firstly the relations that are implied by equations (3.3) and (3.5) have to be solvable for the scale radius, which is automatically satisfied for the King-profile and the isothermal profile. In addition the solutions for the scale radius have to be in a reasonable range. By applying the least stringent assumption that the scale radius has to be at least as big as the core radius and cannot exceed the tidal radius this range is given by $d_c \leq d_s \leq d_t$. Secondly the measured relations between the core radius, the half mass radius and the tidal radius have to agree with the theoretically derived ranges that are implied by the DM profile. If one of these basic requirements is not fulfilled the analysed dataset cannot be fit by the investigated profile. This implies that if a large number of datasets from the catalogue does not meet the requirements the DM profile cannot be fit successfully to the data. Further restrictions arise from the tidal forces acting on a Globular Cluster that can disrupt the Globular Cluster completely within a few orbits if its tidal radius is smaller than approximately twice the scale radius, $d_t < 2d_s$ [29, 13].

3.1 Navarro, Frenk, and White-profile with core

The first profile to be considered is the NFW-profile with constant density core. It is derived from the cuspy NFW-profile by introducing a constant density core in the

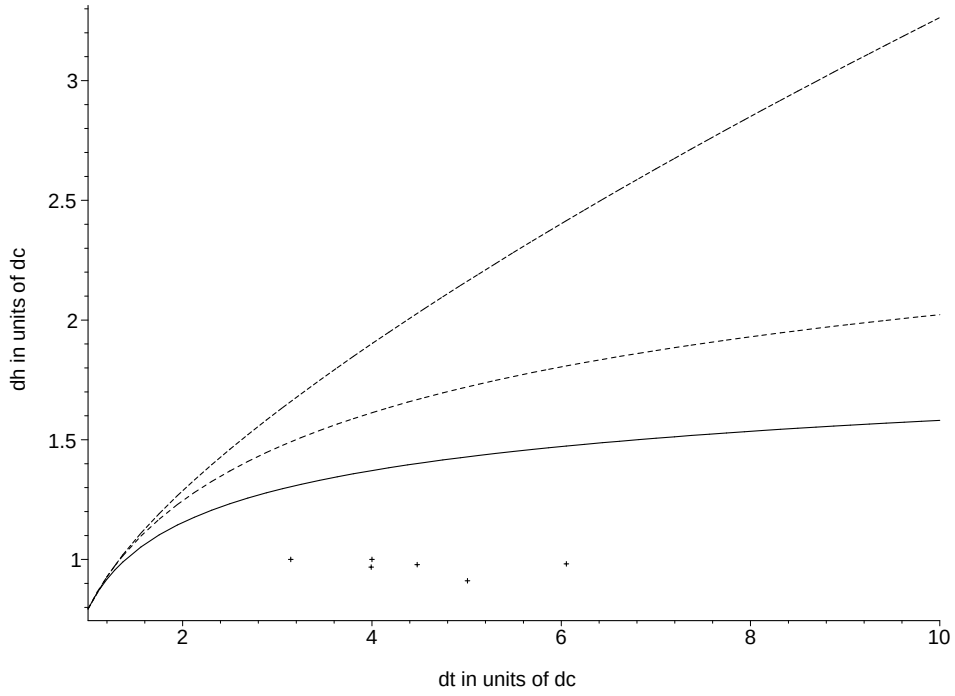

Figure 3.1: Relationships between d_h and d_t for the NFW-profile with core for the case $d_h \leq d_c$. The three lines represent numerical solutions to equation (3.9, I) for $d_s = 0$ (solid, lower line), $d_s = d_c$ (dotted, middle line), and $d_s = d_t$ (dashed, upper line). The points display the measured relations for the Globular Clusters.

center of a NFW-profile. The density distribution is therefore given by

$$\rho(d) = \begin{cases} \rho_0 & \text{for } d \leq d_c, \\ \rho_0 \frac{d_c (d_c + d_s)^2}{d (d + d_s)^2} & \text{for } d > d_c, \end{cases} \tag{3.6}$$

where the core density ρ_0 was defined to be equal to the density of the cuspy NFW-profile at the core radius d_c.

The cluster mass can now be calculated by integrating equation (3.3) over the radius where the profile was replaced by the NFW-profile with core as specified in equation (3.6)

$$M_{\mathrm{GC}} = \frac{4\pi}{3} \rho_0 \left(d_c^3 + 3 d_c \left(d_c + d_s \right)^2 \left(\frac{d_s}{d_t + d_s} - \frac{d_s}{d_c + d_s} + \ln \frac{d_t + d_s}{d_c + d_s} \right) \right). \tag{3.7}$$

The core radius and the tidal radius are given but the scale radius is unknown. Instead the catalogue by Harris contains the half mass radius with which the scale radius can be calculated by using equation (3.5) for the half mass of a Globular

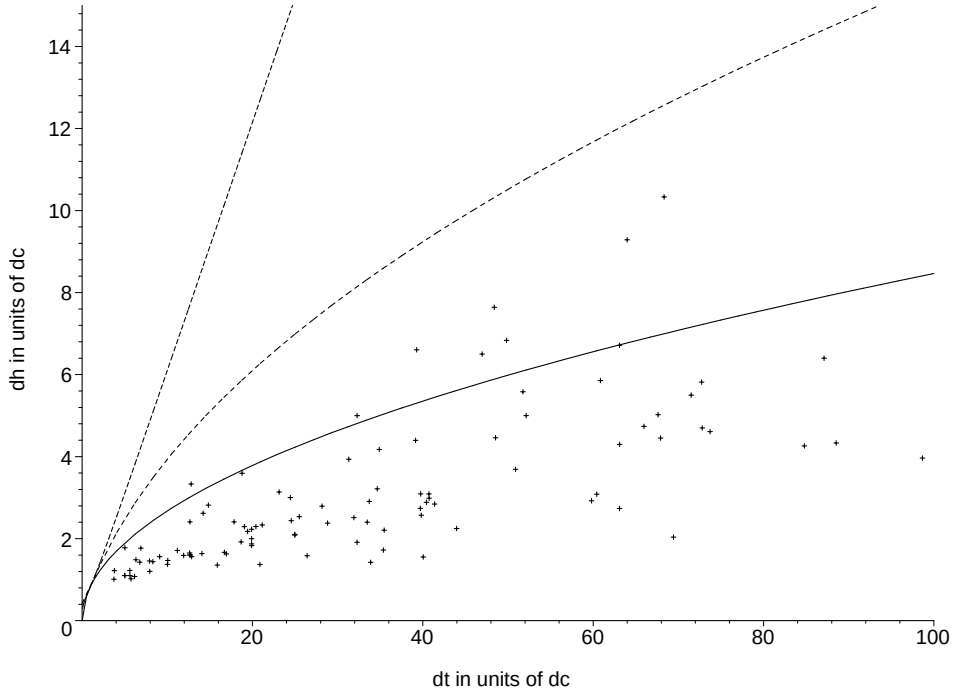

Figure 3.2: Relationships between d_h and d_t for the NFW-profile with core for the case $d_h > d_c$. The three lines represent numerical solutions to equation (3.9, II) for $d_s = 0$ (solid, lower line), $d_s = d_c$ (dotted, middle line), and $d_s = d_t$ (dashed, upper line). The points display the measured relations for the Globular Clusters.

Cluster

$$\frac{M_{\mathrm{GC}}}{2} = \begin{cases} \frac{4\pi}{3}\rho_0 d_h^3 & , d_h \leq d_c, \\ \frac{4\pi}{3}\rho_0 \left(d_c^3 + 3d_c \left(d_c + d_s\right)^2 \left(\frac{d_s}{d_h+d_s} - \frac{d_s}{d_c+d_s} + \ln \frac{d_h+d_s}{d_c+d_s} \right) \right) & , d_h > d_c. \end{cases} \tag{3.8}$$

Together with the equation for the mass these equations for the half mass imply relations that have the scale radius as the only unknown parameter

$$0 = \begin{cases} 2d_h^3 - 1 - 3\left(1 + d_s\right)^2 \left(\frac{d_s}{d_t+d_s} - \frac{d_s}{1+d_s} + \ln \frac{d_t+d_s}{1+d_s} \right) & , d_h \leq d_c, \\ 1 + 3\left(1 + d_s\right)^2 \left(\frac{2d_s}{d_h+d_s} - \frac{d_s}{d_t+d_s} - \frac{d_s}{1+d_s} + \ln \frac{(d_h+d_s)^2}{(1+d_s)(d_t+d_s)} \right) & , d_h > d_c, \end{cases} \tag{3.9}$$

where all radii are normalised to units of the core radius to further simplify the equations. Thus it is possible to derive solutions for the scale radius that are dependent on the core radius, the half mass radius and the tidal radius. To determine the parameter range within which valid solutions for the scale radius exist it proves to be useful to analyse the relations between the half mass radius and the tidal radius at the boundaries of the physically meaningful range of the scale radius. For con-

d_t	5	10	30	50	100
d_h for (Ia)	1.428	1.581	1.776	1.854	1.949
d_h for (Ib)	2.160	3.263	6.528	9.099	14.350
d_h for (IIa)	1.893	2.677	4.636	5.986	8.465
d_h for (IIb)	3.101	6.102	18.212	30.342	60.672

Table 3.1: Half mass radii and tidal radii for the NFW-profile with constant density core. The table summarises numerical results for the half mass radius from equation (Ia), (Ib), (IIa), and (IIb) for a range of values for the tidal radius. All radii are normalised to units of the core radius.

venience the equations were evaluated for $d_s = 0$, (a) unless otherwise stated, and $d_s = d_t$, (b), which is slightly bigger than the actual valid range for the scale radius $d_c \leq d_s \leq d_t$. Evaluation of (I) at the boundaries leads to the following solutions

$$\begin{aligned}
&\text{(Ia) } d_s \to 0 : \; 0 = 2d_h^3 - 1 - 3\ln d_t \\
&\qquad d_h = \sqrt[3]{\tfrac{1}{2} + \tfrac{3}{2}\ln d_t} \quad \text{for } 0.717 \leq d_t \leq 1.396, \\
&\text{(Ib) } d_s \to d_t : \; 0 = 2d_h^3 - 1 - 3\left(d_t+1\right)^2\left(\tfrac{1}{2} - \tfrac{d_t}{d_t+1} + \ln\tfrac{2d_t}{d_t+1}\right) \\
&\qquad d_h = \sqrt[3]{\tfrac{5}{4} - \tfrac{3}{4}d_t^2 + \tfrac{3}{2}\left(d_t+1\right)^2\ln\tfrac{2d_t}{d_t+1}} \quad \text{for } 0.675 \leq d_t \leq 1.329.
\end{aligned} \tag{3.10}$$

Similar results can be derived for (II)

$$\begin{aligned}
&\text{(IIa) } d_s \to 0 : \; 0 = 1 + 3\ln\tfrac{d_h^2}{d_t} \\
&\qquad d_h = \sqrt{d_t}e^{-\frac{1}{6}} \quad \text{for } d_t > 1.396, \\
&\text{(IIb) } d_s \to d_t : \; 0 = \tfrac{d_t(d_t+1)^2}{d_t+d_h} - \tfrac{3}{2}d_t^2 - 2d_t - \tfrac{1}{6} + \left(d_t+1\right)^2\ln\tfrac{(d_t+d_h)^2}{2d_t(d_t+1)} \\
&\qquad d_h = \exp\left(\text{LambertW}\left(-e^{\xi(d_t)}d_t\right) - \xi(d_t)\right) - d_t \quad \text{for } d_t > 1.329,
\end{aligned} \tag{3.11}$$

where the term in the Lambert W function is given by

$$\xi\left(d_t\right) = -\frac{1}{12}\left(6\ln\left(2d_t\left(d_t+1\right)\right) + \frac{9d_t^2 + 12d_t + 1}{\left(d_t+1\right)^2}\right) \tag{3.12}$$

to shorten the notation. In all cases the half mass radius is given as a function of the tidal radius. The range of the tidal radius can then be calculated from the solution for the half mass radius by additionally including the restrictions that are implied by the range of the half mass radius, $0 \leq d_h \leq d_c$ or $d_h > d_c$, for which the equations are valid.

For the NFW-profile with constant density core the first requirement is fulfilled because it is possible to derive parameter ranges for the core radius, half mass radius,

d_t	5	10	30	50	100
d_h for (Ia)	1.428	1.581	1.776	1.854	1.949
d_h for (Ib)	1.992	2.806	4.850	6.260	8.851
d_h for (IIa)	1.893	2.677	4.636	5.986	8.465
d_h for (IIb)	2.919	5.657	16.728	27.828	55.599

Table 3.2: Half mass radii and tidal radii for the Moore-profile with constant density core. The table summarises numerical results for the half mass radius from equation (Ia), (Ib), (IIa), and (IIb) for a range of values for the tidal radius. All radii are normalised to units of the core radius.

and tidal radius within which solutions for the scale radius exist. The theoretical relations for the NFW-profile with core are displayed in Figure 3.1 for $d_h \leq d_c$ and in Figure 3.2 for $d_h > d_c$ together with the datapoints for the measured Globular Clusters in our Galaxy. Furthermore numerical solutions for the half mass radius for a range of common tidal radii are summarised in Table 3.1. They give the numerical values of the boundary functions for $d_s = 0$ and $d_s = d_t$ at the specified tidal radii. It turns out that none of the measurements displayed in Figure 3.1 falls in the right parameter range. A similar result is found from the observation of Figure 3.2 where only a few measurements fall in the extended parameter range which is given by the numerical solutions of equation (3.11) for $d_s = 0$, represented by the solid line, and $d_s = d_t$, dashed line, while none of the datasets falls in the physically meaningful range between the curves for $d_s = d_c$, dotted line, and $d_s = d_t$. Therefore it can be concluded that the second assumption is violated and the data cannot be fit by a NFW-profile with constant density core.

3.2 Moore-profile with core

The Moore-profile with constant density core is the second profile considered. In analogy to the NFW-profile with core it is derived from the Moore-profile by modifying the density distribution in the central region such that it exhibits a constant density core rather than a central cusp

$$\rho(d) = \begin{cases} \rho_0 & \text{for } d \leq d_c, \\ \rho_0 \dfrac{d_c^{\frac{3}{2}} \left(d_s^{\frac{3}{2}} + d_c^{\frac{3}{2}} \right)}{d^{\frac{3}{2}} \left(d^{\frac{3}{2}} + d_s^{\frac{3}{2}} \right)} & \text{for } d > d_c. \end{cases} \tag{3.13}$$

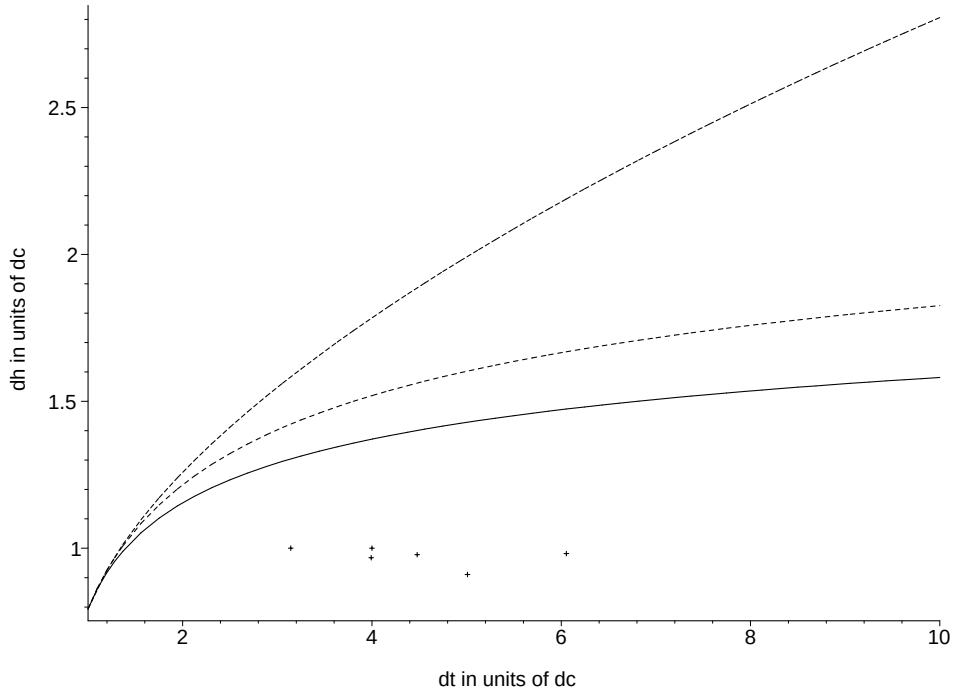

Figure 3.3: Relationships between d_h and d_t for the Moore-profile with core for the case $d_h \leq d_c$. The three lines represent numerical solutions to equation (3.9, I) for $d_s = 0$ (solid, lower line), $d_s = d_c$ (dotted, middle line), and $d_s = d_t$ (dashed, upper line). The points display the measured relations for the Globular Clusters.

The core density was chosen to be equal to the density of the coreless profile at the core radius.

To derive an equation for the mass of a Globular Cluster the general density distribution in equation (3.3) has to be replaced by equation (3.13) for the Moore-profile with constant density core and the radial integral has to be solved. The mass of the Globular Cluster is thus given by

$$M = \frac{4\pi}{3}\rho_0 \left(d_c^3 + 2d_c^{\frac{3}{2}} \left(d_c^{\frac{3}{2}} + d_s^{\frac{3}{2}} \right) \ln \frac{d_t^{\frac{3}{2}} + d_s^{\frac{3}{2}}}{d_c^{\frac{3}{2}} + d_s^{\frac{3}{2}}} \right) \tag{3.14}$$

and is dependent on the unknown scale radius. Therefore it is necessary to find a relation between the scale radius and the given parameters of the cluster. This can be done by utilising the half mass of the Globular Cluster. Integration of the density distribution to the half mass radius yields the following equations for the half mass

$$\frac{M}{2} = \begin{cases} \frac{4\pi}{3}\rho_0 d_h^3 & , d_h \leq d_c, \\ \frac{4\pi}{3}\rho_0 \left(d_c^3 + 2d_c^{\frac{3}{2}} \left(d_c^{\frac{3}{2}} + d_s^{\frac{3}{2}} \right) \ln \frac{d_h^{\frac{3}{2}} + d_s^{\frac{3}{2}}}{d_c^{\frac{3}{2}} + d_s^{\frac{3}{2}}} \right) & , d_h > d_c. \end{cases} \tag{3.15}$$

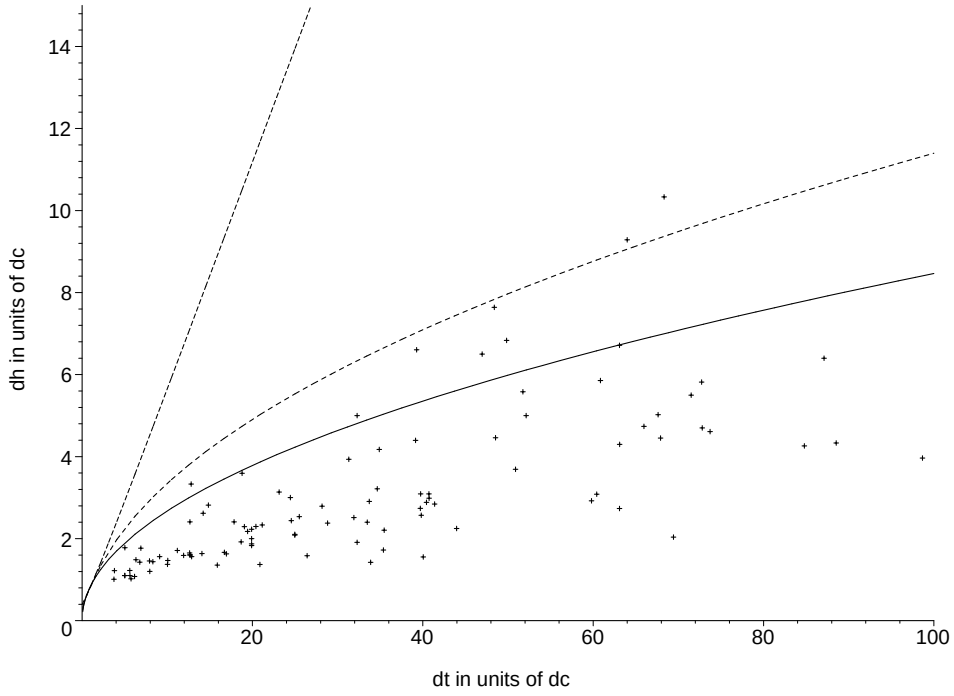

Figure 3.4: Relationships between d_h and d_t for the Moore-profile with core for the case $d_h \leq d_c$. The three lines represent numerical solutions to equation (3.9, II) for $d_s = 0$ (solid, lower line), $d_s = d_c$ (dotted, middle line), and $d_s = d_t$ (dashed, upper line). The points display the measured relations for the Globular Clusters.

Together with the equation for the cluster mass these equations can be used to eliminate the mass and the core density

$$0 = \begin{cases} 1 - 2d_h^3 + 2\left(1 + d_s^{\frac{3}{2}}\right) \ln \frac{d_t^{\frac{3}{2}} + d_s^{\frac{3}{2}}}{1 + d_s^{\frac{3}{2}}} & , d_h \leq d_c, \\ 1 + 2\left(1 + d_s^{\frac{3}{2}}\right) \ln \frac{\left(d_h^{\frac{3}{2}} + d_s^{\frac{3}{2}}\right)^2}{\left(1 + d_s^{\frac{3}{2}}\right)\left(d_t^{\frac{3}{2}} + d_s^{\frac{3}{2}}\right)} & , d_h > d_c. \end{cases} \tag{3.16}$$

These equations contain the scale radius as the only unknown parameter and depend otherwise only on the known core radius, half mass radius and tidal radius. As in the previous section all radii are normalised to units of the core radius to simplify the equations for further analysis. The easiest way to determine the parameter range within which a solution for the scale radius exists is to evaluate the equations at the boundaries of the range for the scale radius. The valid range for the scale radius was previously defined to be $d_c \leq d_s \leq d_t$ but to simplify the results the functions will be evaluated at the boundaries of the somewhat bigger interval $0 \leq d_s \leq d_t$.

For the first case, $d_h \leq d_c$, of equation (3.16) the evaluation at the boundaries

yields

$$
\begin{aligned}
&(Ia)\ d_s \to 0 :\ 0 = 1 - 2d_h^3 + 3\ln d_t \\
&\qquad d_h = \sqrt[3]{\tfrac{1}{2} + \tfrac{3}{2}\ln d_t} \quad \text{for } 0.717 \leq d_t \leq 1.396, \\
&(Ib)\ d_s \to d_t :\ 0 = 1 - 2d_h^3 + 2\left(1 + d_t^{\frac{3}{2}}\right)\ln \tfrac{2d_t^{\frac{3}{2}}}{1+d_t^{\frac{3}{2}}} \\
&\qquad d_h = \sqrt[3]{\tfrac{1}{2} + \left(1 + d_t^{\frac{3}{2}}\right)\ln \tfrac{2d_t^{\frac{3}{2}}}{d_t^{\frac{3}{2}}+1}} \quad \text{for } 0.689 \leq d_t \leq 1.341.
\end{aligned}
\tag{3.17}
$$

The same calculations can then be repeated for the second case, $d_h > d_c$, which produces the following results

$$
\begin{aligned}
&(IIa)\ d_s \to 0 :\ 0 = 1 + 3\ln \tfrac{d_h^2}{d_t} \\
&\qquad d_h = e^{-\frac{1}{6}}\sqrt{d_t} \quad \text{for } d_t > 1.396, \\
&(IIb)\ d_s \to d_t :\ 0 = 1 + 2\left(1 + d_t^{\frac{3}{2}}\right)\ln \frac{\left(d_h^{\frac{3}{2}} + d_t^{\frac{3}{2}}\right)^2}{2d_t^{\frac{3}{2}}\left(1+d_t^{\frac{3}{2}}\right)} \\
&\qquad d_h = \left(e^{-4\left(1+d_t^{\frac{3}{2}}\right)}\sqrt{2\left(1 + d_t^{\frac{3}{2}}\right)d_t^{\frac{3}{2}} - d_t^{\frac{3}{2}}}\right)^{\frac{2}{3}} \quad \text{for } d_t > 1.341.
\end{aligned}
\tag{3.18}
$$

The numerical values for the four boundary solutions are then combined in Table 3.2. Besides the numerical representation the same solutions are displayed in Figure 3.3 and 3.4. They clearly indicate that none of the datasets with $d_h \leq d_c$ agrees with the theoretically derived relations. In addition only a few measurements for $d_h > d_c$ fall in the theoretically allowed parameter range. It has to be mentioned that the agreement between the theoretical relations and the data seems to be better than for the NFW-profile with core. Overall it turns out that most of the datasets in the Harris catalogue do not agree with the valid parameter range for the half mass radius and the tidal radius with respect to the core radius. This implies that the second requirement is violated and the measured data cannot be fit by a Moore profile with a constant density core and has to be rejected as well.

3.3 King-profile

After excluding the two already analysed dark matter profiles with constant density core another established dark matter profile, the King-profile, is considered. As for the former cases the calculations are based on the assumption that all Globular

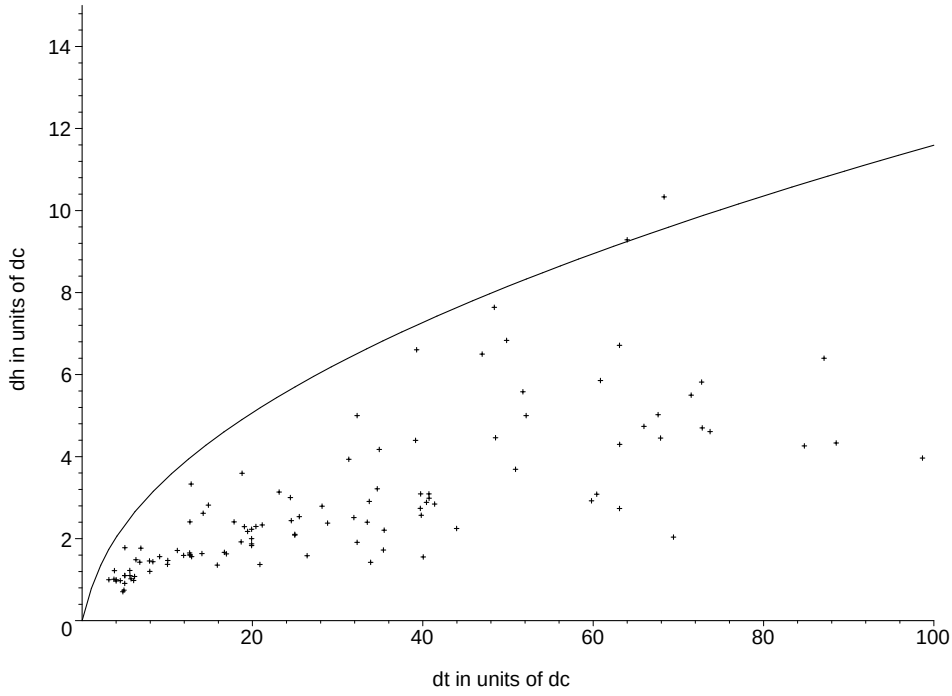

Figure 3.5: Relationship between d_h and d_t for the King-profile. The solid line represents the numerical solution to equation (3.22). The points display the measured relations for the Globular Clusters.

Clusters can be fit by a King-profile

$$\rho(d) = \frac{\rho_0 d_c^3}{(d^2 + d_c^2)^{\frac{3}{2}}} \quad \text{for } d \geq 0. \tag{3.19}$$

For the King profile it is not necessary to perform a case separation because the profile does not have a central cusp, is defined continuously throughout the whole range of interest of the radial parameter, and the core density is given automatically as the density at the center of the cluster $\lim_{d \to 0} \rho(d) = \rho_0$.

The mass of a cluster is derived by inserting the King-profile as specified in equation (3.19) into equation (3.3) for the cluster mass and integrating over the radius

$$M = 4\pi\rho_0 d_c^3 \left(-\frac{d_t}{\sqrt{d_t^2 + d_c^2}} + \ln \frac{d_t + \sqrt{d_t^2 + d_c^2}}{d_c} \right). \tag{3.20}$$

In contrast to the previously discussed profiles the King profile is independent of the scale radius and solely depends on the known values for the core radius and the tidal radius. On the first glance this relation seems to be the missing link between the mass

d_t	5	10	30	50	100
d_h	2.338	3.490	6.269	8.153	11.594

Table 3.3: Half mass radii and tidal radii for the King-profile. The table summarises numerical results for the half mass radius for a range of values for the tidal radius. All radii are normalised to units of the core radius.

of a cluster and its core density, because it does not depend on an unknown scale radius and the first requirement as outlined in the general discussion is trivially fullfilled. It only has to be shown that the theoretical relations between the core radius, the half mass radius and the tidal radius agree with the measured relations between these parameters. This can again be done by using the equation for the half mass. Due to the continuity of the density distribution there exists only one equation for the half mass and no case separation is necessary. Thus the half mass is given by

$$\frac{M}{2} = 4\pi\rho_0 d_c^3 \left(-\frac{d_h}{\sqrt{d_h^2 + d_c^2}} + \ln \frac{d_h + \sqrt{d_h^2 + d_c^2}}{d_c} \right). \tag{3.21}$$

Equations (3.20) and (3.21) can now both be solved for the structure parameter δ to eliminate the cluster mass and the core density from the resulting relation

$$0 = \frac{2d_h}{\sqrt{d_h^2 + 1}} - \frac{d_t}{\sqrt{d_t^2 + 1}} + \ln \frac{d_t + \sqrt{d_t^2 + 1}}{\left(d_h + \sqrt{d_h^2 + 1}\right)^2}. \tag{3.22}$$

Again all radii are normalised to units of the core radius. This equation can neither be solved exactly for the half mass radius nor for the tidal radius. Instead it is necessary to solve the equation numerically for the half mass radius. This can easily be done and the results for a range of tidal radii are summarised in Table 3.3.

To compare the result as derived from equation (3.22) with the measurements it is useful to display them together in a graph. The combination of theoretical and experimental data is shown in Figure 3.5. Since the density distribution is independent of the scale radius the relation between the half mass radius and the tidal radius is unique instead of an area in parameter space. By looking at the graph it turns out that only two datapoints are located above the theoretical line while all other datapoints lie below. In addition the bulk of the measurements indicates that the theoretical line should be much lower than the theoretical solution for the King

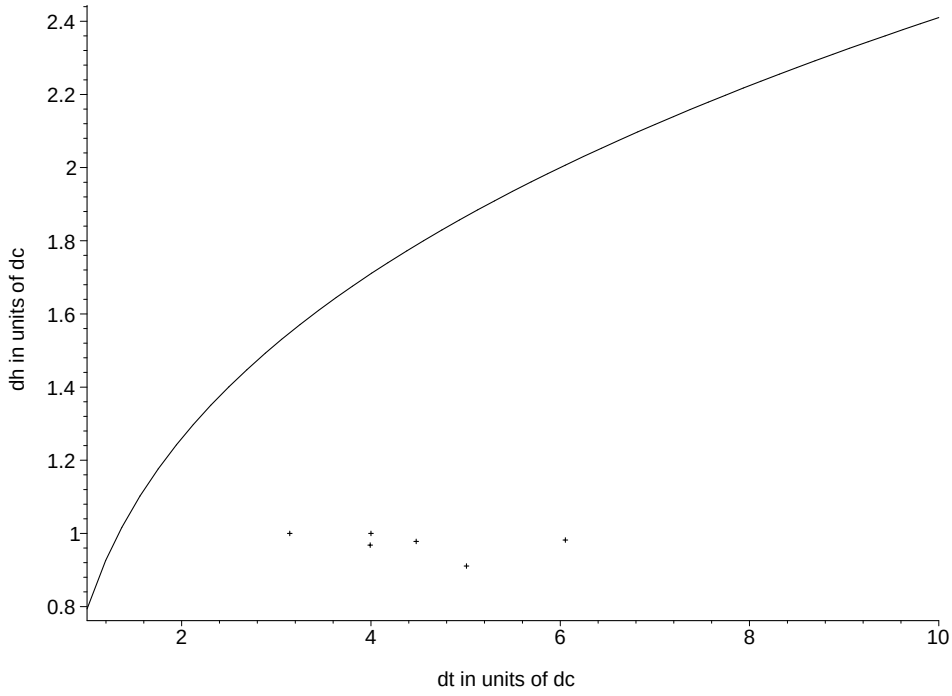

Figure 3.6: Relationship between d_h and d_t for the isothermal profile with core for the case $d_h \leq d_c$. The line represents the numerical solutions to equation (3.26, I). The points display the measured relations for the Globular Clusters.

profile predicts. Therefore it can be concluded that the King profile is not able to explain the measurements and has to be discarded as well.

3.4 Isothermal profile with core

The isothermal profile with constant density core is the last cored profile considered, although, its behaviour for large radii does not meet the widely accepted d^3 dependence for dark matter structures. Instead the isothermal profile with core is proportional to d^2 for large radii and the density is given by

$$\rho(d) = \begin{cases} \rho_0 & \text{for } d \leq d_c, \\ \rho_0 \frac{d_c^2}{d^2} & \text{for } d > d_c, \end{cases} \tag{3.23}$$

where the core density ρ_0 is chosen to be equal to the density of the cuspy isothermal profile at the core radius.

Integration of the density distribution over the volume of the cluster yields a

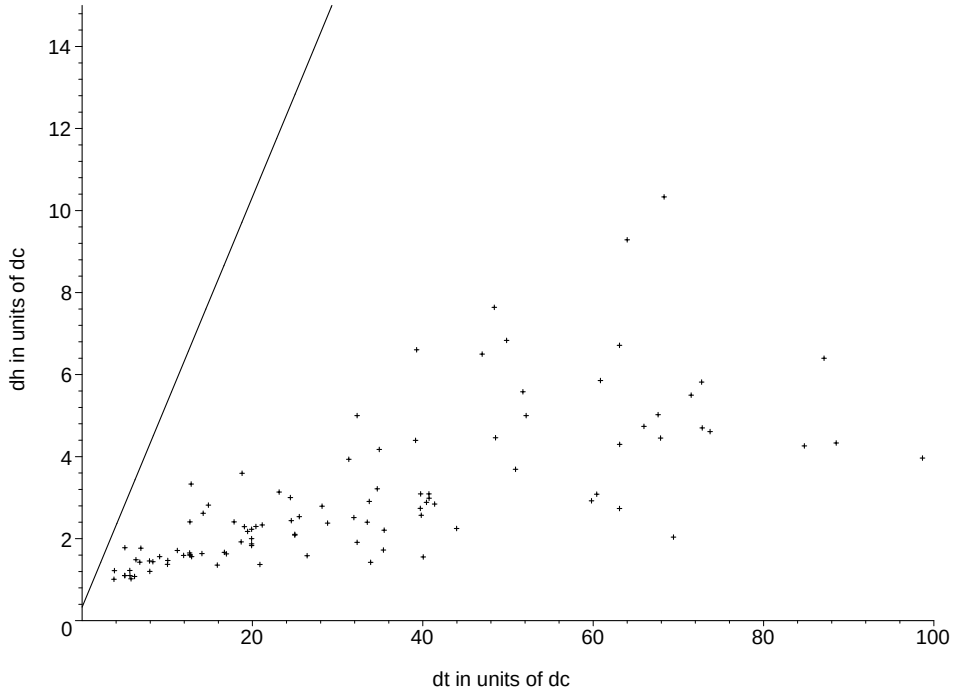

Figure 3.7: Relationship between d_h and d_t for the isothermal profile with core for the case $d_h > d_c$. The line represents the numerical solutions to equation (3.26, II). The points display the measured relations for the Globular Clusters.

cluster mass of

$$M = \frac{4\pi}{3}\rho_0 \left(3d_t d_c^2 - 2d_c^3\right). \tag{3.24}$$

The cluster mass depends only on the known core radius and tidal radius and could therefore easily be calculated from measurements. To verify the fit of the profile to the data it is necessary to derive theoretical relations between the core radius, half mass radius, and tidal radius and compare them with the measured relations between these parameters. To find an equation that relates all known parameters of interest and eliminates the cluster mass as well as the core density the half mass of the cluster has to be taken into account

$$\frac{M}{2} = \begin{cases} \frac{4\pi}{3}\rho_0 d_h^3 & , d_h \leq d_c, \\ \frac{4\pi}{3}\rho_0 \left(3d_h d_c^2 - 2d_c^3\right) & , d_h > d_c. \end{cases} \tag{3.25}$$

Setting the equations for the mass and the half mass equal to each other leads to the following relations that have to be fulfilled if the measured parameters for the core radius, the half mass radius and the tidal radius are supposed to agree with the

d_t	5	10	30	50	100
d_h for $d_h \leq d_c$	1.866	2.410	3.530	4.198	5.301
d_h for $d_h > d_c$	2.833	5.333	15.333	25.333	50.333

Table 3.4: Half mass radii and tidal radii for the isothermal profile with constant density core. The table summarises numerical results for the half mass radius from equation (I) and (II) for a range of values for the tidal radius. All radii are normalised to units of the core radius.

conditions implied by the isothermal profile with core

$$0 = \begin{cases} \frac{3}{2}d_t - 1 - d_h^3 & , d_h \leq d_c, \\ 3d_t + 2 - 6d_h & , d_h > d_c. \end{cases} \tag{3.26}$$

Once again all radii are normalised to units of the core radius. These equations can easily be solved for the half mass radius

$$\begin{aligned} &(I) \quad d_h = \sqrt[3]{\tfrac{3}{2}d_t - 1} \quad , \tfrac{2}{3} \leq d_t \leq \tfrac{4}{3}, \\ &(II)\ d_h = \tfrac{1}{2}d_t + \tfrac{1}{3} \qquad , d_t > \tfrac{4}{3}. \end{aligned} \tag{3.27}$$

In Table 3.4 the results for the half mass radius are displayed for a range of common values for the tidal radius. Furthermore the derived theoretical relations between the half mass radius and the tidal radius are plotted together with the Globular Cluster data in Figure 3.6 for $d_h \leq d_c$ and in Figure 3.7 for $d_h > d_c$. Due to the fact that the isothermal profile is independent of the scale radius the result for each of the cases is unique.

Figure 3.6 reveals that all datapoints for $d_h \leq d_c$ lie significantly below the theoretical relation. The same can be concluded from Figure 3.7 for the datapoints with $d_h > d_c$ and the data suggests a gradient that is much shallower than for the one of the theoretical curve. Because of the considerably worse agreement between the theoretical curve and the data than for the previously considered profiles the conclusion can be drawn that the data cannot be fit by an isothermal profile with core. Moreover this result supports the general belief that profiles with a radial behaviour different from d^3 on large scales are inappropriate to explain the Globular Cluster data.

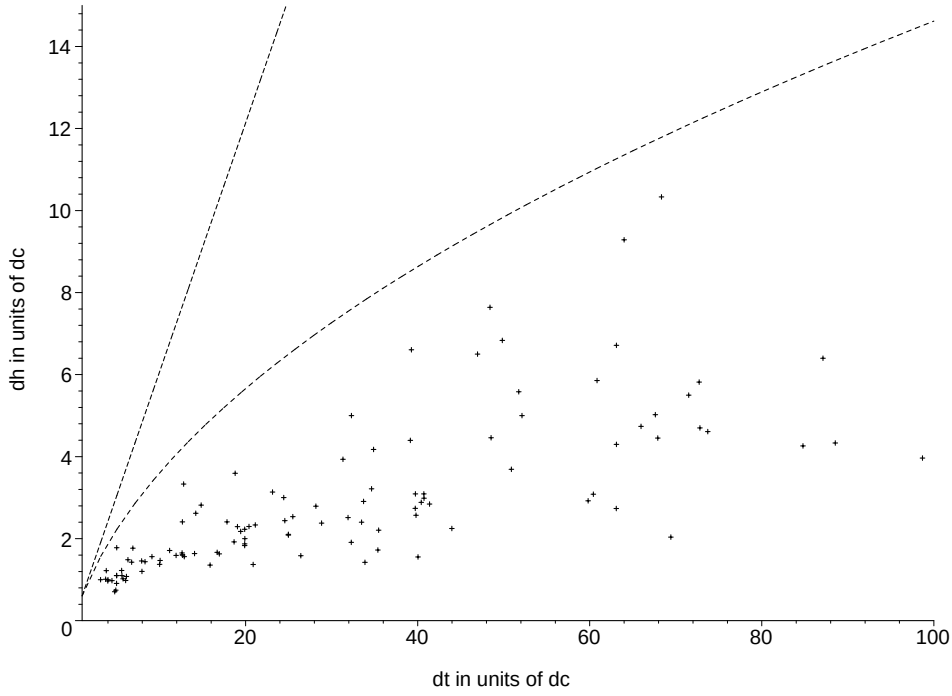

Figure 3.8: Relationships between d_h and d_t for the NFW-profile. The two lines represent numerical solutions to equation (3.31) for $d_s = d_c$ (dotted, lower line) and $d_s = d_t$ (dashed, upper line). The points display the measured relations for the Globular Clusters.

3.5 Navarro, Frenk, and White-profile

After not one of the dark matter profiles with finite density core, discussed in the previous sections, was able to explain the Globular Cluster data it is time to consider the possibility that the data can be fit to one of the common dark matter profiles with central cusp. The most prominent and for this reason first to be probed cuspy dark matter profile is the NFW-profile

$$\rho(d) = \frac{\rho_0 d_s^3}{d\,(d+d_s)^2}, \tag{3.28}$$

which was introduced in Section 1.2 and extensively discussed in Chapter 2. It has the same radial behaviour for the entire range of interest. Therefore there is no need for a case separation as for the NFW-profile with constant density core.

The total mass can be derived by integrating equation (3.3) but it is easier to adapt the previously deduced result for the mass of a dark matter halo from equation

(2.15)

$$M_{\mathrm{GC}} = 4\pi\rho_0 d_s^3 \left(\ln \frac{d_t + d_s}{d_s} - \frac{d_t}{d_t + d_s} \right). \tag{3.29}$$

In opposition to the profiles with core the cluster mass is independent of the core radius, which is not surprising for a cuspy profile. Instead it is only dependent on the tidal radius and the yet to be determined scale radius. In analogy to the calculations for the profiles with core the half mass can be employed to eliminate the cluster mass and the core density from the equations. It is given by

$$\frac{M_{\mathrm{GC}}}{2} = 4\pi\rho_0 d_s^3 \left(\ln \frac{d_h + d_s}{d_s} - \frac{d_h}{d_h + d_s} \right). \tag{3.30}$$

Both equations for the mass, equation (3.29), and half mass, equation (3.30), can be solved for the structure parameter δ and set equal to each other. This leads to the following relation that has the scale radius as the only unknown parameter

$$0 = \frac{2d_h}{d_h + d_s} - \frac{d_t}{d_t + d_s} + \ln \frac{d_s \left(d_t + d_s\right)}{\left(d_h + d_s\right)^2}. \tag{3.31}$$

While the radii for the cored profiles were normalised to units of the core radius to simplify the calculations this renormalisation does not affect the complexity because the equation is independent of the core radius. Anyway, the radii are normalised to units of the core radius to keep the results compatible with the results for the profiles with core.

Another modification that was used to simplify the calculations for the cored profiles is the slight extension of the allowed range of the scale radius to $0 \leq d_s \leq d_t$. For the NFW-profile this extension is not feasible because the equation diverges for $d \to 0$ and the equation has to be evaluated at the physically meaningful boundaries of the scale radius. This complicates the calculation but is necessary to make sure that the results remain reasonable. The solutions of equation (3.31) at the boundaries are therefore given by

$$\begin{aligned}
&(a)\ d_s \to 1 : 0 = \tfrac{2d_h}{d_h+1} - \tfrac{d_t}{d_t+1} + \ln \tfrac{d_t+1}{(d_h+1)^2} \\
&\quad d_h = \exp\left\{\mathrm{LambertW}\left(-e^{\xi_1(d_t)}\right) - \xi_1(d_t)\right\} - 1 \quad \text{for } d_t \geq 0, \\
&(b)\ d_s \to d_t : 0 = \tfrac{2d_h}{d_h+d_t} - \tfrac{1}{2} + \ln \tfrac{2d_t^2}{(d_h+d_t)^2} \\
&\quad d_h = \exp\left\{\mathrm{LambertW}\left(-d_t e^{\xi_2(d_t)}\right) - \xi_2(d_t)\right\} - d_t \quad \text{for } d_t \geq 0,
\end{aligned} \tag{3.32}$$

d_t	5	10	30	50	100
d_h for $d_s = d_c$	2.217	3.606	7.266	9.843	14.619
d_h for $d_s = d_t$	3.033	6.067	18.201	30.334	60.669

Table 3.5: Half mass radii and tidal radii for the NFW-profile. The table summarises numerical results for the half mass radius from equation (a) and (b) for a range of values for the tidal radius. All radii are normalised to units of the core radius.

where the functions $\xi_1(d_t)$ and $\xi_2(d_t)$ in the LambertW functions are defined as

$$\begin{aligned} \xi_1(d_t) &= -\tfrac{1}{2}\left(\ln\left(d_t+1\right) + \tfrac{d_t+2}{d_t+1}\right), \\ \xi_2(d_t) &= -\tfrac{3}{4} - \tfrac{1}{2}\ln\left(2d_t^2\right). \end{aligned} \tag{3.33}$$

The numerical results for the boundary functions, (a) and (b), for a range of tidal radii are summarised in Table 3.5. Additionally the theoretical solutions are plotted together with the Globular Cluster data in Figure 3.8. The graph shows clearly that all datapoints lie below the theoretically expected are in parameter space for the half mass radius and the tidal radius. Therefore it is obvious that the Globular Cluster data cannot be fit successfully by a NFW-profile.

3.6 Moore-profile

So far all analysed profiles failed to explain the Globular Cluster data. The Moore-profile which was discussed at length in Chapter 2 is the last remaining profile to be tested

$$\rho(d) = \frac{\rho_0 d_s^3}{d^{\frac{3}{2}}\left(d^{\frac{3}{2}} + d_s^{\frac{3}{2}}\right)}. \tag{3.34}$$

The cluster mass can again be calculated by executing the radial integration of equation (3.3) but as for the NFW-profile it is more convenient to modify the result for the mass of a dark matter halo from equation (2.28)

$$M = \frac{8}{3}\pi\rho_0 d_s^3 \ln\frac{d_t^{\frac{3}{2}} + d_s^{\frac{3}{2}}}{d_s^{\frac{3}{2}}}. \tag{3.35}$$

To eliminate the cluster mass and the core density from the equation it is again necessary to utilise the half mass which can easily be written down in analogy to the

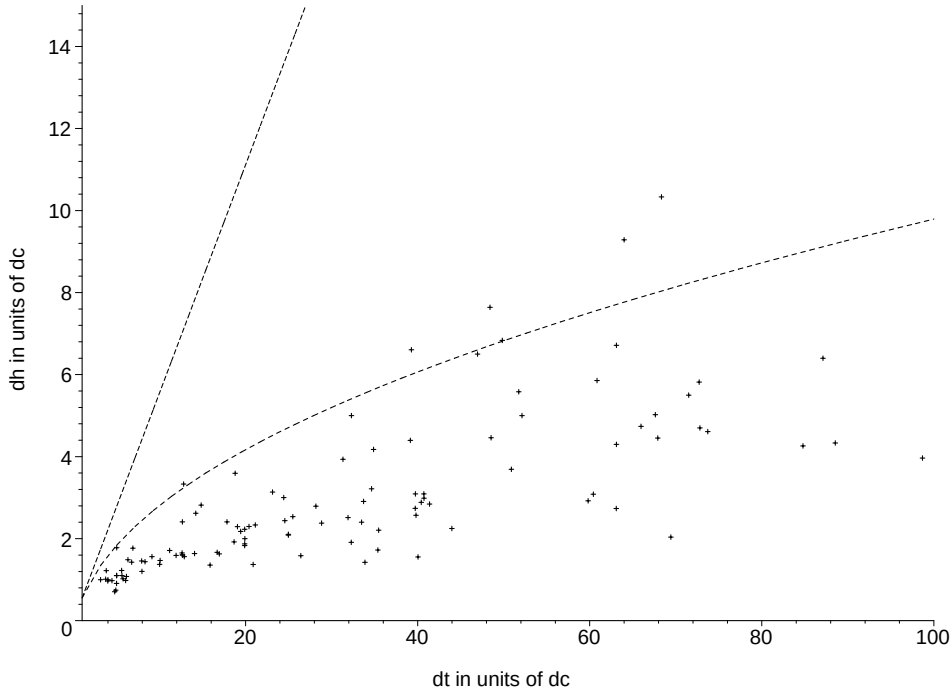

Figure 3.9: Relationship between d_h and d_t for the Moore-profile. The two lines represent numerical solutions to equation (3.37) for $d_s = d_c$ (dotted, lower line) and $d_s = d_t$ (dashed, upper line). The points display the measured relations for the Globular Clusters.

result for the cluster mass

$$\frac{M}{2} = \frac{8}{3}\pi\rho_0 d_s^3 \ln \frac{d_h^{\frac{3}{2}} + d_s^{\frac{3}{2}}}{d_s^{\frac{3}{2}}}. \tag{3.36}$$

This result is again unambiguous because the density distribution for the Moore profile in equation (3.34) is defined continuously for $d \geq 0$.

Equations (3.35) and (3.36) yield the following relation with the scale radius as the only unknown parameter

$$0 = \left(d_t^{\frac{3}{2}} + d_s^{\frac{3}{2}}\right) d_s^{\frac{3}{2}} - \left(d_h^{\frac{3}{2}} + d_s^{\frac{3}{2}}\right)^2. \tag{3.37}$$

To be consistent with previous results all radii are normalised to units of the core radius although the equation is not directly dependent on the core radius. Afterwards it is evaluated at the boundaries. As for the NFW-profile it is impossible to use the mathematically easier extended range of the scale radius because for $d \to 0$ the equation only has the trivial solution. The solutions of the equation at the boundaries

d_t	5	10	30	50	100
d_h for $d_s = d_c$	1.837	2.810	5.200	6.825	9.791
d_h for $d_s = d_t$	2.778	5.557	16.670	27.783	55.567

Table 3.6: Half mass radii and tidal radii for the Moore-profile. The table summarises numerical results for the half mass radius from equation (a) and (b) for a range of values for the tidal radius. All radii are normalised to units of the core radius.

are given by

$$\begin{aligned}
&(a)\ d_s \to 1 : \ 0 = \left(d_t^{\frac{3}{2}} + 1\right) - \left(d_h^{\frac{3}{2}} + 1\right)^2 \\
&\qquad d_h = \left(\sqrt{d_t^{\frac{3}{2}} + 1} - 1\right)^{\frac{2}{3}} \quad \text{for } d_t \geq 0, \\
&(b)\ d_s \to d_t : \ 0 = 2d_t^3 - \left(d_h^{\frac{3}{2}} + d_t^{\frac{3}{2}}\right)^2 \\
&\qquad d_h = d_t \left(\sqrt{2} - 1\right)^{\frac{2}{3}} \quad \text{for } d_t \geq 0.
\end{aligned} \tag{3.38}$$

They are displayed in Figure 3.9 together with the Globular Cluster data. In addition to the graphical representation the numerical values for the boundary functions for specific values of the tidal radius are given in Table 3.6.

A brief inspection of the graph shows that a few datasets can be explained by the Moore-profile. Nevertheless most datasets are still significantly below the allowed parameter range and the data cannot be fit to a Moore-profile. Although the profile failed to explain the data it has to be mentioned that the agreement between data and theory is better than for any of the previously discussed profiles.

3.7 Conclusions

The calculations for the six different dark matter profiles show that the Globular Cluster data by Harris cannot be explained by fitting one of the common density profiles to the data. This is valid for the considered profiles with constant density core as well as for the cuspy profiles.

The discussion of the dark matter profiles shows that the analysed profiles proportional to d^3 provide a better fit to the data than profiles with different large scale proportionality. This finding seems to confirm the widely accepted fact that dark matter structures are proportional to d^3 on large scales. It has to be pointed out that within the scope of this thesis it is not intended to make any predictions about the exact large scale behaviour of dark matter structures due to the limited number

of probed profiles.

Furthermore it was shown that the agreement between the assumed profile and the measured data improved for profiles with higher values for the inner power law index α. The profile with the highest value for the inner power law index considered in the analysis, the Moore-profile with $\alpha = 1.5$, also seemed to have the best agreement with the data. Nevertheless, most of the datasets were located significantly below the predicted parameter space and the Moore-profile clearly failed to explain the measurements.

For these reasons it is necessary to find a profile that can fit the measured data and furthermore preserves the widely accepted condition that the outer power law index is proportional to d^3. The most straightforward possibility to comply with these requirements and to minimise changes to existing profiles is to go one step back and examine the general density distribution specified in equation (1.3). This general equation is the basis of the NFW-profile, $\alpha = 1$, and the Moore-profile, $\alpha = 1.5$, by choosing discrete values for the inner power law index α. Assuming a variable inner power law index maintains the large scale behaviour for dark matter structures and in addition opens the possibility for higher values of the inner power law index that are needed to further improve the agreement between the Globular Cluster data and the theory.

Chapter 4

Profile with Variable α

In the previous Chapter it was shown that the data by Harris cannot be explained by the most commonly used DM profiles. Some of these profiles are closely related to the general profile specified in equation (1.3) by choosing well defined values for the inner power law index α, while the outer power law index γ remains fixed to $\gamma = 3$ to comply with the observed d^3 behaviour for large radii. A simple modification to the general profile should not change the behaviour for large radii and also fit the measured data. This can be done by assuming a variable inner power law index α. The density distribution is then given by

$$\rho(d) = \begin{cases} \rho_0 & \text{for } d \leq d_c, \\ \rho_0 \frac{d_c^\alpha (d_s + d_c)^{3-\alpha}}{d^\alpha (d_s + d)^{3-\alpha}} & \text{for } d > d_c, \end{cases} \tag{4.1}$$

where the core density ρ_0 is chosen to be equal to the density of the coreless profile at the core radius of the GC.

Abandoning the universal profile paradigm where a universal inner power law index explains dark matter structures on all scales seems to be a tremendous loss in simplicity but in reality a variable inner power law index comes at an astonishingly low cost. The calculations still follow the outline given in Chapter 3 to a large extent and only minor modifications are necessary to compensate for the additional variable α.

The cluster mass can still be calculated by integrating the density over the volume of the cluster. Although the density distribution depends on a variable inner power law index it is possible to find an exact solution. This solution can be expressed with hypergeometric functions. To simplify the notation for hypergeometric functions the

abbreviation

$$\mathrm{F}(\alpha, x) \equiv \mathrm{F}\left(3-\alpha, 3-\alpha; 4-\alpha; -x\right) \tag{4.2}$$

will be used unless otherwise stated. A definition for the hypergeometric function can be found in [38]. The equation for the total mass of the cluster can thus be written as

$$M_{\mathrm{GC}} = \frac{4\pi}{3}\rho_0 d_c^3 \left(1 + \frac{3\left(d_s + d_c\right)^{3-\alpha}}{(3-\alpha)\, d_s^{3-\alpha}} \left(\left(\frac{d_t}{d_c}\right)^{3-\alpha} \mathrm{F}\left(\alpha, \frac{d_t}{d_s}\right) - \mathrm{F}\left(\alpha, \frac{d_c}{d_s}\right)\right)\right). \tag{4.3}$$

As for the other profiles with constant density core it is necessary to distinguish between two possibilities for the half mass. Therefore the half mass can be written as

$$\frac{M_{\mathrm{GC}}}{2} = \begin{cases} \frac{4}{3}\pi\rho_0 d_h^3 & , d_h \leq d_c, \\ \frac{4\pi}{3}\rho_0 d_c^3 \left(1 + \frac{3(d_s+d_c)^{3-\alpha}}{(3-\alpha)d_s^{3-\alpha}}\right. & \\ \quad \left. \times \left(\left(\frac{d_h}{d_c}\right)^{3-\alpha} \mathrm{F}\left(\alpha, \frac{d_h}{d_s}\right) - \mathrm{F}\left(\alpha, \frac{d_c}{d_s}\right)\right)\right) & , d_h > d_c. \end{cases} \tag{4.4}$$

In the first case, (I) in the further discussion, it is assumed that the half mass radius is smaller than or equal to the core radius, while in the second case, (II), the half mass radius is assumed to be bigger than the core radius.

With equations (4.3) and (4.4) it is possible to derive equations with the inner power law index and the scale radius as unknown parameters

$$0 = \begin{cases} 1 - 2\left(\frac{d_h^3}{d_c}\right)^3 + \frac{3}{3-\alpha}\left(\frac{d_s+d_c}{d_s}\right)^{3-\alpha} & \\ \quad \times \left(\left(\frac{d_t}{d_c}\right)^{3-\alpha} \mathrm{F}\left(\alpha, \frac{d_t}{d_s}\right) - \mathrm{F}\left(\alpha, \frac{d_c}{d_s}\right)\right) & , d_h \leq d_c, \\ 1 - \frac{3}{3-\alpha}\left(\frac{d_s+d_c}{d_s}\right)^{3-\alpha} \left(\left(\frac{d_t}{d_c}\right)^{3-\alpha} \mathrm{F}\left(\alpha, \frac{d_t}{d_s}\right)\right. & \\ \quad \left. -2\left(\frac{d_h}{d_c}\right)^{3-\alpha} \mathrm{F}\left(\alpha, \frac{d_h}{d_s}\right) + \mathrm{F}\left(\alpha, \frac{d_c}{d_s}\right)\right) & , d_h > d_c. \end{cases} \tag{4.5}$$

As previously stated it is not intended, and as long as no further knowledge on the scale radius is implied impossible, to find an exact solution for the inner power law index. Instead it is planned to determine a range for the inner power law index within which valid solutions for the scale radius can be found that agree with the measured data.

To avoid excluding valid ranges for the inner power law index a conservative

assumption on the possible range of the scale radius was chosen that restricts the scale radius to the physically meaningful range $d_c \leq d_s \leq d_t$. Because it is only intended to confine the valid parameter range it is sufficient to solve each equation from (4.5) twice, once by replacing the scale radius with the lower boundary value and once with the upper one. Therefore each of the initial cases, (I) and (II), has to be split again into two separate cases, where (a) denotes equations that occur for $d_s \to d_c$ and (b) denotes equations that occur for $d_s \to d_t$. The obtained results for the inner power law index specify the whole possible range for the inner power law index that agrees with the measurements. To simplify the notation even further it is useful to normalise all radii to units of the core radius. This leaves us with the following four equations.

$$\begin{aligned} &\text{(Ia)}\colon 0 = 1 - 2d_h^3 + \tfrac{3\cdot 2^{3-\alpha}}{3-\alpha}\left(d_t^{3-\alpha}\mathrm{F}(\alpha, d_t) - \mathrm{F}(\alpha, 1)\right) \\ &\text{(Ib)}\colon 0 = 1 - 2d_h^3 + \tfrac{3}{3-\alpha}\left(\tfrac{d_t+1}{d_t}\right)^{3-\alpha}\left(d_t^{3-\alpha}\mathrm{F}(\alpha, 1) - \mathrm{F}\left(\alpha, \tfrac{1}{d_t}\right)\right) \end{aligned} \tag{4.6}$$

$$\begin{aligned} &\text{(IIa)}\colon 0 = 1 - \tfrac{3\cdot 2^{3-\alpha}}{3-\alpha}\left(d_t^{3-\alpha}\mathrm{F}(\alpha, d_t) - 2d_h^{3-\alpha}\mathrm{F}(\alpha, d_h) + \mathrm{F}(\alpha, 1)\right) \\ &\text{(IIb)}\colon 0 = 1 - \tfrac{3}{3-\alpha}\left(\tfrac{d_t+1}{d_t}\right)^{3-\alpha}\left(d_t^{3-\alpha}\mathrm{F}(\alpha, 1) - 2d_h^{3-\alpha}\mathrm{F}\left(\alpha, \tfrac{d_h}{d_t}\right) + \mathrm{F}\left(\alpha, \tfrac{1}{d_t}\right)\right) \end{aligned} \tag{4.7}$$

Now that the theoretical relations to determine the range of the inner power law index are known it is necessary to have a closer look at the measurements itself. The dataset by Harris contains all currently known 150 GCs in our Galaxy. 9 of those had to be excluded from the beginning because their datasets were incomplete. A brief inspection of the remaining 141 datasets shows that $d_h > d_c$ for 133 GCs and therefore equations (4.7) have to be used, while $d_h \leq d_c$ for the remaining 8 GCs where equations (4.6) have to be used.

It turns out that solutions can be found for nearly all complete datasets, except for 7 of the datasets for $d_h > d_c$ and 2 of the datasets for $d_h \leq d_c$, that have to be excluded from the further discussion as well. For these 9 datasets it is possible that the measurements of one or several parameters are incorrect or they recently got disturbed by interactions with other sufficiently heavy objects in our Galaxy. Another distant possibility could be the presence of an Intermediate Mass Black Hole in the centre of these GCs as discussed by [35]. Due to the limited size of the analysed sample with only 5 candidates that might, but not necessarily must have an IMBH in their center, this possibility is highly speculative. Nonetheless it should not be discarded before further conclusive results are available.

This detected conformity with the data is an impressive improvement compared to the dark matter profiles analysed in Chapeter 3 because 132 out of 141 Globular

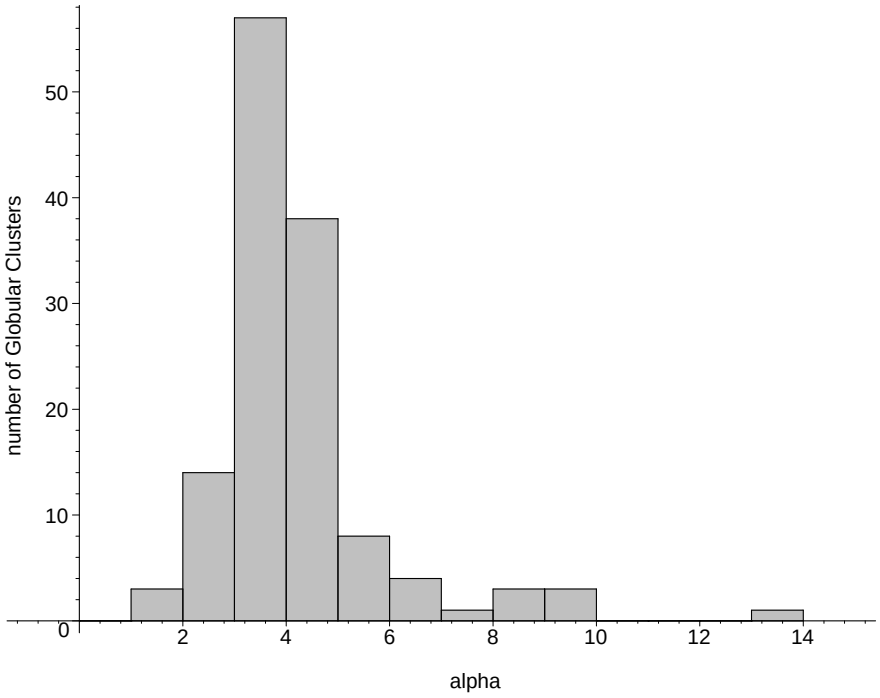

Figure 4.1: Averaged inner power law index of the Globular Clusters. The histogram plot shows the number of Globular Clusters over the averaged inner power law index. A bin contains all Globular Clusters with an averaged inner power law index of $\alpha_{\min} \leq \alpha < \alpha_{\max}$.

Clusters with complete datasets can be explained by a profile with variable inner power law index.

The results for the calculations of the inner power law index are displayed in Figure 4.1. It shows the number of GCs that have an averaged inner power law index over the inner power law index. The averaged inner power law index is defined to be the center of the maximum valid range for the inner power law index that yields a solution for the scale radius. From the histogram plot it can be visually determined that most of the GCs have an averaged inner power law index of $3 \leq \alpha \leq 5$. This is significantly steeper than for the NFW-profile with $\alpha = 1$ or the Moore-profile with $\alpha = 1.5$. The weighted mean of the inner power law index was then calculated to be $\alpha = 3.27 \pm 0.48$. This confirms the first visual impression of $\alpha \approx 4$. It also has to be pointed out that for most Globular Clusters the smallest inner power law index possible is still bigger than for the NFW- and the Moore-profile.

With these results it is possible to calculate the scale radii of the clusters. This is done by reinserting the results for the averaged inner power law index, as well as the values for the core radius and the tidal radius, into equations (4.5) and solving

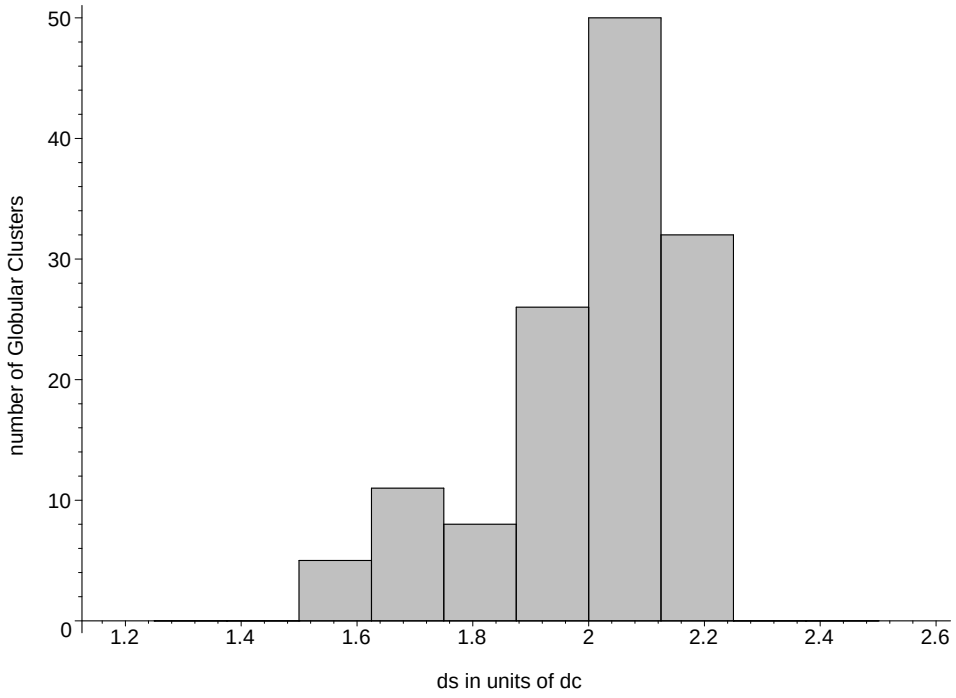

Figure 4.2: Scale radius of the Globular Clusters. The histogram plot shows the number of Globular Clusters over the scale radius in units of the core radius. A bin contains all Globular Clusters with a scale radius of $d_{\min} \leq d_s < d_{\max}$.

them this time for the scale radius. The results for the scale radius are displayed in Figure 4.2. The histogram plot displays the number of clusters over the scale radius normalised to units of the core radius. It turns out that the scale radius is always between $1.5d_c \leq d_s \leq 2.25d_c$ with a maximum at $d_s = 2d_c$. This outcome is unexpected due to the wide range of results for the averaged inner power law index. However, it offers the opportunity to approximate the scale radius to $d_s \approx 2d_c$ without introducing a significant source of error. This simplification would make the rather complicated and time consuming calculation of the exact solution for the scale radius superfluous.

Chapter 5

Core Density of Globular Clusters

After the annihilation flux from SHDM was discussed in Chapter 2 and the profile of dark matter in Globular Clusters was examined at length in Chapters 3 and 4 the intent of this chapter is to outline the calculation of the core density of GCs based on the data given by Harris. The outcome of this evaluation is of immense importance for the computation of the decay and annihilation flux from GC-like SHDM subclumps because it is strongly dependent on the core density.

The derivation is difficult because the masses of GCs which are fundamental parameters for the calculation of the core densities are not directly accessible to measurements. Instead the masses of the Globular Clusters can be calculated from the following formula if the velocity dispersions of the clusters are known

$$M = 2.5\frac{v^2 d_h}{GM_\odot},$$

where r_h is the half mass radius, v is the 3D velocity dispersion of the Globular Cluster, and the mass M is normalised to units of solar masses. It is essential to emphasise the dependence on the 3D velocity dispersion because experiments can only measure the velocity dispersion in one dimension. Thus it has to be replaced with a 1D velocity dispersion that is given by $v^2 = 3v_{\mathrm{disp}}^2$, where the 1D velocity dispersion is conveniently denoted as v_{disp}

$$M = 7.5\frac{v_{\mathrm{disp}}^2 d_h}{GM_\odot}. \tag{5.1}$$

Up to now there are no measurements available for the velocity dispersions of Globular Clusters in our Galaxy. This problem can be circumvented by two assumptions that will be introduced in the next few paragraphs.

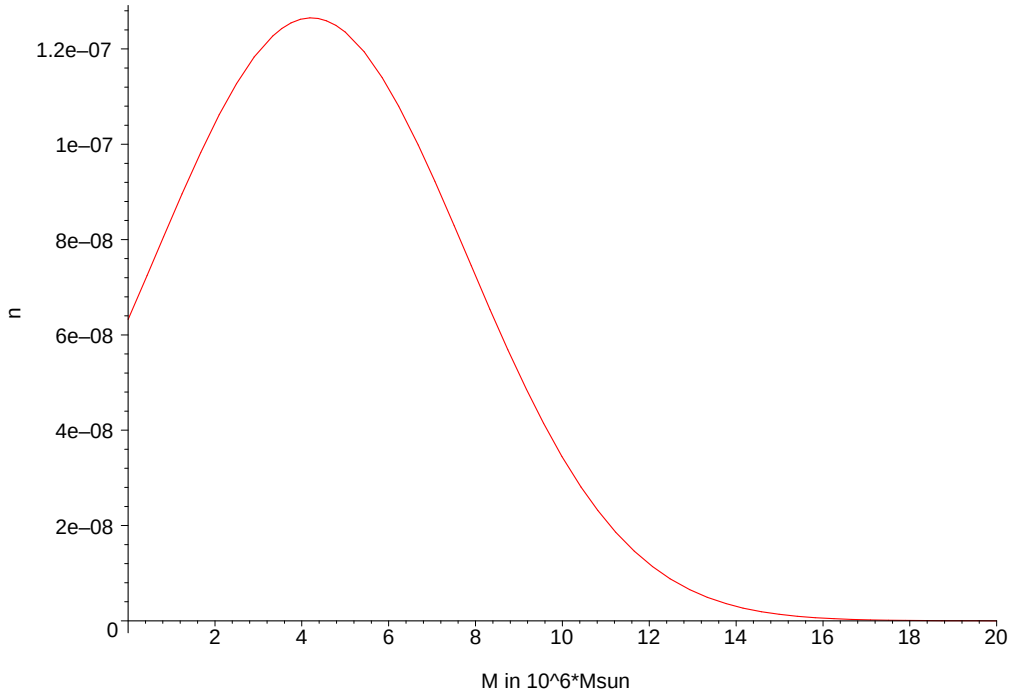

Figure 5.1: Normalised Gaussian mass distribution. The graph shows the normalised Gaussian mass distribution for the first Globular Cluster of the Harris catalogue. It represents the possibility of the Globular Cluster having a certain mass over the mass in units of $10^6\,M_\odot$.

As a first step an educated guess can be made by assuming that velocity dispersions of Globular Clusters are comparable to those of Nuclear Clusters, although, Nuclear Clusters are thought to be heavier by about one order of magnitude. The range of velocity dispersions for Nuclear Clusters of late type spirals was measured by Walcher *et al.* to be $v_{\mathrm{min}} = 13\,\mathrm{km/s} \leq v_{\mathrm{disp}} \leq v_{\mathrm{max}} = 34\,\mathrm{km/s}$ [25]. This assumption can be used to restrict the mass of Globular Clusters to a possible mass range but it fails to give an exact mass. Therefore a second assumption has to be made and the idea that a single Globular Cluster is associated with a specific mass is abandoned. Instead a Globular Cluster is thought to contribute with its probability function, that is specified by its number distribution $n_{\mathrm{GC}}(M)$, to the probability that a cluster of the Globular Cluster system has a certain mass. This leads to another problem because it is not apparent which distribution has to be chosen. For this reason the rest of this chapter discusses the two most straightforward and promising distributions in detail. One of them is the Gaussian distribution which is commonly

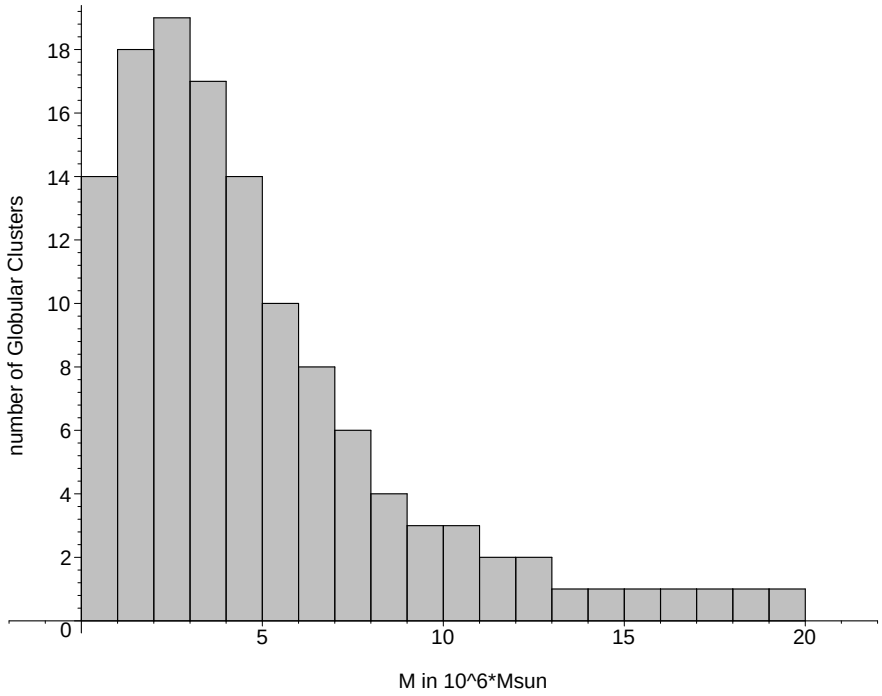

Figure 5.2: Number distribution for the Globular Cluster system in our Galaxy. The histogram plot displays the number of Globular Clusters in our Galaxy that can be expected to be in a certain mass range in units of $10^6\,M_\odot$. Each bin represents the expected number of Globular Clusters within its range $M_{\min} \leq M_{\rm GC} < M_{\max}$.

used to describe physical data

$$n_{\rm gauss}(M) \propto \exp\left(-\frac{(M - M_{\rm avg})^2}{2\sigma_{\rm M}}\right). \tag{5.2}$$

The other distribution of interest is a power law distribution that was found by numerical simulations of Globular Cluster systems

$$n_{\rm power}(M) \propto \begin{cases} \left(\frac{M}{M_\odot}\right)^{-1.9} & \text{for } M_{\rm MIN} \leq M \leq M_{\rm MAX}, \\ 0 & \text{otherwise.} \end{cases} \tag{5.3}$$

where $M_{\rm MIN}$ and $M_{\rm MAX}$ are the upper and lower cutoff masses for the power law distribution. Together with equation (5.1) the measured range of velocity dispersions for NCs can be used to calculate the average mass $M_{\rm avg}$ and mass dispersion σ_M for the Gaussian distribution, as well as the minimum $M_{\rm MIN}$ and maximum $M_{\rm MAX}$ Globular Cluster mass for the power law distribution for every Globular Cluster in the Globular Cluster system of our Galaxy.

Both number distributions depend on the cluster mass while the parameter of interest for the decay and annihilation flux is the core density of a cluster. Therefore it is necessary to a find a connection between mass and core density. If the core radii, scale radii, tidal radii, and averaged inner power law indices of the Globular Clusters are known a simple relation is implied by the dark matter profile. Besides this straightforward approach another relation can be found that is independent of the cluster radii and depends solely on the visual magnitude of the Globular Clusters and an empirical relation between the mass to light ratio (M/L-ratio) and the density. On first glance it seems needless to calculate the core density twice but it presents an independent way to verify whether the results are reasonable or not.

5.1 Gaussian Mass Distribution

The first distribution to be considered is the Gaussian mass distribution. It makes the assumption that the most likely mass of a Globular Cluster in the Globular Cluster system is close to the average mass and that the probability for masses farther away from this average mass decreases. This probability that a Globular Cluster has a certain mass can be calculated by normalising (5.2) to unity

$$n_{\mathrm{gauss}}(M) = \frac{\exp\left(-\frac{(M-M_{\mathrm{avg}})^2}{2\sigma_{\mathrm{M}}}\right)}{\int_0^\infty \mathrm{d}M \, \exp\left(-\frac{(M-M_{\mathrm{avg}})^2}{2\sigma_{\mathrm{M}}}\right)}. \tag{5.4}$$

The resulting number distribution is similar for all GCs because the maximum and minimum values for the velocity dispersion are assumed to be identical. Slight variations of the average mass and the mass dispersion in the equations for the Globular Clusters arise solely from the cluster specific half mass radius which enters into equation (5.1). Therefore it is sufficient to display the number density for one GC as example for all Globular Clusters of the GC system. The normalised Gaussian number density over the mass is shown in Figure 5.1 for the first GC of the Harris catalogue. It turns out that for this Globular Cluster the number density has a maximum at about $5 \cdot 10^6 \, M_\odot$.

Up to this point only one specimen of the whole dataset was considered. To obtain a reasonable approximation on the number distribution of the Globular Cluster system with respect to the mass the individual number distributions for all 132 Globular Clusters with complete datasets have to be calculated and then to be sum-

marised

$$n_{\mathrm{GCsystem}}(M) = \sum_i n^{(i)}_{\mathrm{gauss}}(M). \tag{5.5}$$

This total number distribution for the GC system of our galaxy is displayed as a statistical histogram plot in Figure 5.2. It has a maximum at a GC mass of $(2-3)\cdot 10^6\, M_\odot$ and predicts a small number of Globular Cluster with masses in excess of $2\cdot 10^7\, M_\odot$ up to the order of $10^8\, M_\odot$. This intermediate result is in good agreement with the mass range for Globular Clusters given by [25, 28] and slightly bigger than those by [30, 31].

The final step in the calculation of the core densities is to find a relation between the cluster mass M and the core density ρ to derive the number distribution dependent on the core radius. As outlined in the previous section there are two independent approaches that will be discussed separately in the following subsections.

5.1.1 Core Density from Structure Parameter δ

If the inner power law index and all required radii of a GC are known the relation between the core density and the cluster mass can be written in a simple form that was introduced in equation (3.4)

$$M = \rho\delta, \tag{5.6}$$

where the structure parameter δ is the constant of proportionality between the mass M of a Globular Cluster and its core density ρ. The structure parameter is profile dependent and for the profile with variable inner power law index which was introduced and discussed in detail in Chapter 4 it depends on the core radius, the scale radius, the tidal radius and the inner power law index. All these parameters are given or were calculated and therefore equation (5.2) can be rewritten as a function of the core density

$$n_{\mathrm{gauss}}(\rho) \propto \exp\left(-\frac{(\rho\delta - M_{\mathrm{avg}})^2}{2\sigma_{\mathrm{M}}}\right). \tag{5.7}$$

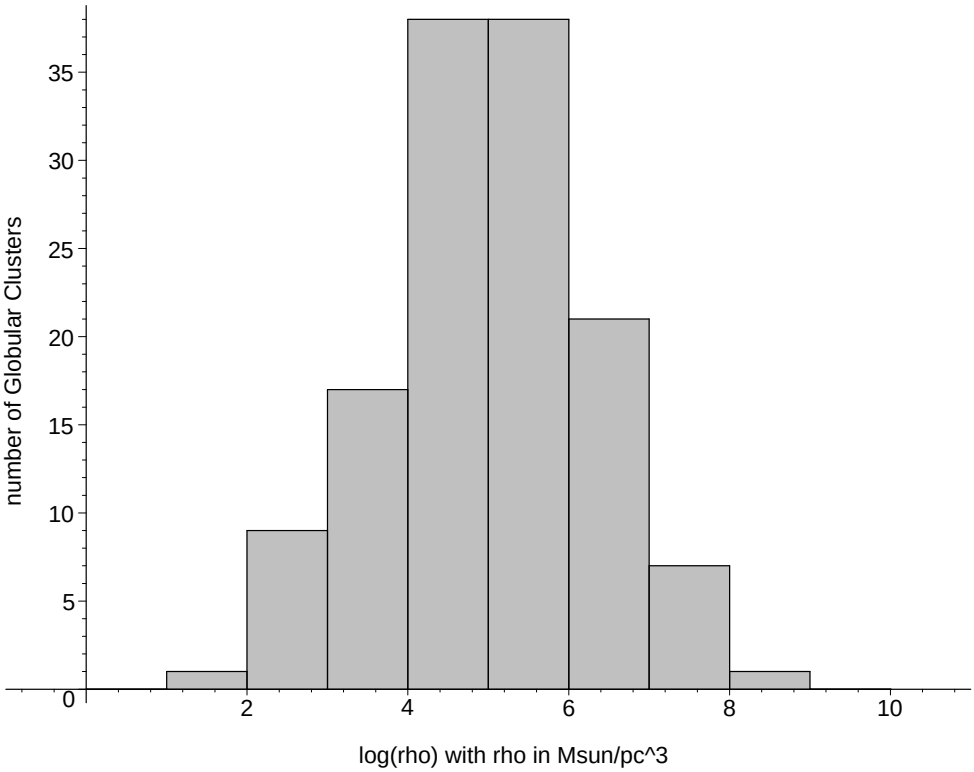

Figure 5.3: Number of Globular Clusters over the core density from structure parameter. The histogram plot displays the number of Globular Clusters over the common logarithm of the core density in units of $M_{\odot}\mathrm{pc}^{-3}$ as derived from the structure parameter δ. Each bin represents the expected number of Globular Clusters within its range $\rho_{\min} \leq \rho < \rho_{\max}$.

Similar to the number density over the mass it is necessary to normalise the number density with respect to the core density independently for each GC

$$n_{\mathrm{gauss}}(\rho) = \frac{\exp\left(-\frac{(\rho\delta - M_{\mathrm{avg}})^2}{2\sigma_{\mathrm{M}}}\right)}{\int_0^{\infty} \mathrm{d}\rho \, \exp\left(-\frac{(\rho\delta - M_{\mathrm{avg}})^2}{2\sigma_{\mathrm{M}}}\right)} \tag{5.8}$$

and then to summarise the results for the 132 contributions as defined in equation (5.5).

The resulting number distribution for the Globular Cluster system is displayed as a histogram plot in Figure 5.3. For convenience the number of Globular Clusters is plotted over the common logarithm of the core density. It can easily be determined that the core densities of the GCs range from $10^2\, M_{\odot}\mathrm{pc}^{-3}$ to $10^8\, M_{\odot}\mathrm{pc}^{-3}$ and that the distribution is centred around a maximum at a core density of about $10^5\, M_{\odot}\mathrm{pc}^{-3}$.

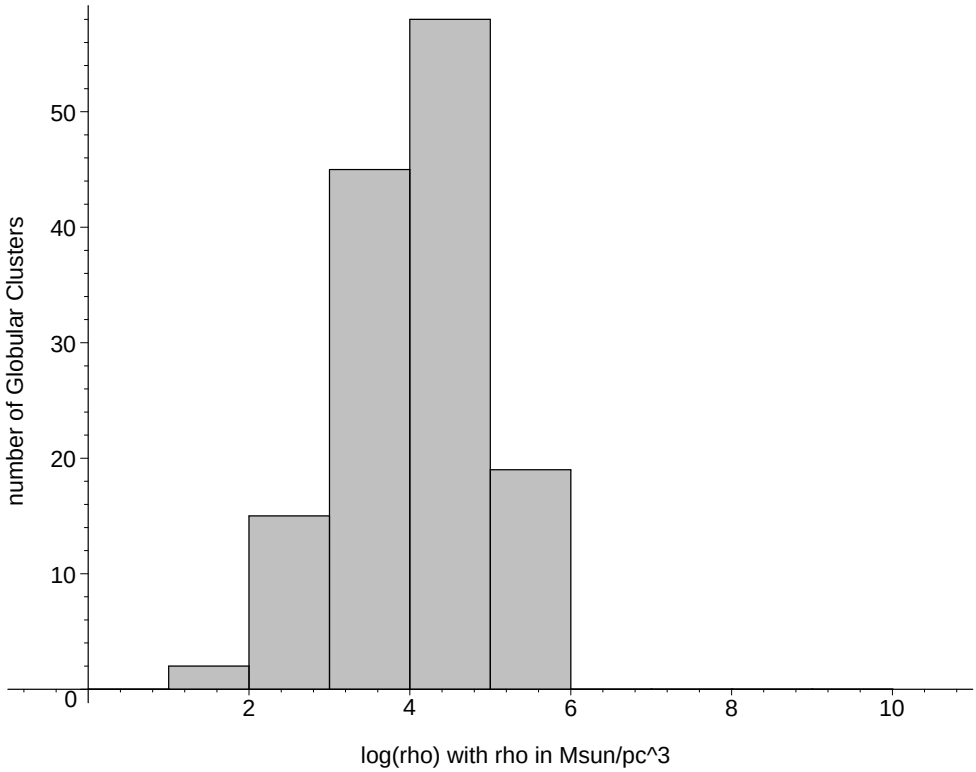

Figure 5.4: Number of Globular Clusters over the core density from M/L-ratio. The histogram plot displays the number of Globular Clusters over the common logarithm of the core density in units of $M_{\odot}\mathrm{pc}^{-3}$ as derived from the M/L-ratio. Each bin represents the expected number of Globular Clusters within its range $\rho_{\min} \leq \rho < \rho_{\max}$.

5.1.2 Core Density from M/L-ratio

Contrary to the derivation in the last subsection the calculation of the core density based on the M/L-ratio is completely independent of the shape of the DM profile. This is of special interest because all parameters needed for the calculation are included in the catalogue by Harris. The M/L-ratio is given by

$$\frac{M}{L} = M \cdot 10^{-\frac{V_{\odot}-V_{\mathrm{GC}}}{2.5}}, \tag{5.9}$$

where the luminosity is dependent on the absolute visual magnitude of the Sun $V_{\odot}$ as well as on the absolute visual magnitude of the Globular Cluster V_{GC} [30, 31]. A relation between the mass and the core density can now be derived by inserting the

M/L-ratio into the following empirical equation for the core density

$$\rho = \frac{3.44 \cdot 10^{10}}{Pr_h 10^{-0.4\sigma}} \frac{M}{L} = \frac{3.44 \cdot 10^{10} \cdot 10^{\frac{\sigma - V_\odot + V_{\mathrm{GC}}}{2.5}}}{Pr_h} M, \tag{5.10}$$

where $P \approx 2$ [6] and σ is the central visual surface brightness of the Globular Cluster. With this relation between the cluster mass and the core density equation (5.2) can be rewritten as

$$n_{\mathrm{gauss}}(\rho) \propto \exp\left(- \frac{\left(\frac{Pr_h}{3.44 \cdot 10^{10}} 10^{\frac{V_\odot - V_{\mathrm{GC}} - \sigma}{2.5}} \rho - M_{\mathrm{avg}} \right)^2}{2\sigma_{\mathrm{M}}} \right). \tag{5.11}$$

To obtain the number density with respect to the core density this distribution has again to be normalised to unity

$$n_{\mathrm{gauss}}(\rho) = \frac{\exp\left(- \frac{\left(\frac{Pr_h}{3.44 \cdot 10^{10}} 10^{\frac{V_\odot - V_{\mathrm{GC}} - \sigma}{2.5}} \rho - M_{\mathrm{avg}} \right)^2}{2\sigma_{\mathrm{M}}} \right)}{\int_0^\infty \mathrm{d}\rho \, \exp\left(- \frac{\left(\frac{Pr_h}{3.44 \cdot 10^{10}} 10^{\frac{V_\odot - V_{\mathrm{GC}} - \sigma}{2.5}} \rho - M_{\mathrm{avg}} \right)^2}{2\sigma_{\mathrm{M}}} \right)}. \tag{5.12}$$

Finally the contributions for the individual clusters in the Globular Cluster system have to be summarised according to equation (5.5).

Figure 5.4 shows the number distribution of the Globular Cluster system where the number density is displayed over the common logarithm of the core density. It turns out that most of the GCs have a core density of $10^2 \, M_\odot \mathrm{pc}^{-3} \leq \rho \leq 10^6 \, M_\odot \mathrm{pc}^{-3}$ and the maximum of the distribution is located at a core density of about $10^4 \, M_\odot \mathrm{pc}^{-3}$ to $10^5 \, M_\odot \mathrm{pc}^3$. In addition it seems that the number distribution has a steep cutoff at $10^6 \, M_\odot \mathrm{pc}^{-3}$.

5.2 Power Law Distribution

The second distribution of interest is a power law mass distribution that was found by numerical simulations of dark matter substructures. Therefore the number distribution should reflect this result and have a form as defined in equation (5.3). Otherwise the calculations for the power law distribution are completely analogous to the calculations for the Gaussian distribution outlined in the previous section.

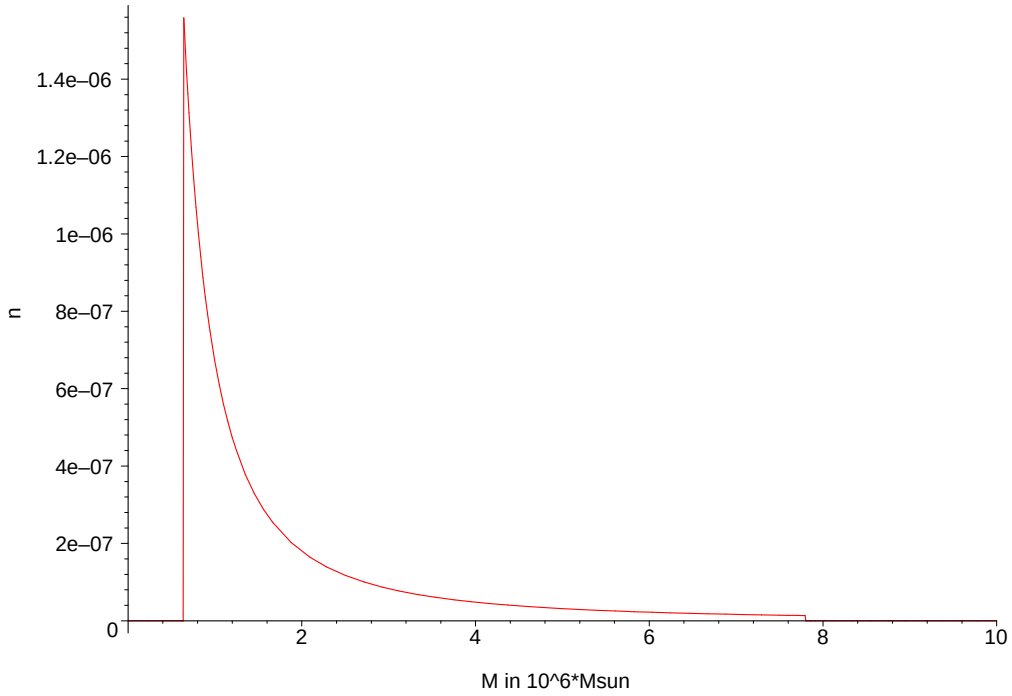

Figure 5.5: Normalised power law mass distribution. The graph shows the normalised power law mass distribution for the first Globular Cluster of the Harris catalogue. It represents the possibility of the Globular Cluster having a certain mass over the mass in units of $10^6\,M_\odot$.

Normalisation of the power law distribution to unity results in the following number distribution

$$n_{\text{power}}(M) = \begin{cases} \frac{M_{\text{MIN}}^{0.9} M_{\text{MAX}}^{0.9}}{0.9\left(M_{\text{MAX}}^{0.9} - M_{\text{MIN}}^{0.9}\right)} M^{-1.9} & \text{for } M_{\text{MIN}} \leq M \leq M_{\text{MAX}}, \\ 0 & \text{otherwise.} \end{cases} \tag{5.13}$$

For convenience the normalisation constant for the number distribution with respect to the cluster mass will be denoted as

$$\kappa = \frac{M_{\text{MIN}}^{0.9} M_{\text{MAX}}^{0.9}}{0.9\left(M_{\text{MAX}}^{0.9} - M_{\text{MIN}}^{0.9}\right)}. \tag{5.14}$$

Like before the number distributions for all Globular Clusters of the system look alike and differ only slightly because of the influence of the cluster specific half mass radius that has an influence on the minimum and maximum mass of the cluster. The normalised power law distribution of the first Globular Cluster in the Harris catalogue is displayed in Figure 5.5. As expected the power law distribution with respect to the cluster mass differs significantly from the Gaussian distribution of the previous

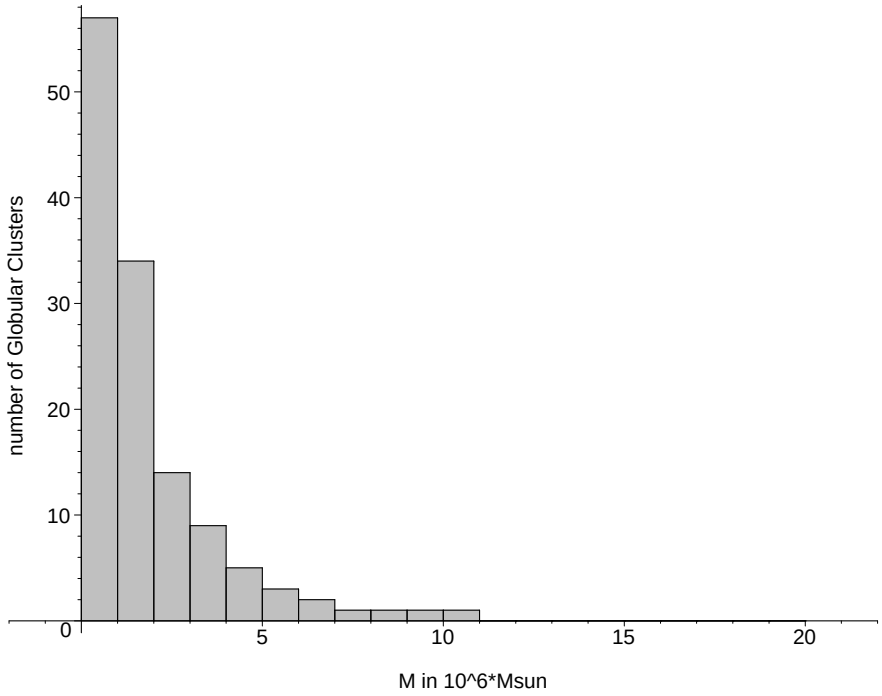

Figure 5.6: Number distribution for the Globular Cluster system in our Galaxy. The histogram plot displays the number of Globular Clusters in our Galaxy that can be expected to be in a certain mass range in units of $10^6\,M_\odot$. Each bin represents the expected number of Globular Clusters within its range $M_{\min} \leq M_{\mathrm{GC}} < M_{\max}$.

section. It has a maximum at a Globular Cluster mass of $M = M_{\mathrm{MIN}} \approx 6 \cdot 10^5\,M_\odot$ and drops off according to the power law up to the maximum mass.

To obtain the number distribution for the globular cluster system the number distributions for all 132 Globular Clusters have to be calculated and summarised

$$n_{\mathrm{GCsystem}}(M) = \sum_i n^{(i)}_{\mathrm{power}}(M). \tag{5.15}$$

The number distribution of the Globular Cluster system with respect to the mass is then shown in form of a histogram plot in Figure 5.6. As expected from a sum of power law distributions the number distribution of the Globular Cluster system favours systems with masses close to the lower end of the mass distribution and exhibits a maximum for Globular Clusters with $M < 10^6\,M_\odot$. Even though this peak seems to appear at a very low mass it has to be pointed out that due to the steep lower cutoff at $M = M_{\mathrm{MIN}}$ there are no Globular Clusters expected with masses smaller than $10^5\,M_\odot$. The graph also indicates that the probability for clusters heavier than a maximum mass of $1.1 \cdot 10^7\,M_\odot$ is very small. An absolute upper cutoff mass can be

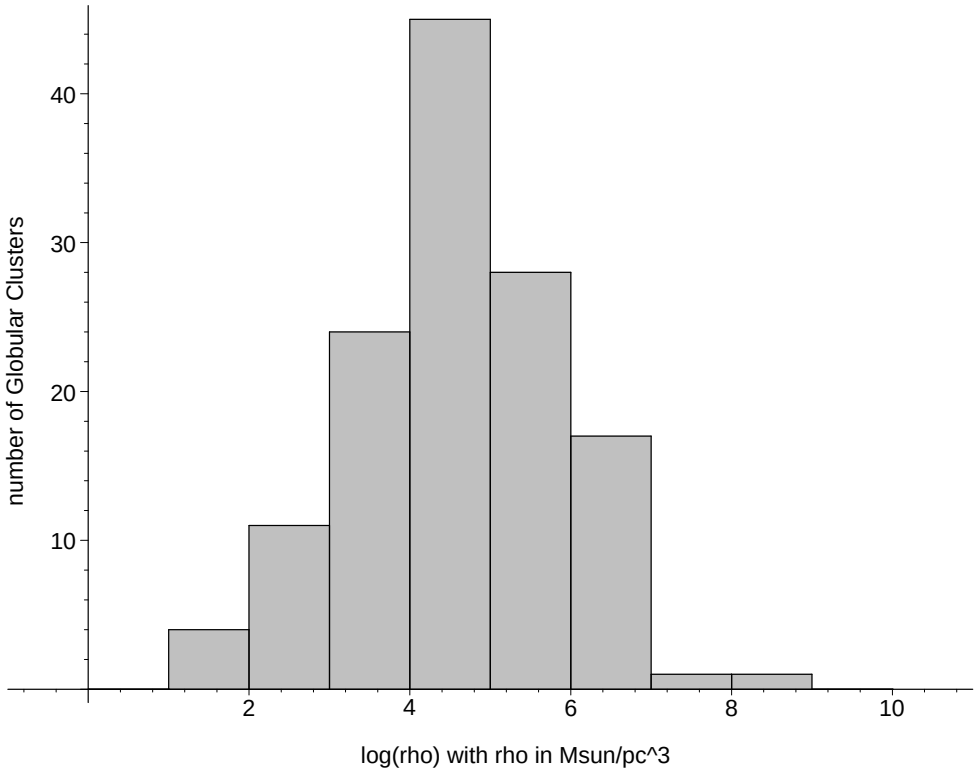

Figure 5.7: Number of Globular Clusters over the core density from structure parameter. The histogram plot displays the number of Globular Clusters over the common logarithm of the core density in units of $M_{\odot}\mathrm{pc}^{-3}$ as derived from the structure parameter δ. Each bin represents the expected number of Globular Clusters within its range $\rho_{\min} \leq \rho < \rho_{\max}$.

derived by finding the biggest maximum mass for a cluster in the GC system. Per definition the probability to find a cluster with mass exceeding this absolute cutoff is zero. The determined mass range for the clusters in the Globular Cluster system is in perfect agreement with the predictions of all authors considered in the previous section because most of the clusters have masses of the order of $10^6\,M_{\odot}$ while there are only a few clusters with masses of about one order of magnitude heavier. But even those clusters fall well into the extended mass range of $10^4\,M_{\odot} \leq M \leq 10^8\,M_{\odot}$.

5.2.1 Core Density from Structure Parameter δ

The first way to find a density dependent number distribution is the previously introduced relation (5.6) that arises directly from the dark matter profile if all needed radii and the inner power law indices are known. This relation between the mass and the core density can be inserted into equation (5.13) to derive the number distribution

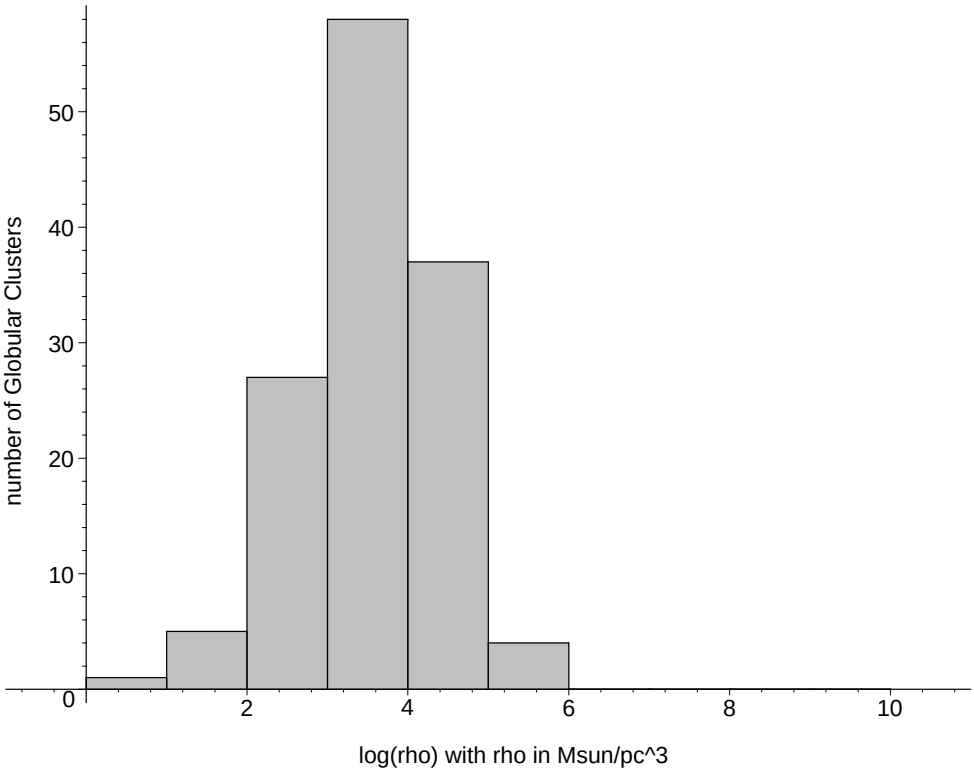

Figure 5.8: Number of Globular Clusters over the core density from M/L-ratio. The histogram plot displays the number of Globular Clusters over the common logarithm of the core density in units of $M_\odot \mathrm{pc}^{-3}$ as derived from the M/L-ratio. Each bin represents the expected number of Globular Clusters within its range $\rho_{\min} \leq \rho < \rho_{\max}$.

with respect to the core density

$$n_{\mathrm{power}}(\rho) = \begin{cases} \frac{\kappa}{\delta^{0.9}} \rho^{-1.9} & \text{for } \rho_{\mathrm{MIN}} \leq \rho \leq \rho_{\mathrm{MAX}}, \\ 0 & \text{otherwise.} \end{cases} \tag{5.16}$$

After calculating the number distributions for all Globular Clusters separately equation (5.15) is used to derive the number distribution for the Globular Cluster system.

The result of the summation is displayed as a histogram plot in Figure 5.7. It shows that the core densities for the power law index are between $10^1\, M_\odot \mathrm{pc}^{-3} \leq \rho \leq 10^7\, M_\odot \mathrm{pc}^{-3}$ with a maximum between $10^4\, M_\odot \mathrm{pc}^{-3}$ and $10^5\, M_\odot \mathrm{pc}^{-3}$. Furthermore a high density tail is present with core densities up to $10^9\, M_\odot \mathrm{pc}^{-3}$.

5.2.2 Core Density from M/L-ratio

In analogy to the previously discussed Gaussian distribution the second relation between the cluster mass and the core density will be analysed for the power law distribution as well. This relation was derived in the last section in equation (5.10) and is dependent on the absolute visual magnitude of the Globular Clusters. It can now be used to replace the mass dependence on the number distribution in equation (5.13) with a dependence on the core density

$$n_{\text{power}}(\rho) = \begin{cases} \frac{\kappa}{\left(\frac{Pr_h}{3.44 \cdot 10^{10}} 10^{\frac{V_\odot - V_{\text{GC}} - \sigma}{2.5}}\right)^{0.9}} \rho^{-1.9} & \text{for } \rho_{\text{MIN}} \leq \rho \leq \rho_{\text{MAX}}, \\ 0 & \text{otherwise.} \end{cases} \tag{5.17}$$

By adding the results for all Globular Clusters according to equation (5.15) it is possible to derive the number distribution for the Globular Cluster system.

Figure 5.8 shows this result in form of a histogram plot. For convenience the number distribution is plotted over the common logarithm of the core density. The graph clearly shows that the Globular Clusters have a core densities of $10^1\, M_\odot \text{pc}^{-3} \leq \rho < 10^6\, M_\odot \text{pc}^{-3}$ while the maximum of the distribution is located at at a core density of $10^3\, M_\odot \text{pc}^{-3}$ to $10^4\, M_\odot \text{pc}^{-3}$.

5.3 Conclusion

The calculation of explicit core densities for the Globular Clusters in our Galaxy is up to now impossible because the mass of a Globular Cluster is not directly accessible to measurements. Therefore it is necessary to make two assumptions which were outlined at the beginning of this chapter to circumvent this problems.
Within the scope of this thesis calculations for the two most likely Globular Cluster mass distributions were performed to minimise systematic errors. In addition to this case separation for the mass distributions two independent relations between the cluster mass and the core density were discussed for each distribution. This makes it possible to verify whether the core density derived from different Globular Cluster properties, on the one hand the cluster radii in combination with the inner power law index and on the other hand the absolute visual magnitude, yield similar results.

The results for the different scenarios are displayed in Figures 5.3, 5.4, 5.7, and 5.8. It turns out that the profiles for all cases look very similar although there are minor differences that have to be mentioned. The maximum of the number distribu-

tion for the Globular Cluster system occurs at about $10^5\,M_\odot\mathrm{pc}^{-3}$ for the Gaussian distribution in combination with the structure parameter δ. For the calculations for the Gaussian distribution in combination with the M/L-ratio and for the power law distribution with the structure parameter δ this maximum is located about half an order of magnitude lower and occurs at a Globular Cluster mass of $10^4\,M_\odot\mathrm{pc}^{-3}$ to $10^5\,M_\odot\mathrm{pc}^{-3}$. The case that shows the maximum of the number distribution at the lowest mass is the power law distribution together with the M/L-ratio at a mass of $10^3\,M_\odot\mathrm{pc}^{-3}$ to $10^4\,M_\odot\mathrm{pc}^{-3}$. Furthermore it appears that the heaviest GCs are suppressed or eliminated in the calculations for the M/L-ratio because Figures 5.4 and 5.8 show a sharp dropoff at $10^6\,M_\odot$ and $10^5\,M_\odot$ respectively.

Although the final results indicate a systematic difference between the results for the Gaussian distribution and the power law distribution by about half an order of magnitude it is interesting that the overall shape of the number distribution of the Globular Cluster system seems to be independent of the initial profile assumption. In addition to the offset between the distributions there is another systematic difference of about one order of magnitude between the calculations with respect to the structure parameter δ and the M/L-ratio.

The second offset might be in connection with the previously mentioned sharp dropoff for the calculations with respect to the M/L-ratio. It is presumed to be caused by the underestimation of the visual magnitude and the surface brightness. Both measurements are limited by the ability to distinguish total and radial differences in the brightness due to smearing in the central region [30]. These results can therefore be considered as a conservative lower limit.

Despite the differences between the cases all but the power law index with the M/L-ratio are in good agreement with the core densities of GCs of $10^4\,M_\odot\mathrm{pc}^{-3}$ to $5\cdot10^5\,M_\odot\mathrm{pc}^{-3}$ calculated by [30, 31]. The high core density tail $\rho_0 \geq 10^6\,M_\odot\mathrm{pc}^{-3}$ of the Globular Cluster number distribution for the structure parameter calculation gives much higher core densities for some of the GCs than previously expected. This is of special interest for the calculation of the UHECR flux from SHDM in Globular Cluster-like substructures because higher core densities would yield significantly increased annihilation rates that might be within the resolution limits of future detector systems like the Pierre Auger Observatory.

Chapter 6

Final Results

The objective of this thesis is to calculate the UHECR flux from SHDM annihilation in Globular Cluster-like substructures. To achieve this goal the annihilation flux was calculated for the NFW-profile and the Moore-profile. In addition a new constant density core approach was introduced that presents an interesting order of magnitude approximation if SHDM substructures exhibit flat cores that dominate the total flux. The first simulation results proved to be promising because it was possible to show that the fraction of the clumped SHDM ξ and the fraction of the heaviest substructure are not independent of each other. Moreover it was shown that the number of subclumps is linearly dependent on the ratio ξ/η. This relation is of special interest because simulations with a ratio of $50 \leq \xi/\eta \leq 100$ were able to reproduce an amount of substructure similar to the Globular Cluster system of our Galaxy. Choosing the boundary conditions to be $\xi = 10^{-1}$ and $\eta = 10^{-3}$, which is equivalent to a ratio of $\xi/\eta = 100$, implies a maximum mass for a subclump in the system of $10^9\, M_\odot$ based on a halo mass of $10^{12}\, M_\odot$. This is about one order of magnitude bigger than the intermediate results for the upper cutoff mass of the Globular Cluster system in our Galaxy. Furthermore the product of the fraction of the s-wave unitary bound ζ and the fraction of the density of the Sun ν is of the order of $-4.5 \leq \log_{10}(\zeta\nu) \leq -3.5$ throughout the previously stated range of interest for the ratio ξ/η.

The next step was to find possible similarities between the theoretically derived parameters for SHDM substructures and measured parameters of the Globular Cluster system in our Galaxy given by Harris. Initially it was intended to show which of the most prominent dark matter profiles fits the data best and then to use this profile for the rest of the analysis. Instead detailed analysis proved that none of the most commonly used dark matter profiles was able to explain the data. This

outcome motivated the use of a general dark matter profile similar to the NFW- and the Moore-profile which uses a variable inner power law index. It was possible to fit nearly all Globular Clusters with complete datasets from the catalogue by Harris to this general profile. The averaged inner power law index turned out to be $\alpha = 4$ which is significantly steeper than all previously considered dark matter profiles.

Finally the core densities of the Globular Clusters were derived by abandoning the idea to associate a Globular Cluster with an explicit mass. Instead a Globular Cluster contributes with its number distribution to the probability that a Globular Cluster of the system has a certain mass. The calculations were performed for two distributions, the Gaussian distribution and a power law distribution, as well as for two different relations between the cluster mass and the core density. This minimises the possibility of systematic errors and offers a chance to verify the results. Thus the core densities were found to be of the order of $10^2 M_\odot\,\mathrm{pc}^{-3}$ to $10^8 M_\odot\,\mathrm{pc}^{-3}$ which is in good agreement with previous results by other authors.

Based on the work done in connection with this thesis it can be concluded that SHDM annihilation from Globular Cluster-like substructures presents a good possibility to explain the measured UHECR flux. This would combine the two previously unrelated phenomena in present day astroparticle physics.

Appendix A

Greisen-Zatsepin-Kuzmin Cutoff

The derivation of the GZK-cutoff can be simplified by calculating in the center of mass frame of the CMB-photon. In this frame the total momentum is always zero and the equations for the conservation of momentum can be written down separately.

$$\vec{\mathbf{p}}_\gamma + \vec{\mathbf{p}}_p = 0 \quad \text{and} \quad \vec{\mathbf{p}}_n + \vec{\mathbf{p}}_{\pi^+} = 0 \tag{A.1}$$

At the threshold energy where a neutron and a pion at rest are generated the second equation is trivially fulfilled and only the first equation is of interest.

$$\vec{\mathbf{p}}_p = -\vec{\mathbf{p}}_\gamma \tag{A.2}$$

Calculation of the cutoff energy from the conservation of the four momentum in a particle interaction.

$$(p_\gamma + p_p)^\alpha (p_\gamma + p_p)_\alpha = (p_n + p_{\pi^+})^\alpha (p_n + p_{\pi^+})_\alpha \tag{A.3}$$

Independent calculation of both sides of equation (A.3) by assuming that $E_p \approx \left|\vec{\mathbf{p}}_p\right|$ for $E_p \gg m_p$.

$$\begin{aligned}
\text{(lhs)} : (p_\gamma + p_p)^\alpha (p_\gamma + p_p)_\alpha &= {p_\gamma}^\alpha p_{\gamma\alpha} + 2{p_\gamma}^\alpha p_{p\alpha} + {p_p}^\alpha p_{p\alpha} \\
\text{with } {p_\gamma}^\alpha p_{\gamma\alpha} &= -E_\gamma^2 + \vec{\mathbf{p}}_\gamma^2 \\
&= -\vec{\mathbf{p}}_\gamma^2 + \vec{\mathbf{p}}_\gamma^2 = 0 \\
{p_p}^\alpha p_{p\alpha} &= -E_p^2 + \vec{\mathbf{p}}_p^2 \\
&= -\left(\vec{\mathbf{p}}_p^2 + m_p^2\right) + \vec{\mathbf{p}}_p^2 = -m_p^2 \\
&= 2{p_\gamma}^\alpha p_{p\alpha} - m_p^2 \\
\text{with } {p_\gamma}^\alpha p_{p\alpha} &= -E_\gamma E_p - \vec{\mathbf{p}}_\gamma \vec{\mathbf{p}}_p \\
&= -E_\gamma E_p - E_\gamma E_p \\
&= -2E_\gamma E_p \\
&= -4E_\gamma E_p - m_p^2
\end{aligned} \tag{A.4}$$

$$
\begin{aligned}
\text{(rhs)} : \left(p_n + p_{\pi^+}\right)^\alpha \left(p_n + p_{\pi^+}\right)_\alpha &= \left(E_n + E_{\pi^+}, \vec{0} + \vec{0}\right)^2 \\
&= -\left(E_n + E_{\pi^+}\right)^2 \\
&\quad \text{with } E_x = m_x \text{ for particle at rest} \\
&= -\left(m_n + m_{\pi^+}\right)^2
\end{aligned}
\tag{A.5}
$$

Derivation of the equation for the cutoff energy by plugging the results from equation (A.5) and equation (A.6) into equation (A.3) for the conservation of the four momentum and solving the resulting equation for the proton energy.

$$
\begin{aligned}
\left(p_\gamma + p_p\right)^\alpha \left(p_\gamma + p_p\right)_\alpha &= \left(p_n + p_{\pi^+}\right)^\alpha \left(p_n + p_{\pi^+}\right)_\alpha \\
\Rightarrow -4E_p E_\gamma - m_p^2 &= -m_p^2 - 2m_n m_{\pi^+} - m_{\pi^+}^2 \\
&\quad \text{with } m_p \approx m_n \\
&= -m_p^2 - 2m_p m_{\pi^+} - m_{\pi^+}^2 \\
\Rightarrow -4E_p E_\gamma &= -2m_p m_{\pi^+} - m_{\pi^+}^2 \\
\Rightarrow E_p &= \frac{1}{4E_\gamma}\left(2m_p m_{\pi^+} + m_{\pi^+}^2\right) \\
&= \frac{m_p m_{\pi^+}}{2E_\gamma}\left(1 + \frac{m_{\pi^+}}{2m_p}\right)
\end{aligned}
\tag{A.6}
$$

Calculation of a numerical value for the cutoff energy with the proton mass $m_p = 938.3\,\text{MeV}$, the pion mass $m_{\pi^+} = 139\,\text{MeV}$, and the energy of the CMB-photons $E_\gamma = 2 \cdot 10^{-4}\,\text{eV}$.

$$
\begin{aligned}
E_p &= \frac{938.3\,\text{MeV} \cdot 139\,\text{MeV}}{2 \cdot 2 \cdot 10^{-4}\,\text{eV}}\left(1 + \frac{139\,\text{MeV}}{2 \cdot 938.3\,\text{MeV}}\right) \\
&\approx 3.5 \cdot 10^{20}\,\text{eV}
\end{aligned}
\tag{A.7}
$$

Appendix B

Navarro, Frenk, and White-Profile

1. The normalisation constant for the density profile can be calculated by integrating the density profile over the volume of the dark matter halo and solving the resulting equation for the normalisation constant.

$$
\begin{aligned}
M_H &= \int d^3\vec{r}\,\rho_H(r) \\
&\quad \text{with } \rho_H(r) = \frac{N_0 M_X r_s^3}{r\,(r+r_s)^2} \\
&= \int d^3\vec{r}\,\frac{N_0 M_X r_s^3}{r\,(r+r_s)^2} \\
&= 4\pi N_0 M_X r_s^3 \int_0^{r_t} \mathrm{d}r\,\frac{r}{(r+r_s)^2} \\
&= 4\pi N_0 M_X r_s^3 \int_0^{r_t} \mathrm{d}r\,\left(\frac{1}{(r+r_s)} - \frac{r_s}{(r+r_s)^2}\right) \\
&= 4\pi N_0 M_X r_s^3 \left(\ln\frac{r_t+r_s}{r_s} - \frac{r_t}{r_t+r_s}\right) \\
\Rightarrow N_0 &= \frac{M_H}{4\pi M_X r_s^3 \left(\ln\frac{r_t+r_s}{r_s} - \frac{r_t}{r_t+r_s}\right)}
\end{aligned}
\tag{B.1}
$$

For $r_t \gg r_s$ this exact result can be slightly simplified. This approximation does not eliminate any of the parameters and only slightly decreases the computational complexity.

$$
\begin{aligned}
N_0 &= \frac{M_H}{4\pi M_X r_s^3 \left(\ln\frac{r_t+r_s}{r_s} - \frac{r_t}{r_t+r_s}\right)} \\
&\quad \text{with } \ln\frac{r_t+r_s}{r_s} - \frac{r_t}{r_t+r_s} \approx \ln\frac{r_t}{r_s} - 1 \\
&\approx \frac{M_H}{4\pi M_X r_s^3 \left(\ln\frac{r_t}{r_s} - 1\right)}
\end{aligned}
\tag{B.2}
$$

2. An exact solution for the decay flux from the smooth DM component can now be derived by solving the spatial integral over the normalised number density in the following equation.

$$
\begin{aligned}
\mathcal{F} &= 2\frac{\mathrm{d}N}{\mathrm{d}E}\Gamma_X \int \mathrm{d}^3\vec{r}\,\frac{n_H\left(r\right)}{4\pi\left|\vec{r}-\vec{r}_\odot\right|^2} \\
&\quad \text{with} \qquad n_H(r) = \frac{N_0 r_s^3}{r\left(r+r_s\right)^2} \\
&\qquad\qquad \frac{1}{\left|\vec{r}-\vec{r}_\odot\right|^2} = \frac{1}{r^2+r_\odot^2-2rr_\odot\cos\theta} \\
&= 2\frac{\mathrm{d}N}{\mathrm{d}E}\Gamma_X \int \mathrm{d}^3\vec{r}\,\frac{N_0 r_s^3}{r\left(r+r_s\right)^2}\frac{1}{4\pi\left(r^2+r_\odot^2-2rr_\odot\cos\theta\right)} \\
&= \frac{\mathrm{d}N}{\mathrm{d}E}\Gamma_X N_0 r_s^3 \int_0^{r_t}\mathrm{d}r\int_0^{\pi}\mathrm{d}\theta\,\frac{r\sin\theta}{\left(r+r_s\right)^2\left(r^2+r_\odot^2-2rr_\odot\cos\theta\right)} \\
&= \frac{\mathrm{d}N}{\mathrm{d}E}\Gamma_X N_0 r_s^3 \int_0^{r_t}\mathrm{d}r\int_{-1}^{1}\mathrm{d}x\,\frac{r}{\left(r+r_s\right)^2\left(r^2+r_\odot^2-2rr_\odot x\right)} \\
&\quad \text{with} \int_{-1}^{1}\mathrm{d}x\,\frac{1}{r^2+r_\odot^2-2rr_\odot x} = \frac{1}{rr_\odot}\ln\frac{r+r_\odot}{\left|r-r_\odot\right|} \\
&= \frac{\mathrm{d}N}{\mathrm{d}E}\Gamma_X N_0 \frac{r_s^3}{r_\odot}\int_0^{r_t}\mathrm{d}r\,\frac{1}{\left(r+r_s\right)^2}\ln\frac{r+r_\odot}{\left|r-r_\odot\right|} \qquad \text{(B.3)} \\
&= \frac{\mathrm{d}N}{\mathrm{d}E}\Gamma_X N_0 \frac{r_s^3}{r_\odot}\left\{\int_0^{r_t}\mathrm{d}r\,\frac{\ln\left(r+r_\odot\right)}{\left(r+r_s\right)^2} - \int_0^{r_\odot}\mathrm{d}r\,\frac{\ln\left(r_\odot-r\right)}{\left(r+r_s\right)^2} - \int_{r_\odot}^{r_t}\mathrm{d}r\,\frac{\ln\left(r-r_\odot\right)}{\left(r+r_s\right)^2}\right\} \\
&\quad \text{with} \int_0^{r_t}\mathrm{d}r\,\frac{\ln\left(r+r_\odot\right)}{\left(r+r_s\right)^2} = \frac{\ln r_\odot}{r_s} - \frac{\ln\left(r_t+r_\odot\right)}{r_t+r_s} + \frac{1}{r_s-r_\odot}\ln\frac{r_s\left(r_t+r_\odot\right)}{r_\odot\left(r_t+r_s\right)} \\
&\qquad\qquad \int_0^{r_\odot}\mathrm{d}r\,\frac{\ln\left(r_\odot-r\right)}{\left(r+r_s\right)^2} = \frac{\ln r_s}{r_\odot+r_s} - \frac{\ln\left(r_\odot+r_s\right)}{r_\odot+r_s} + \frac{r_\odot\ln r_\odot}{r_s\left(r_\odot+r_s\right)} \\
&\qquad\qquad \int_{r_\odot}^{r_t}\mathrm{d}r\,\frac{\ln\left(r-r_\odot\right)}{\left(r+r_s\right)^2} = \frac{1}{r_s+r_\odot}\ln\frac{\left(r_t-r_\odot\right)\left(r_s+r_\odot\right)}{r_t+r_s} - \frac{\ln\left(r_t-r_\odot\right)}{r_t+r_s} \\
&= \frac{\mathrm{d}N}{\mathrm{d}E}\Gamma_X N_0 \frac{r_s^3}{r_\odot}\left\{\frac{\ln r_\odot}{r_s} - \frac{\ln\left(r_t+r_\odot\right)}{r_t+r_s} + \frac{1}{r_s-r_\odot}\ln\frac{r_s\left(r_t+r_\odot\right)}{r_\odot\left(r_t+r_s\right)} - \frac{\ln r_s}{r_\odot+r_s} + \frac{\ln\left(r_\odot+r_s\right)}{r_\odot+r_s}\right. \\
&\quad \left. - \frac{r_\odot\ln r_\odot}{r_s\left(r_\odot+r_s\right)} - \frac{1}{r_s+r_\odot}\ln\frac{\left(r_t-r_\odot\right)\left(r_s+r_\odot\right)}{r_t+r_s} + \frac{\ln\left(r_t-r_\odot\right)}{r_t+r_s}\right\} \\
&= \frac{\mathrm{d}N}{\mathrm{d}E}\Gamma_X N_0 \frac{r_s^3}{r_\odot}\left\{\frac{1}{r_t+r_s}\ln\frac{r_t-r_\odot}{r_t+r_\odot} + \frac{1}{r_s-r_\odot}\ln\frac{r_s\left(r_t+r_\odot\right)}{r_\odot\left(r_t+r_s\right)} + \frac{1}{r_s+r_\odot}\ln\frac{r_\odot\left(r_t+r_s\right)}{r_s\left(r_t-r_\odot\right)}\right\}
\end{aligned}
$$

From the physical point of view the contribution from dark matter beyond the tidal radius to the overall flux is negligible and therefore the solution of the integral can be simplified by integrating from zero to ∞.

$$
\begin{aligned}
\mathcal{F} &\approx \frac{\mathrm{d}N}{\mathrm{d}E}\Gamma_X N_0 \frac{r_s^3}{r_\odot}\left\{\int_0^\infty \mathrm{d}r\,\frac{\ln\left(r+r_\odot\right)}{\left(r+r_s\right)^2} - \int_0^{r_\odot} \mathrm{d}r\,\frac{\ln\left(r_\odot-r\right)}{\left(r+r_s\right)^2} - \int_{r_\odot}^\infty \mathrm{d}r\,\frac{\ln\left(r-r_\odot\right)}{\left(r+r_s\right)^2}\right\} \\
&\quad \text{with} \quad \int_0^\infty \mathrm{d}r\,\frac{\ln\left(r+r_\odot\right)}{\left(r+r_s\right)^2} = \frac{r_\odot \ln r_\odot - r_s \ln r_s}{r_s\left(r_\odot - r_s\right)} \\
&\qquad\quad \int_0^{r_\odot} \mathrm{d}r\,\frac{\ln\left(r_\odot-r\right)}{\left(r+r_s\right)^2} = \frac{r_s \ln r_s - r_s \ln\left(r_\odot+r_s\right) + r_\odot \ln r_\odot}{r_s\left(r_\odot+r_s\right)} \\
&\qquad\quad \int_{r_\odot}^\infty \mathrm{d}r\,\frac{\ln\left(r-r_\odot\right)}{\left(r+r_s\right)^2} = \frac{\ln\left(r_\odot+r_s\right)}{r_\odot+r_s} \\
&= \frac{\mathrm{d}N}{\mathrm{d}E}\Gamma_X N_0 \frac{r_s^3}{r_\odot}\left\{\frac{r_\odot \ln r_\odot - r_s \ln r_s}{r_s\left(r_\odot - r_s\right)} - \frac{r_s \ln r_s - r_s \ln\left(r_\odot+r_s\right) + r_\odot \ln r_\odot}{r_s\left(r_\odot+r_s\right)} - \frac{\ln\left(r_\odot+r_s\right)}{r_\odot+r_s}\right\} \\
&= 2\frac{\mathrm{d}N}{\mathrm{d}E}\Gamma_X N_0 \frac{r_s^3}{r_s^2 - r_\odot^2}\ln\frac{r_s}{r_\odot}
\end{aligned}
\tag{B.4}
$$

The same result arises if the exact result is approximated by assuming that $r_t \gg r_\odot, r_s$.

3. The annihilation flux from the smooth DM component is calculated similar to the decay flux by integration of the square of the number density over the volume of the halo.

$$
\begin{aligned}
\mathcal{F} &= 2\frac{\mathrm{d}N}{\mathrm{d}E}\langle\sigma v\rangle \int \mathrm{d}^3\vec{r}\,\frac{n_H^2(r)}{4\pi\left|\vec{r}-\vec{r}_\odot\right|^2} \\
&\quad \text{with} \quad n_H(r) = \frac{N_0 r_s^3}{r\left(r+r_s\right)^2} \\
&\qquad\quad \frac{1}{\left|\vec{r}-\vec{r}_\odot\right|^2} = \frac{1}{r^2 + r_\odot^2 - 2rr_\odot\cos\theta} \\
&= 2\frac{\mathrm{d}N}{\mathrm{d}E}\langle\sigma v\rangle \int \mathrm{d}^3\vec{r}\,\frac{N_0^2 r_s^6}{r^2\left(r+r_s\right)^4}\frac{1}{4\pi\left(r^2+r_\odot^2-2rr_\odot\cos\theta\right)} \\
&= \frac{\mathrm{d}N}{\mathrm{d}E}\langle\sigma v\rangle N_0^2 r_s^6 \int_0^{r_t}\mathrm{d}r\int_0^\pi \mathrm{d}\theta\,\frac{\sin\theta}{\left(r+r_s\right)^4\left(r^2+r_\odot^2-2rr_\odot\cos\theta\right)} \\
&= \frac{\mathrm{d}N}{\mathrm{d}E}\langle\sigma v\rangle N_0^2 r_s^6 \int_0^{r_t}\mathrm{d}r\int_{-1}^1 \mathrm{d}x\,\frac{1}{\left(r+r_s\right)^4\left(r^2+r_\odot^2-2rr_\odot x\right)} \\
&\quad \text{with} \int_{-1}^1 \mathrm{d}x\,\frac{1}{r^2+r_\odot^2-2rr_\odot x} = \frac{1}{rr_\odot}\ln\frac{r+r_\odot}{\left|r-r_\odot\right|} \\
&= \frac{\mathrm{d}N}{\mathrm{d}E}\langle\sigma v\rangle N_0^2 \frac{r_s^6}{r_\odot}\int_0^{r_t}\mathrm{d}r\,\frac{1}{r\left(r+r_s\right)^4}\ln\frac{r+r_\odot}{\left|r-r_\odot\right|} \\
&\quad \text{with integral solution as defined in 3.1} \\
&= \frac{\mathrm{d}N}{\mathrm{d}E}\langle\sigma v\rangle N_0^2 \frac{r_s^2}{r_\odot}\left\{\frac{\pi^2}{3} - \ln\frac{r_s}{r_s-r_\odot}\ln\frac{r_s+r_\odot}{r_\odot} + \frac{1}{2}\ln^2\frac{r_s+r_\odot}{r_s-r_\odot} + L_2\left(\frac{r_s}{r_s-r_\odot}\right)\right. \\
&\quad \left. + L_2\left(\frac{r_\odot}{r_s+r_\odot}\right) - \frac{2r_\odot r_s\left(3r_\odot^4 - 8r_\odot^2 r_s^2 + 9r_s^4\right)}{3\left(r_s^2-r_\odot^2\right)^3}\ln\frac{r_s}{r_\odot} + \frac{4r_\odot r_s\left(2r_s^2-r_\odot^2\right)}{3\left(r_s^2-r_\odot^2\right)^2}\right\}
\end{aligned}
\tag{B.5}
$$

3.1 It is possible to solve the radial integral analytically. The calculation is extremely complex and has to be split up into five separate calculations to deal with the level

of complexity.

$$\begin{aligned}
\mathcal{I} &= \int_0^{r_t} \mathrm{d}r\, \frac{1}{r\,(r+r_s)^4} \ln\frac{r+r_\odot}{|r-r_\odot|} \qquad \text{(B.6)}\\
&\text{with } \frac{1}{r\,(r+r_s)^4} = \frac{1}{r_s^4 r} - \frac{1}{r_s^4\,(r+r_s)} - \frac{1}{r_s^3\,(r+r_s)^2} - \frac{1}{r_s^2\,(r+r_s)^3} - \frac{1}{r_s^1\,(r+r_s)^4}\\
&= \int^{r_t} \mathrm{d}r\, \ln\frac{r+r_\odot}{|r-r_\odot|} \left\{ \frac{1}{r_s^4 r} - \frac{1}{r_s^4\,(r+r_s)} - \frac{1}{r_s^3\,(r+r_s)^2} - \frac{1}{r_s^2\,(r+r_s)^3} - \frac{1}{r_s\,(r+r_s)^4} \right\}\\
&\approx \int_0^{\infty} \mathrm{d}r\, \ln\frac{r+r_\odot}{|r-r_\odot|} \left\{ \frac{1}{r_s^4 r} - \frac{1}{r_s^4\,(r+r_s)} - \frac{1}{r_s^3\,(r+r_s)^2} - \frac{1}{r_s^2\,(r+r_s)^3} - \frac{1}{r_s\,(r+r_s)^4} \right\}\\
&= \underbrace{\int_0^{\infty} \mathrm{d}r\, \frac{1}{r_s^4 r} \ln\frac{r+r_\odot}{|r-r_\odot|}}_{\text{(I)}} - \underbrace{\int_0^{\infty} \mathrm{d}r\, \frac{1}{r_s^4\,(r+r_s)} \ln\frac{r+r_\odot}{|r-r_\odot|}}_{\text{(II)}} - \underbrace{\int_0^{\infty} \mathrm{d}r\, \frac{1}{r_s^3\,(r+r_s)^2} \ln\frac{r+r_\odot}{|r-r_\odot|}}_{\text{(III)}}\\
&\quad - \underbrace{\int_0^{\infty} \mathrm{d}r\, \frac{1}{r_s^2\,(r+r_s)^3} \ln\frac{r+r_\odot}{|r-r_\odot|}}_{\text{(IV)}} - \underbrace{\int_0^{\infty} \mathrm{d}r\, \frac{1}{r_s\,(r+r_s)^4} \ln\frac{r+r_\odot}{|r-r_\odot|}}_{\text{(V)}}
\end{aligned}$$

For the rest of the derivation of the integral $\mathcal{I}$ lengthy repetitive calculations will not be explained in detail and only short descriptions are given which part is calculated. Calculation of the contribution from integral (I)

$$\begin{aligned}
\text{(I)} &= \int_0^{\infty} \mathrm{d}r \frac{1}{r_s^4 r} \ln\frac{r+r_\odot}{|r-r_\odot|} \qquad \text{(B.7)}\\
&= \frac{1}{r_s^4} \underbrace{\int_0^{\infty} \mathrm{d}r \frac{1}{r} \ln(r+r_\odot)}_{\text{(Ia)}} - \frac{1}{r_s^4} \underbrace{\int_0^{r_\odot} \mathrm{d}r \frac{1}{r} \ln(r_\odot - r)}_{\text{(Ib)}} - \frac{1}{r_s^4} \underbrace{\int_{r_\odot}^{\infty} \mathrm{d}r \frac{1}{r} \ln(r-r_\odot)}_{\text{(Ic)}}
\end{aligned}$$

Calculation of contribution (Ia) to integral (I)

$$\begin{aligned}
\text{(Ia)} &= \int_0^{\infty} \mathrm{d}r \frac{1}{r} \ln(r+r_\odot)\\
&= \int_0^{\infty} \mathrm{d}r \frac{1}{(r+r_\odot)-r_\odot} \ln(r+r_\odot)\\
&= \int_0^{\infty} \mathrm{d}r \frac{1}{r_\odot\left(\frac{r+r_\odot}{r_\odot}-1\right)} \ln(r+r_\odot)\\
&= -\int_0^{\infty} \mathrm{d}r \frac{1}{r_\odot\left(1-\frac{r+r_\odot}{r_\odot}\right)} \left\{ \ln\frac{r+r_\odot}{r_\odot} + \ln r_\odot \right\} \qquad \text{(B.8)}\\
&\quad \text{with } t = \frac{r+r_\odot}{r_\odot} \Rightarrow \frac{\mathrm{d}t}{\mathrm{d}r} = \frac{1}{r_\odot} \Rightarrow \mathrm{d}r = r_\odot \mathrm{d}t\\
&= -\int_1^{\infty} \mathrm{d}t \frac{1}{1-t} \ln t + \int_0^{\infty} \mathrm{d}r \frac{1}{r} \ln r_\odot\\
&= -L_2(t)|_{t=\infty} + \ln r \ln r_\odot|_0^{\infty}
\end{aligned}$$

Calculation of contribution (Ib) to integral (I)

$$
\begin{aligned}
(\mathrm{Ib}) &= \int_0^{r_\odot} \mathrm{d}r \frac{1}{r} \ln\left(r_\odot - r\right) \\
&= \ln r \ln\left(r_\odot - r\right)\big|_0^{r_\odot} - \int_0^{r_\odot} \mathrm{d}r \left(-\frac{1}{\left(r_\odot - r\right)}\right) \ln r \\
&= \ln r \ln\left(r_\odot - r\right)\big|_0^{r_\odot} + \int_0^{r_\odot} \mathrm{d}r \frac{1}{r_\odot - r} \ln r \\
&= \ln r \ln\left(r_\odot - r\right)\big|_0^{r_\odot} + \int_0^{r_\odot} \mathrm{d}r \frac{1}{r_\odot \left(1 - \frac{r}{r_\odot}\right)} \ln r \\
&= \ln r \ln\left(r_\odot - r\right)\big|_0^{r_\odot} + \int_0^{r_\odot} \mathrm{d}r \frac{1}{r_\odot \left(1 - \frac{r}{r_\odot}\right)} \left\{\ln \frac{r}{r_\odot} + \ln r_\odot\right\} \qquad \text{(B.9)} \\
&\quad \text{with } t = \frac{r}{r_\odot} \Rightarrow \frac{\mathrm{d}t}{\mathrm{d}r} = \frac{1}{r_\odot} \Rightarrow \mathrm{d}r = r_\odot \mathrm{d}t \\
&= \ln r \ln\left(r_\odot - r\right)\big|_0^{r_\odot} + \int_0^1 \mathrm{d}t \frac{1}{1-t} \ln t + \int_0^{r_\odot} \mathrm{d}r \frac{1}{r_\odot - r} \ln r_\odot \\
&= \ln r \ln\left(r_\odot - r\right)\big|_0^{r_\odot} - \int_1^0 \mathrm{d}t \frac{1}{1-t} \ln t + \int_0^{r_\odot} \mathrm{d}r \frac{1}{r_\odot - r} \ln r_\odot \\
&= \ln r \ln\left(r_\odot - r\right)\big|_0^{r_\odot} - L_2\left(t\right)\big|_{t=0} - \ln\left(r_\odot - r\right) \ln r_\odot\big|_0^{r_\odot} \\
&= \ln\left(r_\odot - r\right) \ln \frac{r}{r_\odot}\Bigg|_0^{r_\odot} - \frac{\pi^2}{6}
\end{aligned}
$$

Calculation of contribution (Ic) to integral (I)

$$
\begin{aligned}
(\mathrm{Ic}) &= \int_{r_\odot}^{\infty} \mathrm{d}r \frac{1}{r} \ln\left(r - r_\odot\right) \\
&= \ln r \ln\left(r - r_\odot\right)\big|_{r_\odot}^{\infty} - \int_{r_\odot}^{\infty} \mathrm{d}r \frac{1}{r - r_\odot} \ln r \\
&= \ln r \ln\left(r - r_\odot\right)\big|_{r_\odot}^{\infty} + \int_{r_\odot}^{\infty} \mathrm{d}r \frac{1}{r_\odot - r} \ln r \\
&= \ln r \ln\left(r - r_\odot\right)\big|_{r_\odot}^{\infty} + \int_{r_\odot}^{\infty} \mathrm{d}r \frac{1}{r_\odot \left(1 - \frac{r}{r_\odot}\right)} \ln r \\
&= \ln r \ln\left(r - r_\odot\right)\big|_{r_\odot}^{\infty} + \int_{r_\odot}^{\infty} \mathrm{d}r \frac{1}{r_\odot \left(1 - \frac{r}{r_\odot}\right)} \left\{\ln \frac{r}{r_\odot} + \ln r_\odot\right\} \qquad \text{(B.10)} \\
&\quad \text{with } t = \frac{r}{r_\odot} \Rightarrow \frac{\mathrm{d}t}{\mathrm{d}r} = \frac{1}{r_\odot} \Rightarrow \mathrm{d}r = r_\odot \mathrm{d}t \\
&= \ln r \ln\left(r - r_\odot\right)\big|_{r_\odot}^{\infty} + \int_1^{\infty} \mathrm{d}t \frac{1}{1-t} \ln t - \int_{r_\odot}^{\infty} \mathrm{d}r \frac{1}{r - r_\odot} \ln r_\odot \\
&= \ln r \ln\left(r - r_\odot\right)\big|_{r_\odot}^{\infty} + L_2\left(t\right)\big|_{t=\infty} - \ln\left(r - r_\odot\right) \ln r_\odot\big|_{r_\odot}^{\infty} \\
&= \ln\left(r - r_\odot\right) \ln \frac{r}{r_\odot}\Bigg|_{r_\odot}^{\infty} + L_2\left(t\right)\big|_{t=\infty}
\end{aligned}
$$

With the results from equations (Ia), (Ib), and (Ic) that were derived on the previous pages a solution for integral (I) is calculated.

$$
\begin{aligned}
(\mathrm{I}) = \frac{1}{r_s^4}\Bigg\{ & -L_2\left(\frac{r+r_\odot}{r_\odot}\right)\Big|_{r=\infty} + \ln r \ln r_\odot|_0^\infty - \ln r \ln\left(r_\odot - r\right)|_0^{r_\odot} + \frac{\pi^2}{6} \\
& + \ln\left(r_\odot - r\right)\ln r_\odot|_0^{r_\odot} - \ln r \ln\left(r - r_\odot\right)|_{r_\odot}^\infty - L_2\left(\frac{r}{r_\odot}\right)\Big|_{r=\infty} + \ln\left(r - r_\odot\right)\ln r_\odot|_{r_\odot}^\infty \Bigg\} \\
& \text{with } L_2\left(\frac{1}{x}\right) = -L_2(x) - \frac{1}{2}\ln^2(x) \quad \text{,for } 0 \le x \le 1 \\
= \frac{1}{r_s^4}\Bigg\{ & \frac{\pi^2}{6} + \frac{1}{2}\ln^2\frac{r_\odot}{r+r_\odot}\Big|_{r=\infty} + \ln r \ln r_\odot|_{r=\infty} - \ln r \ln r_\odot|_{r=0} - \ln r \ln\left(r_\odot - r\right)|_{r=r_\odot} \\
& + \ln r \ln\left(r_\odot - r\right)|_{r=0} + \frac{\pi^2}{6} + \ln\left(r_\odot - r\right)\ln r_\odot|_{r=r_\odot} - \ln^2 r_\odot - \ln r \ln\left(r - r_\odot\right)|_{r=\infty} \\
& + \ln r \ln\left(r - r_\odot\right)|_{r=r_\odot} + \frac{\pi^2}{6} + \frac{1}{2}\ln^2\frac{r_\odot}{r}\Big|_{r=\infty} + \ln\left(r - r_\odot\right)\ln r_\odot|_{r=\infty} \\
& - \ln\left(r - r_\odot\right)\ln r_\odot|_{r=r_\odot} \Bigg\} \\
= \frac{1}{r_s^4}\Bigg\{ & \frac{\pi^2}{2} + \frac{1}{2}\ln^2 r_\odot - \ln r_\odot \ln\left(r + r_\odot\right)|_{r=\infty} + \frac{1}{2}\ln^2\left(r + r_\odot\right)\Big|_{r=\infty} + \ln r \ln r_\odot|_{r=\infty} \\
& - \ln^2 r_\odot - \ln r \ln\left(r - r_\odot\right)|_{r=\infty} + \frac{1}{2}\ln^2 r_\odot - \ln r_\odot \ln r|_{r=\infty} + \frac{1}{2}\ln^2 r\Big|_{r=\infty} \\
& + \ln\left(r - r_\odot\right)\ln r_\odot|_{r=\infty} \Bigg\} \qquad \text{(B.11)} \\
= \frac{1}{r_s^4}\Bigg\{ & \frac{\pi^2}{2} - \ln r_\odot \ln r|_{r=\infty} - \ln r_\odot \ln\left(1 + \frac{r_\odot}{r}\right)\Big|_{r=\infty} + \frac{1}{2}\ln^2 r\Big|_{r=\infty} \\
& + \ln r \ln\left(1 + \frac{r_\odot}{r}\right)\Big|_{r=\infty} + \frac{1}{2}\ln^2\left(1 + \frac{r_\odot}{r}\right)\Big|_{r=\infty} + \ln r \ln r_\odot|_{r=\infty} - \ln^2 r|_{r=\infty} \\
& - \ln r \ln\left(1 - \frac{r_\odot}{r}\right)\Big|_{r=\infty} - \ln r_\odot \ln r|_{r=\infty} + \frac{1}{2}\ln^2 r\Big|_{r=\infty} + \ln r \ln r_\odot|_{r=\infty} \\
& + \ln\left(1 - \frac{r_\odot}{r}\right)\ln r_\odot\Big|_{r=\infty} \Bigg\} \\
= \frac{1}{r_s^4}\Bigg\{ & \frac{\pi^2}{2} + \ln r \ln\left(1 + \frac{r_\odot}{r}\right)\Big|_{r=\infty} - \ln r \ln\left(1 - \frac{r_\odot}{r}\right)\Big|_{r=\infty} \Bigg\} \\
= \frac{1}{r_s^4}\Bigg\{ & \frac{\pi^2}{2} + \ln r \ln\frac{1 + \frac{r_\odot}{r}}{1 - \frac{r_\odot}{r}}\Big|_{r=\infty} \Bigg\} \\
& \text{with } \ln\frac{1+x}{1-x} \approx 2x \text{ ,for } |x| \ll 1 \\
= & \frac{\pi^2}{2r_s^4} + \frac{2r_\odot}{r r_s^4}\ln r\Big|_{r=\infty} \\
& \text{with } \lim_{r\to\infty}\frac{\ln r}{r} = \lim_{r\to\infty}\frac{\frac{1}{r}}{r} = \lim_{r\to\infty}\frac{1}{r} = 0 \\
= & \frac{\pi^2}{2r_s^4}
\end{aligned}
$$

Calculation of the contribution from integral (II)

$$
\begin{aligned}
(\mathrm{II}) &= \int_0^\infty \mathrm{d}r \frac{1}{r_s^4\,(r+r_s)} \ln\frac{r+r_\odot}{|r-r_\odot|} \\
&= \frac{1}{r_s^4} \underbrace{\int_0^\infty \mathrm{d}r \frac{1}{r+r_s} \ln\left(r+r_\odot\right)}_{(\mathrm{IIa})} - \frac{1}{r_s^4} \underbrace{\int_0^{r_\odot} \mathrm{d}r \frac{1}{r+r_s} \ln\left(r_\odot - r\right)}_{(\mathrm{IIb})} \\
&\quad - \frac{1}{r_s^4} \underbrace{\int_{r_\odot}^\infty \mathrm{d}r \frac{1}{r+r_s} \ln\left(r-r_\odot\right)}_{(\mathrm{IIc})}
\end{aligned}
\tag{B.12}
$$

Calculation of contribution (IIa) to integral (II)

$$
\begin{aligned}
(\mathrm{IIa}) &= \int_0^\infty \mathrm{d}r \frac{1}{r+r_s} \ln\left(r+r_\odot\right) \\
&= \ln\left(r+r_s\right)\ln\left(r+r_\odot\right)\big|_0^\infty - \int_0^\infty \mathrm{d}r \frac{\ln\left(r+r_s\right)}{r+r_\odot} \\
&= \ln\left(r+r_s\right)\ln\left(r+r_\odot\right)\big|_0^\infty - \int_0^\infty \mathrm{d}r \frac{\ln\left(r+r_s\right)}{r+r_s-\left(r_s-r_\odot\right)} \\
&= \ln\left(r+r_s\right)\ln\left(r+r_\odot\right)\big|_0^\infty + \int_0^\infty \mathrm{d}r \frac{\ln\left(r+r_s\right)}{\left(r_s-r_\odot\right)\left(1-\frac{r+r_s}{r_s-r_\odot}\right)} \\
&= \ln\left(r+r_s\right)\ln\left(r+r_\odot\right)\big|_0^\infty + \int_0^\infty \mathrm{d}r \frac{\left\{\ln\frac{(r+r_s)}{r_s-r_\odot} + \ln\left(r_s-r_\odot\right)\right\}}{\left(r_s-r_\odot\right)\left(1-\frac{r+r_s}{r_s-r_\odot}\right)} \\
&\quad \text{with } t = \frac{r+r_s}{r_s-r_\odot} \Rightarrow \frac{\mathrm{d}t}{\mathrm{d}r} = \frac{1}{r_s-r_\odot} \Rightarrow \mathrm{d}r = \left(r_s-r_\odot\right)\mathrm{d}t \\
&= \ln\left(r+r_s\right)\ln\left(r+r_\odot\right)\big|_0^\infty + \int_{\frac{r_s}{r_s-r_\odot}}^\infty \mathrm{d}t \frac{\ln t}{1-t} - \int_0^\infty \mathrm{d}r \frac{\ln\left(r_s-r_\odot\right)}{r+r_\odot} \\
&= \ln\left(r+r_s\right)\ln\left(r+r_\odot\right)\big|_0^\infty + \int_1^\infty \mathrm{d}t \frac{\ln t}{1-t} - \int_1^{\frac{r_s}{r_s-r_\odot}} \mathrm{d}t \frac{\ln t}{1-t} \\
&\quad - \ln\left(r+r_\odot\right)\ln\left(r_s-r_\odot\right)\big|_0^\infty \\
&= \ln\left(r+r_s\right)\ln\left(r+r_\odot\right)\big|_0^\infty + L_2\left(\frac{r+r_s}{r_s-r_\odot}\right)\Big|_{r=\infty} - L_2\left(\frac{r_s}{r_s-r_\odot}\right) \\
&\quad - \ln\left(r+r_\odot\right)\ln\left(r_s-r_\odot\right)\big|_0^\infty
\end{aligned}
\tag{B.13}
$$

Calculation of contribution (IIb) to integral (II)

$$
\begin{aligned}
(\mathrm{IIb}) &= \int_0^{r_\odot} \mathrm{d}r \frac{\ln\left(r_\odot - r\right)}{r+r_s} \\
&= \int_0^{r_\odot} \mathrm{d}r \frac{\ln\left(r_\odot - r\right)}{r_\odot + r_s - \left(r_\odot - r\right)} \\
&= \int_0^{r_\odot} \mathrm{d}r \frac{\ln\left(r_\odot - r\right)}{\left(r_\odot+r_s\right)\left(1-\frac{r_\odot - r}{r_\odot + r_s}\right)} \\
&= \int_0^{r_\odot} \mathrm{d}r \frac{\ln\frac{r_\odot - r}{r_\odot + r_s} + \ln\left(r_\odot + r_s\right)}{\left(r_\odot+r_s\right)\left(1-\frac{r_\odot - r}{r_\odot + r_s}\right)}
\end{aligned}
\tag{B.14}
$$

$$\text{with } t = \frac{r_\odot - r}{r_\odot + r_s} \Rightarrow \frac{\mathrm{d}t}{\mathrm{d}r} = -\frac{1}{r_\odot + r_s} \Rightarrow \mathrm{d}r = -\left(r_\odot + r_s\right)\mathrm{d}t$$

$$\begin{aligned}
\text{(IIb)} &= -\int_{\frac{r_\odot}{r_\odot + r_s}}^{0} \mathrm{d}t \frac{\ln t}{1-t} + \int_0^{r_\odot} \mathrm{d}r \frac{\ln\left(r_\odot + r_s\right)}{r + r_s} \\
&= -\int_1^0 \mathrm{d}t \frac{\ln t}{1-t} + \int_1^{\frac{r_\odot}{r_\odot + r_s}} \mathrm{d}t \frac{\ln t}{1-t} + \int_0^{r_\odot} \mathrm{d}r \frac{\ln\left(r_\odot + r_s\right)}{r + r_s} \\
&= -\frac{\pi^2}{6} + L_2\left(\frac{r_\odot}{r_\odot + r_s}\right) + \ln\left(r + r_s\right)\ln\left(r_\odot + r_s\right)\big|_0^{r_\odot}
\end{aligned}$$

Calculation of contribution (IIc) to integral (II)

$$\begin{aligned}
\text{(IIc)} &= \int_{r_\odot}^{\infty} \mathrm{d}r \frac{\ln\left(r - r_\odot\right)}{r + r_s} \\
&= \ln\left(r + r_s\right)\ln\left(r - r_\odot\right)\big|_{r_\odot}^{\infty} - \int_{r_\odot}^{\infty} \mathrm{d}r \frac{\ln\left(r + r_s\right)}{r - r_\odot} \\
&= \ln\left(r + r_s\right)\ln\left(r - r_\odot\right)\big|_{r_\odot}^{\infty} - \int_{r_\odot}^{\infty} \mathrm{d}r \frac{\ln\left(r + r_s\right)}{r + r_s - \left(r_\odot + r_s\right)} \\
&= \ln\left(r + r_s\right)\ln\left(r - r_\odot\right)\big|_{r_\odot}^{\infty} + \int_{r_\odot}^{\infty} \mathrm{d}r \frac{\ln\left(r + r_s\right)}{r_\odot + r_s - \left(r + r_s\right)} \\
&= \ln\left(r + r_s\right)\ln\left(r - r_\odot\right)\big|_{r_\odot}^{\infty} + \int_{r_\odot}^{\infty} \mathrm{d}r \frac{\ln\left(r + r_s\right)}{\left(r_\odot + r_s\right)\left(1 - \frac{r + r_s}{r_\odot + r_s}\right)} \qquad \text{(B.15)} \\
&= \ln\left(r + r_s\right)\ln\left(r - r_\odot\right)\big|_{r_\odot}^{\infty} + \int_{r_\odot}^{\infty} \mathrm{d}r \frac{\ln\frac{r + r_s}{r_\odot + r_s} + \ln\left(r_\odot + r_s\right)}{\left(r_\odot + r_s\right)\left(1 - \frac{r + r_s}{r_\odot + r_s}\right)}
\end{aligned}$$

$$\text{with } t = \frac{r + r_s}{r_\odot + r_s} \Rightarrow \frac{\mathrm{d}t}{\mathrm{d}r} = \frac{1}{r_\odot + r_s} \Rightarrow \mathrm{d}r = \left(r_\odot + r_s\right)\mathrm{d}t$$

$$\begin{aligned}
&= \ln\left(r + r_s\right)\ln\left(r - r_\odot\right)\big|_{r_\odot}^{\infty} + \int_1^{\infty} \mathrm{d}t \frac{\ln t}{1-t} - \int_{r_\odot}^{\infty} \mathrm{d}r \frac{\ln\left(r_\odot + r_s\right)}{r - r_\odot} \\
&= \ln\left(r + r_s\right)\ln\left(r - r_\odot\right)\big|_{r_\odot}^{\infty} + L_2\left(\frac{r + r_s}{r_\odot + r_s}\right)\Big|_{r=\infty} - \ln\left(r - r_\odot\right)\ln\left(r_\odot + r_s\right)\big|_{r_\odot}^{\infty}
\end{aligned}$$

With the results from equations (IIa), (IIb), and (IIc) that were derived on the previous pages a solution for integral (II) is calculated.

$$\begin{aligned}
\text{(II)} = \frac{1}{r_s^4}\Bigg\{ &\ln\left(r + r_s\right)\ln\left(r + r_\odot\right)\big|_0^{\infty} + L_2\left(\frac{r + r_s}{r_s - r_\odot}\right)\Big|_{r=\infty} - L_2\left(\frac{r_s}{r_s - r_\odot}\right) \qquad \text{(B.16)} \\
&- \ln\left(r + r_\odot\right)\ln\left(r_s - r_\odot\right)\big|_0^{\infty} + \frac{\pi^2}{6} - L_2\left(\frac{r_\odot}{r_\odot + r_s}\right) - \ln\left(r + r_s\right)\ln\left(r_\odot + r_s\right)\big|_0^{r_\odot} \\
&- \ln\left(r + r_s\right)\ln\left(r - r_\odot\right)\big|_{r_\odot}^{\infty} - L_2\left(\frac{r + r_s}{r_\odot + r_s}\right)\Big|_{r=\infty} + \ln\left(r - r_\odot\right)\ln\left(r_\odot + r_s\right)\big|_{r_\odot}^{\infty}\Bigg\}
\end{aligned}$$

$$\text{with } L_2\left(\frac{1}{x}\right) = -L_2(x) - \frac{1}{2}\ln^2(x) \text{ ,for } 0 \le x \le 1$$

$$
\begin{aligned}
(\mathrm{II}) = \frac{1}{r_s^4}\Bigg\{ & \ln(r+r_s)\ln(r+r_\odot)|_{r=\infty} - \ln r_s \ln r_\odot - \frac{\pi^2}{6} - \frac{1}{2}\ln^2\frac{r_s-r_\odot}{r+r_s}\Big|_{r=\infty} \\
& - L_2\left(\frac{r_s}{r_s-r_\odot}\right) - \ln(r+r_\odot)\ln(r_s-r_\odot)|_{r=\infty} + \ln r_\odot \ln(r_s-r_\odot) + \frac{\pi^2}{6} \\
& - L_2\left(\frac{r_\odot}{r_\odot+r_s}\right) - \ln^2(r_\odot+r_s) + \ln r_s \ln(r_\odot+r_s) - \ln(r+r_s)\ln(r-r_\odot)|_{r=\infty} \\
& + \ln(r+r_s)\ln(r-r_\odot)|_{r=r_\odot} + \frac{\pi^2}{6} + \frac{1}{2}\ln^2\frac{r_\odot+r_s}{r+r_s}\Big|_{r=\infty} \\
& + \ln(r-r_\odot)\ln(r_\odot+r_s)|_{r=\infty} - \ln(r-r_\odot)\ln(r_\odot+r_s)|_{r=r_\odot}\Bigg\} \\
= \frac{1}{r_s^4}\Bigg\{ & \frac{\pi^2}{6} + \ln(r+r_s)\ln(r+r_\odot)|_{r=\infty} - \ln r_s \ln r_\odot - \frac{1}{2}\ln^2(r_s-r_\odot) \\
& + \ln(r_s-r_\odot)\ln(r+r_s)|_{r=\infty} - \frac{1}{2}\ln^2(r+r_s)\Big|_{r=\infty} - L_2\left(\frac{r_s}{r_s-r_\odot}\right) \\
& - \ln(r+r_\odot)\ln(r_s-r_\odot)|_{r=\infty} + \ln r_\odot \ln(r_s-r_\odot) - L_2\left(\frac{r_\odot}{r_\odot+r_s}\right) \\
& - \ln^2(r_\odot+r_s) + \ln r_s \ln(r_\odot+r_s) - \ln(r+r_s)\ln(r-r_\odot)|_{r=\infty} + \frac{1}{2}\ln^2(r_\odot+r_s) \\
& - \ln(r_\odot+r_s)\ln(r+r_s)|_{r=\infty} + \frac{1}{2}\ln^2(r+r_s)\Big|_{r=\infty} + \ln(r-r_\odot)\ln(r_\odot+r_s)|_{r=\infty}\Bigg\} \\
= \frac{1}{r_s^4}\Bigg\{ & \frac{\pi^2}{6} + \ln^2 r\big|_{r=\infty} + \ln\left(1+\frac{r_s}{r}\right)\ln r\Big|_{r=\infty} + \ln r \ln\left(1+\frac{r_\odot}{r}\right)\Big|_{r=\infty} \\
& + \ln\left(1+\frac{r_s}{r}\right)\ln\left(1+\frac{r_\odot}{r}\right)\Big|_{r=\infty} - \ln r_s \ln r_\odot - \frac{1}{2}\ln^2(r_s-r_\odot) + \ln(r_s-r_\odot)\ln r|_{r=\infty} \\
& + \ln(r_s-r_\odot)\ln\left(1+\frac{r_s}{r}\right)\Big|_{r=\infty} - \frac{1}{2}\ln^2 r\Big|_{r=\infty} - \ln r \ln\left(1+\frac{r_s}{r}\right)\Big|_{r=\infty} \\
& - \frac{1}{2}\ln^2\left(1+\frac{r_s}{r}\right)\Big|_{r=\infty} - L_2\left(\frac{r_s}{r_s-r_\odot}\right) - \ln r \ln(r_s-r_\odot)|_{r=\infty} \\
& - \ln\left(1+\frac{r_\odot}{r}\right)\ln(r_s-r_\odot)\Big|_{r=\infty} + \ln r_\odot \ln(r_s-r_\odot) - L_2\left(\frac{r_\odot}{r_\odot+r_s}\right) - \ln^2(r_\odot+r_s) \\
& + \ln r_s \ln(r_\odot+r_s) - \ln^2 r\big|_{r=\infty} - \ln\left(1+\frac{r_s}{r}\right)\ln r\Big|_{r=\infty} - \ln r \ln\left(1-\frac{r_\odot}{r}\right)\Big|_{r=\infty} \\
& - \ln\left(1+\frac{r_s}{r}\right)\ln\left(1-\frac{r_\odot}{r}\right)\Big|_{r=\infty} + \frac{1}{2}\ln^2(r_\odot+r_s) - \ln(r_\odot+r_s)\ln r|_{r=\infty} \\
& - \ln(r_\odot+r_s)\ln\left(1+\frac{r_s}{r}\right)\Big|_{r=\infty} + \frac{1}{2}\ln^2 r\Big|_{r=\infty} + \ln r \ln\left(1+\frac{r_s}{r}\right)\Big|_{r=\infty} \\
& + \frac{1}{2}\ln^2\left(1+\frac{r_s}{r}\right)\Big|_{r=\infty} + \ln r \ln(r_\odot+r_s)|_{r=\infty} + \ln\left(1-\frac{r_\odot}{r}\right)\ln(r_\odot+r_s)\Big|_{r=\infty}\Bigg\} \\
= \frac{1}{r_s^4}\Bigg\{ & \frac{\pi^2}{6} + \ln r \ln\left(1+\frac{r_\odot}{r}\right)\Big|_{r=\infty} - \ln r_s \ln r_\odot - \frac{1}{2}\ln^2(r_s-r_\odot) - L_2\left(\frac{r_s}{r_s-r_\odot}\right) \\
& + \ln r_\odot \ln(r_s-r_\odot) - L_2\left(\frac{r_\odot}{r_\odot+r_s}\right) - \frac{1}{2}\ln^2(r_\odot+r_s) + \ln r_s \ln(r_\odot+r_s) \\
& - \ln r \ln\left(1-\frac{r_\odot}{r}\right)\Big|_{r=\infty}\Bigg\} \\
= \frac{1}{r_s^4}\Bigg\{ & \frac{\pi^2}{6} + \ln r \ln\frac{1+\frac{r_\odot}{r}}{1-\frac{r_\odot}{r}}\Big|_{r=\infty} - \ln r_s \ln r_\odot - \frac{1}{2}\ln^2(r_s-r_\odot) - L_2\left(\frac{r_s}{r_s-r_\odot}\right) \\
& + \ln r_\odot \ln(r_s-r_\odot) - L_2\left(\frac{r_\odot}{r_\odot+r_s}\right) - \frac{1}{2}\ln^2(r_\odot+r_s) + \ln r_s \ln(r_\odot+r_s)\Bigg\}
\end{aligned}
$$

$$\text{with } \ln\frac{1+x}{1-x} \approx 2x \text{ ,for } |x| \ll 1$$

$$\begin{aligned}
(\text{II}) &= \frac{1}{r_s^4}\left\{\frac{\pi^2}{6} + 2\frac{r_\odot}{r}\ln r\Big|_{r=\infty} - \ln r_s \ln r_\odot - \frac{1}{2}\ln^2(r_s - r_\odot) - L_2\left(\frac{r_s}{r_s - r_\odot}\right)\right. \\
&\quad \left. + \ln r_\odot \ln(r_s - r_\odot) - L_2\left(\frac{r_\odot}{r_\odot + r_s}\right) - \frac{1}{2}\ln^2(r_\odot + r_s) + \ln r_s \ln(r_\odot + r_s)\right\} \\
&= \frac{1}{r_s^4}\left\{\frac{\pi^2}{6} - \ln r_s \ln r_\odot - \frac{1}{2}\ln^2(r_s - r_\odot) - L_2\left(\frac{r_s}{r_s - r_\odot}\right) + \ln r_\odot \ln(r_s - r_\odot)\right. \\
&\quad \left. - L_2\left(\frac{r_\odot}{r_\odot + r_s}\right) - \frac{1}{2}\ln^2(r_\odot + r_s) + \ln r_s \ln(r_\odot + r_s)\right\} \\
&= \frac{1}{r_s^4}\left\{\frac{\pi^2}{6} - \ln r_s \ln r_\odot - \frac{1}{2}\ln^2\frac{r_s - r_\odot}{r_s + r_\odot} - \ln(r_s - r_\odot)\ln(r_s + r_\odot) - L_2\left(\frac{r_s}{r_s - r_\odot}\right)\right. \\
&\quad \left. + \ln r_\odot \ln(r_s - r_\odot) - L_2\left(\frac{r_\odot}{r_\odot + r_s}\right) + \ln r_s \ln(r_\odot + r_s)\right\} \\
&= \frac{1}{r_s^4}\left\{\frac{\pi^2}{6} + \ln r_s \ln\frac{r_\odot + r_s}{r_\odot} - \frac{1}{2}\ln^2\frac{r_s - r_\odot}{r_s + r_\odot} + \ln(r_s - r_\odot)\ln\frac{r_\odot}{r_s + r_\odot} - L_2\left(\frac{r_s}{r_s - r_\odot}\right)\right. \\
&\quad \left. - L_2\left(\frac{r_\odot}{r_\odot + r_s}\right)\right\} \\
&= \frac{1}{r_s^4}\left\{\frac{\pi^2}{6} + \ln\frac{r_s}{r_s - r_\odot}\ln\frac{r_\odot + r_s}{r_\odot} - \frac{1}{2}\ln^2\frac{r_s - r_\odot}{r_s + r_\odot} - L_2\left(\frac{r_s}{r_s - r_\odot}\right) - L_2\left(\frac{r_\odot}{r_\odot + r_s}\right)\right\}
\end{aligned}$$

Calculation of the contribution from integral (III)

$$\begin{aligned}
(\text{III}) &= \int_0^\infty \mathrm{d}r \frac{1}{r_s^3(r + r_s)^2}\ln\frac{r + r_\odot}{|r - r_\odot|} \\
&= \frac{1}{r_s^3}\underbrace{\int_0^\infty \mathrm{d}r\,\frac{1}{(r + r_s)^2}\ln(r + r_\odot)}_{(\text{IIIa})} - \frac{1}{r_s^3}\underbrace{\int_0^{r_\odot} \mathrm{d}r\,\frac{1}{(r + r_s)^2}\ln(r_\odot - r)}_{(\text{IIIb})} \\
&\quad - \frac{1}{r_s^3}\underbrace{\int_{r_\odot}^\infty \mathrm{d}r\,\frac{1}{(r + r_s)^2}\ln(r - r_\odot)}_{(\text{IIIc})}
\end{aligned} \tag{B.17}$$

Calculation of contribution (IIIa) to integral (III)

$$\begin{aligned}
(\text{IIIa}) &= \int_0^\infty \mathrm{d}r \frac{1}{(r + r_s)^2}\ln(r + r_\odot) \\
&= -\frac{1}{r + r_s}\ln(r + r_\odot)\Big|_0^\infty - \int_0^\infty \mathrm{d}r\left(-\frac{1}{r + r_s}\right)\frac{1}{r + r_\odot} \\
&= -\frac{1}{r + r_s}\ln(r + r_\odot)\Big|_0^\infty + \int_0^\infty \mathrm{d}r \frac{1}{(r + r_s)(r + r_\odot)} \\
&\quad \text{with } \frac{1}{(r + r_s)(r + r_\odot)} = \frac{1}{(r_\odot - r_s)(r + r_s)} - \frac{1}{(r_\odot - r_s)(r + r_\odot)} \\
&= -\frac{\ln(r + r_\odot)}{r + r_s}\Big|_0^\infty + \int_0^\infty \mathrm{d}r \frac{1}{(r_\odot - r_s)(r + r_s)} - \int_0^\infty \mathrm{d}r \frac{1}{(r_\odot - r_s)(r + r_\odot)} \\
&= -\frac{\ln(r + r_\odot)}{r + r_s}\Big|_0^\infty + \frac{\ln(r + r_s)}{r_\odot - r_s}\Big|_0^\infty - \frac{\ln(r + r_\odot)}{r_\odot - r_s}\Big|_0^\infty
\end{aligned} \tag{B.18}$$

$$
\begin{aligned}
\text{(IIIa)} = &- \left.\frac{\ln\left(r+r_\odot\right)}{r+r_s}\right|_{r=\infty} + \frac{\ln r_\odot}{r_s} + \left.\frac{\ln\left(r+r_s\right)}{r_\odot - r_s}\right|_{r=\infty} - \frac{\ln r_s}{r_\odot - r_s} - \left.\frac{\ln\left(r+r_\odot\right)}{r_\odot - r_s}\right|_{r=\infty} \\
&+ \frac{\ln r_\odot}{r_\odot - r_s} \\
&\text{with } \lim_{r\to\infty} \frac{\ln\left(r+r_\odot\right)}{r+r_s} = \lim_{r\to\infty} \frac{\frac{1}{r+r_\odot}}{1} = \lim_{r\to\infty} \frac{1}{r+r_\odot} = 0 \\
&\left.\frac{\ln\left(r+r_s\right)}{r_\odot - r_s}\right|_{r=\infty} = \left.\frac{\ln\left(r+r_\odot\right)}{r_\odot - r_s}\right|_{r=\infty} \\
= &\frac{\ln r_\odot}{r_s} - \frac{\ln r_s}{r_\odot - r_s} + \frac{\ln r_\odot}{r_\odot - r_s} \\
= &\frac{r_\odot \ln r_\odot - r_s \ln r_s}{r_s\left(r_\odot - r_s\right)}
\end{aligned}
$$

Calculation of contribution (IIIb) to integral (III)

$$
\begin{aligned}
\text{(IIIb)} = &\int_0^{r_\odot} \mathrm{d}r \frac{1}{\left(r+r_s\right)^2} \ln\left(r_\odot - r\right) \\
= &- \left.\frac{1}{r+r_s} \ln\left(r_\odot - r\right)\right|_0^{r_\odot} - \int_0^{r_\odot} \mathrm{d}r \left(-\frac{1}{r+r_s}\right)\left(-\frac{1}{r_\odot - r}\right) \\
= &- \left.\frac{1}{r+r_s} \ln\left(r_\odot - r\right)\right|_0^{r_\odot} - \int_0^{r_\odot} \mathrm{d}r \frac{1}{\left(r+r_s\right)\left(r_\odot - r\right)} \\
&\text{with } \frac{1}{\left(r+r_s\right)\left(r_\odot - r\right)} = \frac{1}{\left(r_\odot + r_s\right)\left(r+r_s\right)} + \frac{1}{\left(r_\odot + r_s\right)\left(r_\odot - r\right)} \\
= &- \left.\frac{\ln\left(r_\odot - r\right)}{r+r_s}\right|_0^{r_\odot} - \int_0^{r_\odot} \mathrm{d}r \frac{1}{\left(r_\odot + r_s\right)\left(r+r_s\right)} - \int_0^{r_\odot} \mathrm{d}r \frac{1}{\left(r_\odot + r_s\right)\left(r_\odot - r\right)} \qquad \text{(B.19)} \\
= &- \left.\frac{\ln\left(r_\odot - r\right)}{r+r_s}\right|_0^{r_\odot} - \left.\frac{\ln\left(r+r_s\right)}{r_\odot + r_s}\right|_0^{r_\odot} + \left.\frac{\ln\left(r_\odot - r\right)}{r_\odot + r_s}\right|_0^{r_\odot} \\
= &- \left.\frac{\ln\left(r_\odot - r\right)}{r+r_s}\right|_{r=r_\odot} + \frac{\ln r_\odot}{r_s} - \frac{\ln\left(r_\odot + r_s\right)}{r_\odot + r_s} + \frac{\ln r_s}{r_\odot + r_s} + \left.\frac{\ln\left(r_\odot - r\right)}{r_\odot + r_s}\right|_{r=r_\odot} - \frac{\ln r_\odot}{r_\odot + r_s} \\
&\text{with } \left.\frac{\ln\left(r_\odot - r\right)}{r+r_s}\right|_{r=r_\odot} = \left.\frac{\ln\left(r_\odot - r\right)}{r_\odot + r_s}\right|_{r=r_\odot} \\
= &\frac{\ln r_\odot}{r_s} - \frac{\ln\left(r_\odot + r_s\right)}{r_\odot + r_s} + \frac{\ln r_s}{r_\odot + r_s} - \frac{\ln r_\odot}{r_\odot + r_s} \\
= &\frac{r_\odot \ln r_\odot - r_s \ln\left(r_\odot + r_s\right) + r_s \ln r_s}{r_s\left(r_\odot + r_s\right)}
\end{aligned}
$$

Calculation of contribution (IIIc) to integral (III)

$$
\begin{aligned}
\text{(IIIc)} = &\int_{r_\odot}^{\infty} \mathrm{d}r \frac{1}{\left(r+r_s\right)^2} \ln\left(r - r_\odot\right) \\
= &- \left.\frac{1}{r+r_s} \ln\left(r - r_\odot\right)\right|_{r_\odot}^{\infty} - \int_{r_\odot}^{\infty} \mathrm{d}r \left(-\frac{1}{r+r_s}\right) \frac{1}{r - r_\odot} \qquad \text{(B.20)} \\
= &- \left.\frac{1}{r+r_s} \ln\left(r - r_\odot\right)\right|_{r_\odot}^{\infty} + \int_{r_\odot}^{\infty} \mathrm{d}r \frac{1}{\left(r+r_s\right)\left(r - r_\odot\right)} \\
&\text{with } \frac{1}{\left(r+r_s\right)\left(r - r_\odot\right)} = -\frac{1}{\left(r_\odot + r_s\right)\left(r+r_s\right)} + \frac{1}{\left(r_\odot + r_s\right)\left(r - r_\odot\right)}
\end{aligned}
$$

$$
\begin{aligned}
\text{(IIIc)} &= -\left.\frac{\ln(r-r_\odot)}{r+r_s}\right|_{r_\odot}^{\infty} - \int_{r_\odot}^{\infty} \mathrm{d}r \frac{1}{(r_\odot+r_s)(r+r_s)} + \int_{r_\odot}^{\infty} \mathrm{d}r \frac{1}{(r_\odot+r_s)(r-r_\odot)} \\
&= -\left.\frac{\ln(r-r_\odot)}{r+r_s}\right|_{r_\odot}^{\infty} - \left.\frac{\ln(r+r_s)}{r_\odot+r_s}\right|_{r_\odot}^{\infty} + \left.\frac{\ln(r-r_\odot)}{r_\odot+r_s}\right|_{r_\odot}^{\infty} \\
&= -\left.\frac{\ln(r-r_\odot)}{r+r_s}\right|_{r=\infty} + \left.\frac{\ln(r-r_\odot)}{r+r_s}\right|_{r=r_\odot} - \left.\frac{\ln(r+r_s)}{r_\odot+r_s}\right|_{r=\infty} + \frac{\ln(r_\odot+r_s)}{r_\odot+r_s} \\
&\quad + \left.\frac{\ln(r-r_\odot)}{r_\odot+r_s}\right|_{r=\infty} - \left.\frac{\ln(r-r_\odot)}{r_\odot+r_s}\right|_{r=r_\odot} \\
&\quad \text{with} \quad \lim_{r\to\infty} \frac{\ln(r-r_\odot)}{r+r_s} = \lim_{r\to\infty} \frac{\frac{1}{r-r_\odot}}{1} = \lim_{r\to\infty} \frac{1}{r-r_\odot} = 0 \\
&\qquad \left.\frac{\ln(r-r_\odot)}{r+r_s}\right|_{r=r_\odot} = \left.\frac{\ln(r-r_\odot)}{r_\odot+r_s}\right|_{r=r_\odot} \\
&\qquad \left.\frac{\ln(r+r_s)}{r_\odot+r_s}\right|_{r=\infty} = \left.\frac{\ln(r-r_\odot)}{r_\odot+r_s}\right|_{r=\infty} \\
&= \frac{\ln(r_\odot+r_s)}{r_\odot+r_s}
\end{aligned}
$$

With the results from equations (IIIa), (IIIb), and (IIIc) that were derived on the previous pages a solution for integral (III) is calculated.

$$
\begin{aligned}
\text{(III)} &= \frac{1}{r_s^3}\left\{\frac{r_\odot \ln r_\odot - r_s \ln r_s}{r_s(r_\odot - r_s)} - \frac{r_\odot \ln r_\odot - r_s \ln(r_\odot+r_s) + r_s \ln r_s}{r_s(r_\odot+r_s)} - \frac{\ln(r_\odot+r_s)}{r_\odot+r_s}\right\} \\
&= \frac{1}{r_s^3}\left\{\frac{r_\odot \ln r_\odot - r_s \ln r_s}{r_s(r_\odot - r_s)} - \frac{r_\odot \ln r_\odot + r_s \ln r_s}{r_s(r_\odot+r_s)}\right\} \\
&= \frac{1}{r_s^3}\left\{\frac{(r_\odot+r_s) r_\odot \ln r_\odot - (r_\odot+r_s) r_s \ln r_s - (r_\odot - r_s) r_\odot \ln r_\odot - (r_\odot - r_s) r_s \ln r_s}{r_s(r_\odot - r_s)(r_\odot+r_s)}\right\} \\
&= \frac{2r_\odot}{r_s^3\left(r_s^2 - r_\odot^2\right)} \ln\frac{r_s}{r_\odot}
\end{aligned}
\tag{B.21}
$$

Calculation of the contribution from integral (IV)

$$
\begin{aligned}
\text{(IV)} &= \int_0^{\infty} \mathrm{d}r \frac{1}{r_s^2(r+r_s)^3} \ln\frac{r+r_\odot}{|r-r_\odot|} \\
&= \frac{1}{r_s^2} \underbrace{\int_0^{\infty} \mathrm{d}r \, \frac{1}{(r+r_s)^3} \ln(r+r_\odot)}_{\text{(IVa)}} - \frac{1}{r_s^2} \underbrace{\int_0^{r_\odot} \mathrm{d}r \, \frac{1}{(r+r_s)^3} \ln(r_\odot - r)}_{\text{(IVb)}} \\
&\quad - \frac{1}{r_s^2} \underbrace{\int_{r_\odot}^{\infty} \mathrm{d}r \frac{1}{(r+r_s)^3} \ln(r-r_\odot)}_{\text{(IVc)}}
\end{aligned}
\tag{B.22}
$$

Calculation of contribution (IVa) to integral (IV)

$$
\begin{aligned}
\text{(IVa)} &= -\left.\frac{\ln(r+r_\odot)}{2(r+r_s)^2}\right|_0^{\infty} - \int_0^{\infty} \mathrm{d}r \left(-\frac{1}{2(r+r_s)^2}\right) \frac{1}{r+r_\odot} \\
&= -\left.\frac{\ln(r+r_\odot)}{2(r+r_s)^2}\right|_0^{\infty} + \int_0^{\infty} \mathrm{d}r \frac{1}{2(r+r_s)^2(r+r_\odot)}
\end{aligned}
\tag{B.23}
$$

$$\text{with } \frac{1}{(r+r_s)^2(r+r_\odot)} = -\frac{1}{(r_\odot-r_s)^2(r+r_s)} + \frac{1}{(r_\odot-r_s)(r+r_s)^2} + \frac{1}{(r_\odot-r_s)^2(r+r_\odot)}$$

$$\begin{aligned}
\text{(IVa)} &= -\left.\frac{\ln(r+r_\odot)}{2(r+r_s)^2}\right|_0^\infty - \int_0^\infty \mathrm{d}r \frac{1}{2(r_\odot-r_s)^2(r+r_s)} + \int_0^\infty \mathrm{d}r \frac{1}{2(r_\odot-r_s)(r+r_s)^2} \\
&\quad + \int_0^\infty \mathrm{d}r \frac{1}{2(r_\odot-r_s)^2(r+r_\odot)} \\
&= -\left.\frac{\ln(r+r_\odot)}{2(r+r_s)^2}\right|_0^\infty - \left.\frac{\ln(r+r_s)}{2(r_\odot-r_s)^2}\right|_0^\infty - \left.\frac{1}{2(r_\odot-r_s)(r+r_s)}\right|_0^\infty + \left.\frac{\ln(r+r_\odot)}{2(r_\odot-r_s)^2}\right|_0^\infty \\
&= -\left.\frac{\ln(r+r_\odot)}{2(r+r_s)^2}\right|_{r=\infty} + \frac{\ln r_\odot}{2r_s^2} - \left.\frac{\ln(r+r_s)}{2(r_\odot-r_s)^2}\right|_{r=\infty} + \frac{\ln r_s}{2(r_\odot-r_s)^2} \\
&\quad - \left.\frac{1}{2(r_\odot-r_s)(r+r_s)}\right|_{r=\infty} + \frac{1}{2r_s(r_\odot-r_s)} + \left.\frac{\ln(r+r_\odot)}{2(r_\odot-r_s)^2}\right|_{r=\infty} - \frac{\ln r_\odot}{2(r_\odot-r_s)^2}
\end{aligned}$$

$$\text{with} \qquad \lim_{r\to\infty} \frac{\ln r + r_\odot}{2(r+r_s)^2} = \lim_{r\to\infty} \frac{\frac{1}{r+r_\odot}}{4(r+r_s)} = \lim_{r\to\infty} \frac{1}{4(r+r_s)(r+r_\odot)} = 0$$

$$\lim_{r\to\infty} \frac{1}{2(r_\odot+r_s)(r+r_s)} = 0$$

$$\left.\frac{\ln r + r_s}{2(r_\odot-r_s)^2}\right|_{r=\infty} = \left.\frac{\ln r + r_\odot}{2(r_\odot-r_s)^2}\right|_{r=\infty}$$

$$\begin{aligned}
&= \frac{\ln r_\odot}{2r_s^2} + \frac{\ln r_s}{2(r_\odot-r_s)^2} + \frac{1}{2r_s(r_\odot-r_s)} - \frac{\ln r_\odot}{2(r_\odot-r_s)^2} \\
&= \frac{\ln r_\odot}{2r_s^2} - \frac{1}{2(r_\odot-r_s)^2} \ln\frac{r_\odot}{r_s} + \frac{1}{2r_s(r_\odot-r_s)}
\end{aligned}$$

Calculation of contribution (IVb) to integral (IV)

$$\begin{aligned}
\text{(IVb)} &= -\left.\frac{\ln(r_\odot-r)}{2(r+r_s)^2}\right|_0^{r_\odot} - \int_0^{r_\odot} \mathrm{d}r \left(-\frac{1}{2(r+r_s)^2}\right)\left(-\frac{1}{r_\odot-r}\right) \\
&= -\left.\frac{\ln(r_\odot-r)}{2(r+r_s)^2}\right|_0^{r_\odot} - \int_0^{r_\odot} \mathrm{d}r \frac{1}{2(r+r_s)^2(r_\odot-r)}
\end{aligned}$$

$$\text{with } \frac{1}{(r+r_s)^2(r_\odot-r)} = \frac{1}{(r_\odot+r_s)^2(r+r_s)} + \frac{1}{(r_\odot+r_s)(r+r_s)^2} + \frac{1}{(r_\odot+r_s)^2(r_\odot-r)} \tag{B.24}$$

$$\begin{aligned}
&= -\left.\frac{\ln(r_\odot-r)}{2(r+r_s)^2}\right|_0^{r_\odot} - \int_0^{r_\odot} \mathrm{d}r \frac{1}{2(r_\odot+r_s)^2(r+r_s)} - \int_0^{r_\odot} \mathrm{d}r \frac{1}{2(r_\odot+r_s)(r+r_s)^2} \\
&\quad - \int_0^{r_\odot} \mathrm{d}r \frac{1}{2(r_\odot+r_s)^2(r_\odot-r)} \\
&= -\left.\frac{\ln(r_\odot-r)}{2(r+r_s)^2}\right|_0^{r_\odot} - \left.\frac{\ln(r+r_s)}{2(r_\odot+r_s)^2}\right|_0^{r_\odot} + \left.\frac{1}{2(r_\odot+r_s)(r+r_s)}\right|_0^{r_\odot} + \left.\frac{\ln(r_\odot-r)}{2(r_\odot+r_s)^2}\right|_0^{r_\odot}
\end{aligned}$$

$$
\begin{aligned}
(\mathrm{IVb}) = &- \frac{\ln(r_\odot - r)}{2(r+r_s)^2}\bigg|_{r=r_\odot} + \frac{\ln r_\odot}{2r_s^2} - \frac{\ln(r_\odot + r_s)}{2(r_\odot+r_s)^2} + \frac{\ln r_s}{2(r_\odot+r_s)^2} + \frac{1}{2(r_\odot+r_s)^2} \\
&- \frac{1}{2r_s(r_\odot+r_s)} + \frac{\ln(r_\odot - r)}{2(r_\odot+r_s)^2}\bigg|_{r=r_\odot} - \frac{\ln r_\odot}{2(r_\odot+r_s)^2} \\
&\text{with } \frac{\ln(r_\odot - r)}{2(r+r_s)^2}\bigg|_{r=r_\odot} = \frac{\ln(r_\odot - r)}{2(r_\odot+r_s)^2}\bigg|_{r=r_\odot} \\
= &\frac{\ln r_\odot}{2r_s^2} - \frac{\ln(r_\odot + r_s)}{2(r_\odot+r_s)^2} + \frac{\ln r_s}{2(r_\odot+r_s)^2} + \frac{1}{2(r_\odot+r_s)^2} - \frac{1}{2r_s(r_\odot+r_s)} - \frac{\ln r_\odot}{2(r_\odot+r_s)^2} \\
= &\frac{\ln r_\odot}{2r_s^2} + \frac{1}{2(r_\odot+r_s)^2}\ln\frac{r_s}{r_\odot(r_\odot+r_s)} - \frac{r_\odot}{2r_s(r_\odot+r_s)^2}
\end{aligned}
$$

Calculation of contribution (IVc) to integral (IV)

$$
\begin{aligned}
(\mathrm{IVc}) = &- \frac{\ln(r-r_\odot)}{2(r+r_s)^2}\bigg|_{r_\odot}^{\infty} - \int_{r_\odot}^{\infty} \mathrm{d}r \left(-\frac{1}{2(r+r_s)^2}\right)\frac{1}{r-r_\odot} \\
= &- \frac{\ln(r-r_\odot)}{2(r+r_s)^2}\bigg|_{r_\odot}^{\infty} + \int_{r_\odot}^{\infty} \mathrm{d}r \frac{1}{2(r+r_s)^2(r-r_\odot)} \\
&\text{with } \frac{1}{(r+r_s)^2(r-r_\odot)} = -\frac{1}{(r_\odot+r_s)^2(r+r_s)} - \frac{1}{(r_\odot+r_s)(r+r_s)^2} \\
&\qquad + \frac{1}{(r_\odot+r_s)^2(r-r_\odot)} \\
= &- \frac{\ln(r-r_\odot)}{2(r+r_s)^2}\bigg|_{r_\odot}^{\infty} - \int_{r_\odot}^{\infty} \mathrm{d}r \frac{1}{2(r_\odot+r_s)^2(r+r_s)} - \int_{r_\odot}^{\infty} \mathrm{d}r \frac{1}{2(r_\odot+r_s)(r+r_s)^2} \\
&+ \int_{r_\odot}^{\infty} \mathrm{d}r \frac{1}{2(r_\odot+r_s)^2(r-r_\odot)} \qquad (\mathrm{B.25}) \\
= &- \frac{\ln(r-r_\odot)}{2(r+r_s)^2}\bigg|_{r_\odot}^{\infty} - \frac{\ln(r+r_s)}{2(r_\odot+r_s)^2}\bigg|_{r_\odot}^{\infty} + \frac{1}{2(r_\odot+r_s)(r+r_s)}\bigg|_{r_\odot}^{\infty} + \frac{\ln(r-r_\odot)}{2(r_\odot+r_s)^2}\bigg|_{r_\odot}^{\infty} \\
= &- \frac{\ln(r-r_\odot)}{2(r+r_s)^2}\bigg|_{r=\infty} + \frac{\ln(r-r_\odot)}{2(r+r_s)^2}\bigg|_{r=r_\odot} - \frac{\ln(r+r_s)}{2(r_\odot+r_s)^2}\bigg|_{r=\infty} + \frac{\ln(r_\odot+r_s)}{2(r_\odot+r_s)^2} \\
&+ \frac{1}{2(r_\odot+r_s)(r+r_s)}\bigg|_{r=\infty} - \frac{1}{2(r_\odot+r_s)^2} + \frac{\ln(r-r_\odot)}{2(r_\odot+r_s)^2}\bigg|_{r=\infty} - \frac{\ln(r-r_\odot)}{2(r_\odot+r_s)^2}\bigg|_{r=r_\odot} \\
&\text{with} \qquad \lim_{r\to\infty}\frac{\ln(r-r_\odot)}{2(r+r_s)^2} = \lim_{r\to\infty}\frac{\frac{1}{r-r_\odot}}{4(r+r_s)} = \lim_{r\to\infty}\frac{1}{4(r-r_\odot)(r+r_s)} = 0 \\
&\lim_{r\to\infty}\frac{1}{2(r_\odot+r_s)(r+r_s)} = 0 \\
&\frac{\ln(r+r_s)}{2(r_\odot+r_s)^2}\bigg|_{r=\infty} = \frac{\ln(r-r_\odot)}{2(r_\odot+r_s)^2}\bigg|_{r=\infty} \\
&\frac{\ln(r-r_\odot)}{2(r+r_s)^2}\bigg|_{r=r_\odot} = \frac{\ln(r-r_\odot)}{2(r_\odot+r_s)^2}\bigg|_{r=r_\odot}
\end{aligned}
$$

$$(\mathrm{IVc}) = \frac{\ln\left(r_\odot + r_s\right)}{2\left(r_\odot + r_s\right)^2} - \frac{1}{2\left(r_\odot + r_s\right)^2}$$

With the results from equations (IVa), (IVb), and (IVc) that were derived on the previous pages a solution for integral (IV) is calculated.

$$\begin{aligned}
(\mathrm{IV}) &= \frac{1}{r_s^2}\left\{\frac{\ln r_\odot}{2r_s^2} + \frac{1}{2\left(r_\odot - r_s\right)^2}\ln\frac{r_s}{r_\odot} + \frac{1}{2r_s\left(r_\odot - r_s\right)} - \frac{\ln r_\odot}{2r_s^2}\right. \\
&\quad \left. - \frac{1}{2\left(r_\odot + r_s\right)^2}\ln\frac{r_s}{r_\odot\left(r_\odot + r_s\right)} + \frac{r_\odot}{2r_s\left(r_\odot + r_s\right)^2} - \frac{\ln\left(r_\odot + r_s\right)}{2\left(r_\odot + r_s\right)^2} + \frac{1}{2\left(r_\odot + r_s\right)^2}\right\} \\
&= \frac{1}{r_s^2}\left\{\frac{1}{2\left(r_\odot - r_s\right)^2}\ln\frac{r_s}{r_\odot} + \frac{1}{2r_s\left(r_\odot - r_s\right)} - \frac{1}{2\left(r_\odot + r_s\right)^2}\ln\frac{r_s}{r_\odot}\right. \\
&\quad \left. + \frac{r_\odot}{2r_s\left(r_\odot + r_s\right)^2} + \frac{1}{2\left(r_\odot + r_s\right)^2}\right\} \\
&= \frac{1}{r_s^2}\left\{\frac{2r_s r_\odot}{\left(r_\odot + r_s\right)^2\left(r_\odot - r_s\right)^2}\ln\frac{r_s}{r_\odot} + \frac{r_\odot}{r_s\left(r_\odot + r_s\right)\left(r_\odot - r_s\right)}\right\} \\
&= -\frac{2r_\odot}{r_s\left(r_\odot + r_s\right)^2\left(r_s - r_\odot\right)^2}\ln\frac{r_\odot}{r_s} - \frac{r_\odot}{r_s^3\left(r_\odot + r_s\right)\left(r_s - r_\odot\right)}
\end{aligned} \tag{B.26}$$

Calculation of the contribution from integral (V)

$$\begin{aligned}
(\mathrm{V}) &= \int_0^\infty \mathrm{d}r\,\frac{1}{r_s\left(r + r_s\right)^4}\ln\frac{r + r_\odot}{|r - r_\odot|} \\
&= \frac{1}{r_s}\underbrace{\int_0^\infty \mathrm{d}r\,\frac{1}{\left(r + r_s\right)^4}\ln\left(r + r_\odot\right)}_{(\mathrm{Va})} - \frac{1}{r_s}\underbrace{\int_0^{r_\odot} \mathrm{d}r\,\frac{1}{\left(r + r_s\right)^4}\ln\left(r_\odot - r\right)}_{(\mathrm{Vb})} \\
&\quad - \frac{1}{r_s}\underbrace{\int_{r_\odot}^\infty \mathrm{d}r\,\frac{1}{\left(r + r_s\right)^4}\ln\left(r - r_\odot\right)}_{(\mathrm{Vc})}
\end{aligned} \tag{B.27}$$

Calculation of contribution (Va) to integral (V)

$$\begin{aligned}
(\mathrm{Va}) &= -\frac{\ln\left(r + r_\odot\right)}{3\left(r + r_s\right)^3}\bigg|_0^\infty - \int_0^\infty \mathrm{d}r\left(-\frac{1}{3\left(r + r_s\right)^3}\right)\frac{1}{r + r_\odot} \\
&= -\frac{\ln\left(r + r_\odot\right)}{3\left(r + r_s\right)^3}\bigg|_0^\infty + \int_0^\infty \mathrm{d}r\frac{1}{3\left(r + r_s\right)^3}\frac{1}{r + r_\odot} \\
&\quad \text{with } \frac{1}{\left(r + r_s\right)^3\left(r + r_\odot\right)} = \frac{1}{\left(r_\odot - r_s\right)^3\left(r + r_s\right)} - \frac{1}{\left(r_\odot - r_s\right)^2\left(r + r_s\right)^2} \\
&\qquad\qquad + \frac{1}{\left(r_\odot - r_s\right)\left(r + r_s\right)^3} - \frac{1}{\left(r_\odot - r_s\right)^3\left(r + r_\odot\right)} \\
&= -\frac{\ln\left(r + r_\odot\right)}{3\left(r + r_s\right)^3}\bigg|_0^\infty + \int_0^\infty \mathrm{d}r\frac{1}{3\left(r - r_s\right)^3\left(r + r_s\right)} - \int_0^\infty \mathrm{d}r\frac{1}{3\left(r_\odot - r_s\right)^2\left(r + r_s\right)^2} \\
&\quad + \int_0^\infty \mathrm{d}r\frac{1}{3\left(r_\odot - r_s\right)\left(r + r_s\right)^3} - \int_0^\infty \mathrm{d}r\frac{1}{3\left(r_\odot - r_s\right)^3\left(r + r_\odot\right)}
\end{aligned} \tag{B.28}$$

$$
\begin{aligned}
\text{(Va)} = & -\frac{\ln\left(r+r_\odot\right)}{3\left(r+r_s\right)^3}\bigg|_0^\infty + \frac{\ln\left(r+r_s\right)}{3\left(r_\odot-r_s\right)^3}\bigg|_0^\infty + \frac{1}{3\left(r_\odot-r_s\right)^2\left(r+r_s\right)}\bigg|_0^\infty \\
& - \frac{1}{6\left(r_\odot-r_s\right)\left(r+r_s\right)^2}\bigg|_0^\infty - \frac{\ln\left(r+r_\odot\right)}{3\left(r_\odot-r_s\right)^3}\bigg|_0^\infty \\
= & -\frac{\ln\left(r+r_\odot\right)}{3\left(r+r_s\right)^3}\bigg|_{r=\infty} + \frac{\ln r_\odot}{3r_s^3} + \frac{\ln\left(r+r_s\right)}{3\left(r_\odot-r_s\right)^3}\bigg|_{r=\infty} - \frac{\ln r_s}{3\left(r_\odot-r_s\right)^3} \\
& + \frac{1}{3\left(r_\odot-r_s\right)^2\left(r+r_s\right)}\bigg|_{r=\infty} - \frac{1}{3r_s\left(r_\odot-r_s\right)^2} - \frac{1}{6\left(r_\odot-r_s\right)\left(r+r_s\right)^2}\bigg|_{r=\infty} \\
& + \frac{1}{6r_s^2\left(r_\odot-r_s\right)} - \frac{\ln\left(r+r_\odot\right)}{3\left(r_\odot-r_s\right)^3}\bigg|_{r=\infty} + \frac{\ln r_\odot}{3\left(r_\odot-r_s\right)^3} \\
& \text{with} \qquad \lim_{r\to\infty}\frac{\ln\left(r+r_\odot\right)}{3\left(r+r_s\right)^3} = \lim_{r\to\infty}\frac{\frac{1}{r+r_\odot}}{9\left(r+r_s\right)^2} = \lim_{r\to\infty}\frac{1}{9\left(r+r_s\right)^2\left(r+r_\odot\right)} = 0 \\
& \qquad \lim_{r\to\infty}\frac{1}{3\left(r_\odot-r_s\right)^2\left(r+r_s\right)} = 0 \\
& \qquad \lim_{r\to\infty}\frac{1}{6\left(r_\odot-r_s\right)\left(r+r_s\right)^2} = 0 \\
& \qquad \frac{\ln\left(r+r_s\right)}{3\left(r_\odot-r_s\right)^3}\bigg|_{r=\infty} = \frac{\ln\left(r+r_\odot\right)}{3\left(r_\odot-r_s\right)^3}\bigg|_{r=\infty} \\
= & \frac{\ln r_\odot}{3r_s^3} - \frac{\ln r_s}{3\left(r_\odot-r_s\right)^3} - \frac{1}{3r_s\left(r_\odot-r_s\right)^2} + \frac{1}{6r_s^2\left(r_\odot-r_s\right)} + \frac{\ln r_\odot}{3\left(r_\odot-r_s\right)^3} \\
= & \frac{\ln r_\odot}{3r_s^3} + \frac{1}{3\left(r_\odot-r_s\right)^3}\ln\frac{r_\odot}{r_s} + \frac{r_\odot-3r_s}{6r_s^2\left(r_\odot-r_s\right)^2}
\end{aligned}
$$

Calculation of contribution (Vb) to integral (V)

$$
\begin{aligned}
\text{(Vb)} = & -\frac{\ln\left(r_\odot-r\right)}{3\left(r+r_s\right)^3}\bigg|_0^{r_\odot} - \int_0^{r_\odot}\mathrm{d}r\left(-\frac{1}{3\left(r+r_s\right)^3}\right)\left(-\frac{1}{r_\odot-r}\right) \\
= & -\frac{\ln\left(r_\odot-r\right)}{3\left(r+r_s\right)^3}\bigg|_0^{r_\odot} - \int_0^{r_\odot}\mathrm{d}r\frac{1}{3\left(r+r_s\right)^3\left(r_\odot-r\right)} \\
& \text{with} \quad \frac{1}{\left(r+r_s\right)^3\left(r_\odot-r\right)} = \frac{1}{\left(r_\odot+r_s\right)^3\left(r+r_s\right)} + \frac{1}{\left(r_\odot+r_s\right)^2\left(r+r_s\right)^2} \\
& \qquad\qquad + \frac{1}{\left(r_\odot+r_s\right)\left(r+r_s\right)^3} + \frac{1}{\left(r_\odot+r_s\right)^3\left(r_\odot-r\right)} \qquad \text{(B.29)} \\
= & -\frac{\ln\left(r_\odot-r\right)}{3\left(r+r_s\right)^3}\bigg|_0^{r_\odot} - \int_0^{r_\odot}\mathrm{d}r\frac{1}{3\left(r_\odot+r_s\right)^3\left(r+r_s\right)} - \int_0^{r_\odot}\mathrm{d}r\frac{1}{3\left(r_\odot+r_s\right)^2\left(r+r_s\right)^2} \\
& - \int_0^{r_\odot}\mathrm{d}r\frac{1}{3\left(r_\odot+r_s\right)\left(r+r_s\right)^3} - \int_0^{r_\odot}\mathrm{d}r\frac{1}{3\left(r_\odot+r_s\right)^3\left(r_\odot-r\right)} \\
= & -\frac{\ln\left(r_\odot-r\right)}{3\left(r+r_s\right)^3}\bigg|_0^{r_\odot} - \frac{\ln\left(r+r_s\right)}{3\left(r_\odot+r_s\right)^3}\bigg|_0^{r_\odot} + \frac{1}{3\left(r_\odot+r_s\right)^2\left(r+r_s\right)}\bigg|_0^{r_\odot} \\
& + \frac{1}{6\left(r_\odot+r_s\right)\left(r+r_s\right)^2}\bigg|_0^{r_\odot} + \frac{\ln\left(r_\odot-r\right)}{3\left(r_\odot+r_s\right)^3}\bigg|_0^{r_\odot}
\end{aligned}
$$

$$
\begin{aligned}
\text{(Vb)} = & -\frac{\ln\left(r_\odot - r\right)}{3\left(r+r_s\right)^3}\bigg|_{r=r_\odot} + \frac{\ln r_\odot}{3r_s^3} - \frac{\ln\left(r_\odot + r_s\right)}{3\left(r_\odot + r_s\right)^3} + \frac{\ln r_s}{3\left(r_\odot + r_s\right)^3} + \frac{1}{3\left(r_\odot + r_s\right)^3} \\
& - \frac{1}{3r_s\left(r_\odot + r_s\right)^2} + \frac{1}{6\left(r_\odot + r_s\right)^3} - \frac{1}{6r_s^2\left(r_\odot + r_s\right)} + \frac{\ln\left(r_\odot - r\right)}{3\left(r_\odot + r_s\right)^3}\bigg|_{r=r_\odot} - \frac{\ln r_\odot}{3\left(r_\odot + r_s\right)^3} \\
& \text{with } \frac{\ln\left(r_\odot - r\right)}{3\left(r+r_s\right)^3}\bigg|_{r=r_\odot} = \frac{\ln\left(r_\odot - r\right)}{3\left(r_\odot + r_s\right)^3}\bigg|_{r=r_\odot} \\
= & \frac{\ln r_\odot}{3r_s^3} + \frac{1}{3\left(r_\odot + r_s\right)^3}\ln\frac{r_s}{r_\odot\left(r_\odot + r_s\right)} + \frac{2r_s^2}{6r_s^2\left(r_\odot + r_s\right)^3} - \frac{2r_s\left(r_\odot + r_s\right)}{6r_s^2\left(r_\odot + r_s\right)^3} \\
& + \frac{r_s^2}{6r_s^2\left(r_\odot + r_s\right)^3} - \frac{\left(r_\odot + r_s\right)^2}{6r_s^2\left(r_\odot + r_s\right)^3} \\
= & \frac{\ln r_\odot}{3r_s^3} + \frac{1}{3\left(r_\odot + r_s\right)^3}\ln\frac{r_s}{r_\odot\left(r_\odot + r_s\right)} - \frac{r_\odot\left(r_\odot + 4r_s\right)}{6r_s^2\left(r_\odot + r_s\right)^3}
\end{aligned}
$$

Calculation of contribution (Vc) to integral (V)

$$
\begin{aligned}
\text{(Vc)} = & -\frac{\ln\left(r - r_\odot\right)}{3\left(r+r_s\right)^3}\bigg|_{r_\odot}^{\infty} - \int_{r_\odot}^{\infty}\mathrm{d}r\left(-\frac{1}{3\left(r+r_s\right)^3}\right)\frac{1}{r - r_\odot} \\
= & -\frac{\ln\left(r_\odot - r\right)}{3\left(r+r_s\right)^3}\bigg|_{r_\odot}^{\infty} + \int_{r_\odot}^{\infty}\mathrm{d}r\frac{1}{3\left(r+r_s\right)^3\left(r - r_\odot\right)} \\
& \text{with } \frac{1}{\left(r+r_s\right)^3\left(r - r_\odot\right)} = -\frac{1}{\left(r_\odot + r_s\right)^3\left(r+r_s\right)} - \frac{1}{\left(r_\odot + r_s\right)^2\left(r+r_s\right)^2} \\
& \qquad - \frac{1}{\left(r_\odot + r_s\right)\left(r+r_s\right)^3} + \frac{1}{\left(r_\odot + r_s\right)^3\left(r - r_\odot\right)} \\
= & -\frac{\ln\left(r - r_\odot\right)}{3\left(r+r_s\right)^3}\bigg|_{r_\odot}^{\infty} - \int_{r_\odot}^{\infty}\mathrm{d}r\frac{1}{3\left(r_\odot + r_s\right)^3\left(r+r_s\right)} - \int_{r_\odot}^{\infty}\mathrm{d}r\frac{1}{3\left(r_\odot + r_s\right)^2\left(r+r_s\right)^2} \\
& - \int_{r_\odot}^{\infty}\mathrm{d}r\frac{1}{3\left(r_\odot + r_s\right)\left(r+r_s\right)^3} + \int_{r_\odot}^{\infty}\mathrm{d}r\frac{1}{3\left(r_\odot + r_s\right)^3\left(r - r_\odot\right)} \qquad \text{(B.30)} \\
= & -\frac{\ln\left(r - r_\odot\right)}{3\left(r+r_s\right)^3}\bigg|_{r_\odot}^{\infty} - \frac{\ln\left(r+r_s\right)}{3\left(r_\odot + r_s\right)^3}\bigg|_{r_\odot}^{\infty} + \frac{1}{3\left(r_\odot + r_s\right)^2\left(r+r_s\right)}\bigg|_{r_\odot}^{\infty} \\
& + \frac{1}{6\left(r_\odot + r_s\right)\left(r+r_s\right)^2}\bigg|_{r_\odot}^{\infty} + \frac{\ln\left(r - r_\odot\right)}{3\left(r_\odot + r_s\right)^3}\bigg|_{r_\odot}^{\infty} \\
= & -\frac{\ln\left(r - r_\odot\right)}{3\left(r+r_s\right)^3}\bigg|_{r=\infty} + \frac{\ln\left(r - r_\odot\right)}{3\left(r+r_s\right)^3}\bigg|_{r=r_\odot} - \frac{\ln r + r_s}{3\left(r_\odot + r_s\right)^3}\bigg|_{r=\infty} + \frac{\ln\left(r_\odot + r_s\right)}{3\left(r_\odot + r_s\right)^3} \\
& + \frac{1}{3\left(r_\odot + r_s\right)^2\left(r+r_s\right)}\bigg|_{r=\infty} - \frac{1}{3\left(r_\odot + r_s\right)^3} + \frac{1}{6\left(r_\odot + r_s\right)\left(r+r_s\right)^2}\bigg|_{r=\infty} \\
& - \frac{1}{6\left(r_\odot + r_s\right)^3} + \frac{\ln\left(r - r_\odot\right)}{3\left(r_\odot + r_s\right)^3}\bigg|_{r=\infty} - \frac{\ln\left(r - r_\odot\right)}{3\left(r_\odot + r_s\right)^3}\bigg|_{r=r_\odot}
\end{aligned}
$$

$$\text{with} \qquad \lim_{r\to\infty} \frac{\ln(r-r_\odot)}{3(r+r_s)^3} = \lim_{r\to\infty} \frac{\frac{1}{r-r_\odot}}{9(r+r_s)^2} = \lim_{r\to\infty} \frac{1}{9(r+r_s)^2(r-r_\odot)} = 0$$

$$\lim_{r\to\infty} \frac{1}{3(r_\odot+r_s)^2(r+r_s)} = 0$$

$$\lim_{r\to\infty} \frac{1}{6(r_\odot+r_s)(r+r_s)^2} = 0$$

$$\left.\frac{\ln(r-r_\odot)}{3(r+r_s)^3}\right|_{r=r_\odot} = \left.\frac{\ln(r-r_\odot)}{3(r_\odot+r_s)^3}\right|_{r=r_\odot}$$

$$\left.\frac{\ln(r+r_s)}{3(r_\odot+r_s)^3}\right|_{r=\infty} = \left.\frac{\ln(r-r_\odot)}{3(r_\odot+r_s)^3}\right|_{r=\infty}$$

$$(\text{Vc}) = \frac{\ln(r_\odot+r_s)}{3(r_\odot+r_s)^3} - \frac{1}{2(r_\odot+r_s)^3}$$

With the results from equations (Va), (Vb), and (Vc) that were derived on the previous pages a solution for integral (V) is calculated.

$$\begin{aligned}(\text{V}) = \frac{1}{r_s}\Bigg\{ & \frac{\ln r_\odot}{3r_s^3} + \frac{1}{3(r_\odot-r_s)^3}\ln\frac{r_\odot}{r_s} + \frac{r_\odot-3r_s}{6r_s^2(r_\odot-r_s)^2} - \frac{\ln r_\odot}{3r_s^3} \\ & - \frac{1}{3(r_\odot+r_s)^3}\ln\frac{r_s}{r_\odot(r_\odot+r_s)} + \frac{r_\odot(r_\odot+4r_s)}{6r_s^2(r_\odot+r_s)^3} - \frac{\ln(r_\odot+r_s)}{3(r_\odot+r_s)^3} + \frac{1}{2(r_\odot+r_s)^3}\Bigg\} \\ = {} & \frac{2r_\odot^3+6r_\odot r_s^2}{3r_s\left(r_\odot^2-r_s^2\right)^3}\ln\frac{r_\odot}{r_s} + \frac{r_\odot\left(r_\odot^2-5r_s^2\right)}{3r_s^3\left(r_\odot^2-r_s^2\right)^2}\end{aligned} \tag{B.31}$$

After calculating the contributions of integrals (I) to (V) to integral $\mathcal{I}$ the final solution for this integral can be derived.

$$\begin{aligned}\mathcal{I} &= \text{I} - \text{II} - \text{III} - \text{IV} - \text{V} \\ &= \frac{\pi^2}{2r_s^4} - \frac{\pi^2}{6r_s^4} - \frac{1}{r_s^4}\ln\frac{r_s}{r_s-r_\odot}\ln\frac{r_s+r_\odot}{r_\odot} + \frac{1}{2r_s^4}\ln^2\frac{r_s+r_\odot}{r_s-r_\odot} + \frac{1}{r_s^4}L_2\left(\frac{r_s}{r_s-r_\odot}\right) \\ &\quad + \frac{1}{r_s^4}L_2\left(\frac{r_\odot}{r_s+r_\odot}\right) - \frac{2r_\odot}{r_s^3\left(r_s^2-r_\odot^2\right)^2}\ln\frac{r_s}{r_\odot} + \frac{2r_\odot}{r_s\left(r_s^2-r_\odot^2\right)^2}\ln\frac{r_\odot}{r_s} + \frac{r_\odot}{r_s^3\left(r_s^2-r_\odot^2\right)} \\ &\quad - \frac{2r_\odot+6r_\odot r_s^2}{3r_s\left(r_\odot^2-r_s^2\right)^3}\ln\frac{r_\odot}{r_s} - \frac{r_\odot\left(r_\odot^2-5r_s^2\right)}{3r_s^3\left(r_\odot^2-r_s^2\right)^2} \\ &= \frac{\pi^2}{3r_s^4} - \frac{1}{r_s^4}\ln\frac{r_s}{r_s-r_\odot}\ln\frac{r_s+r_\odot}{r_\odot} + \frac{1}{2r_s^4}\ln^2\frac{r_s+r_\odot}{r_s-r_\odot} + \frac{1}{r_s^4}L_2\left(\frac{r_s}{r_s-r_\odot}\right) \\ &\quad + \frac{1}{r_s^4}L_2\left(\frac{r_\odot}{r_s+r_\odot}\right) - \frac{2r_\odot}{r_s^3\left(r_s^2-r_\odot^2\right)^2}\ln\frac{r_s}{r_\odot} - \frac{2r_\odot}{r_s\left(r_s^2-r_\odot^2\right)^2}\ln\frac{r_s}{r_\odot} + \frac{r_\odot}{r_s^3\left(r_s^2-r_\odot^2\right)} \\ &\quad - \frac{2r_\odot+6r_\odot r_s^2}{3r_s\left(r_s^2-r_\odot^2\right)^3}\ln\frac{r_s}{r_\odot} - \frac{r_\odot\left(r_\odot^2-5r_s^2\right)}{3r_s^3\left(r_s^2-r_\odot^2\right)^2} \\ &= \frac{\pi^2}{3r_s^4} - \frac{1}{r_s^4}\ln\frac{r_s}{r_s-r_\odot}\ln\frac{r_s+r_\odot}{r_\odot} + \frac{1}{2r_s^4}\ln^2\frac{r_s+r_\odot}{r_s-r_\odot} + \frac{1}{r_s^4}L_2\left(\frac{r_s}{r_s-r_\odot}\right) \\ &\quad + \frac{1}{r_s^4}L_2\left(\frac{r_\odot}{r_s+r_\odot}\right) - \frac{2r_\odot\left(3r_\odot^4-8r_\odot^2r_s^2-9r_s^4\right)}{3r_s^3\left(r_s^2-r_\odot^2\right)^3}\ln\frac{r_s}{r_\odot} + \frac{4r_\odot\left(2r_s^2-r_\odot^2\right)}{3r_s^2\left(r_s^2-r_\odot^2\right)^2}\end{aligned} \tag{B.32}$$

$$\mathcal{I} = \frac{1}{r_s^4}\left\{\frac{\pi^2}{3} - \ln\frac{r_s}{r_s - r_\odot}\ln\frac{r_s + r_\odot}{r_\odot} + \frac{1}{2}\ln^2\frac{r_s + r_\odot}{r_s - r_\odot} + L_2\left(\frac{r_s}{r_s - r_\odot}\right) + L_2\left(\frac{r_\odot}{r_s + r_\odot}\right)\right.$$
$$\left. - \frac{2r_\odot r_s\left(3r_\odot^4 - 8r_\odot^2 r_s^2 - 9r_s^4\right)}{3\left(r_s^2 - r_\odot^2\right)^3}\ln\frac{r_s}{r_\odot} + \frac{4r_\odot r_s^2\left(2r_s^2 - r_\odot^2\right)}{3\left(r_s^2 - r_\odot^2\right)^2}\right\}$$

4. For numerical simulations it is more convenient to simulate the mass of a substructure than its tidal radius. Therefore it is necessary to normalise the subclump density profile integrating the subclump profile over the volume of the subclump.

$$\begin{aligned}
M_{\rm Cl} &= \int \mathrm{d}^3\vec{d}\,\rho_X(d,r) \\
&\quad \text{with } \rho_X(d,r) = n_H(r) M_X \frac{d_t\left(d_t + d_s\right)^2}{d\left(d + d_s\right)^2} \\
&= \int \mathrm{d}^3\vec{d}\, n_H(r) M_X \frac{d_t\left(d_t + d_s\right)^2}{d\left(d + d_s\right)^2} \\
&= 4\pi n_H(r) M_X d_t\left(d_t + d_s\right)^2 \int_0^{d_t} \mathrm{d}d\,\frac{d}{\left(d + d_s\right)^2} \\
&\quad \text{with } \int \mathrm{d}d\,\frac{d}{\left(d + d_s\right)^2} = \frac{d_s}{d + d_s} + \ln\left(d + d_s\right) \\
&= 4\pi n_H(r) M_X d_t\left(d_t + d_s\right)^2\left(\ln\frac{d_t + d_s}{d_s} - \frac{d_t}{d_t + d_s}\right) \\
\Rightarrow d_t &= d_t(r, M_{\rm cl}) \quad \text{,solved numerically}
\end{aligned} \tag{B.33}$$

The resulting equation cannot be solved for the tidal radius and a numerical solution has to be computed. Instead an approximate solution for the core radius can be found by assuming that the tidal radius is in the range between $5d_s \leq d_t \leq 50d_s$ which is a reasonable assumption based on the relation between these parameters for Globular Clusters.

$$\begin{aligned}
M_{\rm Cl} &\approx 4\pi n_H(r) M_X d_t^3\left(\ln\frac{d_t + d_s}{d_s} - \frac{d_t}{d_t + d_s}\right) \\
&\quad \text{with } \left(\ln\frac{d_t + d_s}{d_s} - \frac{d_t}{d_t + d_s}\right) \approx 2^{+1.0}_{-1.0} \\
&\approx 8\pi n_H(r) M_X d_t^3 \\
\Rightarrow d_t &= d_t(r, M_{\rm Cl}) \approx \sqrt[3]{\frac{M_{\rm Cl}}{8\pi n_H(r) M_X}}
\end{aligned} \tag{B.34}$$

5. By integrating the square of the subclump number distribution over the volume of the subclump the annihilation rate inside a subclump can be derived.

$$\begin{aligned}
\mathcal{R}\left(r, M_{\rm cl}\right) &= \langle\sigma v\rangle \int \mathrm{d}^3\vec{d}\, n_X^2(d,r) \\
&\quad \text{with } n_X(d,r) = n_H(r)\frac{d_t\left(d_t + d_s\right)^2}{d\left(d + d_s\right)^2} \\
&= \langle\sigma v\rangle \int \mathrm{d}^3\vec{r}\, n_H^2(r)\frac{d_t^2\left(d_t + d_s\right)^4}{d^2\left(d + d_s\right)^4}
\end{aligned} \tag{B.35}$$

$$
\begin{aligned}
\mathcal{R}\left(r, M_{\mathrm{cl}}\right) &= 4\pi\langle\sigma v\rangle n_H^2(r) d_t^2 \left(d_t + d_s\right)^4 \int_0^{d_t} \mathrm{d}d \, \frac{1}{\left(d + d_s\right)^4} \\
&= \frac{4}{3}\pi\langle\sigma v\rangle n_H^2(r) d_t^2 \left(d_t + d_s\right)^4 \left\{ \frac{1}{d_s^3} - \frac{1}{\left(d_t + d_s\right)^3} \right\} \\
&= \frac{4}{3}\pi\langle\sigma v\rangle n_H^2(r) d_t^2 \left(d_t + d_s\right) \left\{ \frac{\left(d_t + d_s\right)^3}{d_s^3} - 1 \right\} \\
&\quad \text{,where } \; d_t = d_t\left(r, M_{\mathrm{Cl}}\right)
\end{aligned}
$$

For an exact solution the tidal radius depends on the distance from the Galactic Center as well as on the subclump mass. Instead an approximate solution is found by assuming that $d_t \gg d_s$.

$$
\begin{aligned}
\mathcal{R}(r, M_{\mathrm{cl}}) &= \frac{4}{3}\pi\langle\sigma v\rangle n_H^2(r) d_t^2 \left(d_t + d_s\right) \left\{ \frac{\left(d_t + d_s\right)^3}{d_s^3} - 1 \right\} \\
&\quad \text{with } \; d_t^2 \left(d_t + d_s\right) \left\{ \frac{\left(d_t + d_s\right)^3}{d_s^3} - 1 \right\} \approx \frac{d_t^6}{d_s^3} \\
&\approx \frac{4}{3}\pi\langle\sigma v\rangle n_H^2(r) \frac{d_t^6}{d_s^3} \\
&\quad \text{with } \; d_t = d_t(r, M_{\mathrm{cl}}) \sqrt[3]{\frac{M_{\mathrm{Cl}}}{8\pi n_H(r) M_X}} \\
&\approx \frac{1}{48\pi}\langle\sigma v\rangle \frac{M_{\mathrm{Cl}}^2}{M_X^2 d_s^3}
\end{aligned}
\tag{B.36}
$$

6. Before the annihilation flux from the subclumps can be calculated the subclump distribution in the galaxy has to be normalised. This distribution is independent of the exact shape of the shape of the subclumps and the results of this calculation are valid for all profiles. For this reason this calculation is omitted in the calculations for the other profiles.

$$
\begin{aligned}
\xi M_H &= \int \mathrm{d}^3\vec{r} \int \mathrm{d}M_{\mathrm{cl}} \, M_{\mathrm{cl}} n_{\mathrm{cl}}(r, M_{\mathrm{cl}}) \\
&\quad \text{with } \; n_{\mathrm{cl}}(r, M_{\mathrm{cl}}) = n_{\mathrm{cl}}^0 \left(\frac{M_H}{M_{\mathrm{cl}}}\right)^{\alpha} \frac{{R_c^{\mathrm{cl}}}^3}{\left({R_c^{\mathrm{cl}}}^2 + r^2\right)^{\frac{3}{2}}} \\
&= \int \mathrm{d}^3\vec{r} \int \mathrm{d}M_{\mathrm{cl}} \, M_{\mathrm{cl}} n_{\mathrm{cl}}^0 \left(\frac{M_H}{M_{\mathrm{cl}}}\right)^{\alpha} \frac{{R_c^{\mathrm{cl}}}^3}{\left({R_c^{\mathrm{cl}}}^2 + r^2\right)^{\frac{3}{2}}} \\
&= 4\pi n_{\mathrm{cl}}^0 M_H^{\alpha} {R_c^{\mathrm{cl}}}^3 \int_0^{r_t} \mathrm{d}r \int_0^{\eta M_H} \mathrm{d}M_{\mathrm{cl}} \, M_{\mathrm{cl}}^{1-\alpha} \frac{r^2}{\left({R_c^{\mathrm{cl}}}^2 + r^2\right)^{\frac{3}{2}}} \\
&= 4\pi \frac{n_{\mathrm{cl}}^0 M_H^2 \eta^{2-\alpha} {R_c^{\mathrm{cl}}}^3}{2 - \alpha} \int_0^{r_t} \mathrm{d}r \, \frac{r^2}{\left({R_c^{\mathrm{cl}}}^2 + r^2\right)^{\frac{3}{2}}} \\
&\quad \text{with } \; \int \mathrm{d}r \, \frac{r^2}{\sqrt{{R_c^{\mathrm{cl}}}^2 + r^2}} = -\frac{r}{\sqrt{{R_c^{\mathrm{cl}}}^2 + r^2}} + \ln\left(r + \sqrt{{R_c^{\mathrm{cl}}}^2 + r^2}\right)
\end{aligned}
\tag{B.37}
$$

$$\xi M_H = 4\pi \frac{n_{\rm cl}^0 M_H^2 \eta^{2-\alpha} {R_c^{\rm cl}}^3}{2-\alpha} \left\{ \ln\left(\frac{r_t + \sqrt{{R_c^{\rm cl}}^2 + r_t^2}}{R_c^{\rm cl}} \right) - \frac{r_t}{\sqrt{{R_c^{\rm cl}}^2 + r_t^2}} \right\}$$

$$\Rightarrow n_{\rm cl}^0 = \frac{\xi\,(2-\alpha)}{4\pi M_H \eta^{2-\alpha} {R_c^{\rm cl}}^3 \left\{ \ln\left(\frac{r_t + \sqrt{{R_c^{\rm cl}}^2 + r_t^2}}{R_c^{\rm cl}} \right) - \frac{r_t}{\sqrt{{R_c^{\rm cl}}^2 + r_t^2}} \right\}}$$

By using the fact that the tidal radius is much bigger than the scale radius of the subclump distribution in the galaxy, $r_t \gg R_c^{\rm cl}$, the result for the normalisation constant is simplified.

$$\begin{aligned} n_{\rm cl}^0 &= \frac{\xi\,(2-\alpha)}{4\pi M_H \eta^{2-\alpha} {R_c^{\rm cl}}^3 \left\{ \ln\left(\frac{r_t + \sqrt{{R_c^{\rm cl}}^2 + r_t^2}}{R_c^{\rm cl}} \right) - \frac{r_t}{\sqrt{{R_c^{\rm cl}}^2 + r_t^2}} \right\}} \\ &\quad \text{with } \sqrt{{R_c^{\rm cl}}^2 + r_t^2} \approx r_t \\ &\approx \frac{\xi\,(2-\alpha)}{4\pi M_H \eta^{2-\alpha} {R_c^{\rm cl}}^3 \left\{ \ln \frac{2r_t}{R_c^{\rm cl}} - 1 \right\}} \end{aligned} \tag{B.38}$$

7. Finally, the annihilation flux from the clumped DM component is calculated.

$$\begin{aligned} \mathcal{F} &= \frac{{\rm d}N}{{\rm d}E} \int {\rm d}^3\vec{r} \frac{1}{2\pi \left|\vec{r} - \vec{r_\odot}\right|^2} \int {\rm d}M_{\rm cl} n_{\rm cl}(r, M_{\rm cl}) \mathcal{R}(r, M_{\rm cl}) \\ &\quad \text{with} \quad \frac{1}{|\vec{r} - \vec{r}_\odot|^2} = \frac{1}{r^2 + r_\odot^2 - 2 r r_\odot \cos\theta} \\ &\qquad n_{\rm cl}(r, M_{\rm cl}) = n_{\rm cl}^0 \left(\frac{M_H}{M_{\rm cl}} \right)^\alpha \frac{{R_c^{\rm cl}}^3}{\left({R_c^{\rm cl}}^2 + r^2 \right)^{\frac{3}{2}}} \\ &\qquad \mathcal{R}(r, M_{\rm cl}) = \frac{4\pi}{3} \langle\sigma v\rangle n_H^2(r) d_t^2 \,(d_t + d_s) \left\{ \frac{(d_t + d_s)^3}{d_s^3} - 1 \right\} \\ &= \frac{1}{2\pi} \frac{{\rm d}N}{{\rm d}E} \int {\rm d}^3\vec{r} \frac{1}{r^2 + r_\odot^2 - 2 r r_\odot \cos\theta} \int {\rm d}M_{\rm cl}\, n_{\rm cl}^0 \left(\frac{M_H}{M_{\rm cl}} \right)^\alpha \frac{{R_c^{\rm cl}}^3}{\left({R_c^{\rm cl}}^2 + r^2 \right)^{\frac{3}{2}}} \\ &\quad \times \frac{4\pi}{3} \langle\sigma v\rangle n_H^2(r) d_t^2 \,(d_t + d_s) \left\{ \frac{(d_t + d_s)^3}{d_s^3} - 1 \right\} \\ &= \frac{2}{3} \frac{{\rm d}N}{{\rm d}E} \langle\sigma v\rangle n_{\rm cl}^0 M_H^\alpha {R_c^{\rm cl}}^3 \int {\rm d}^3\vec{r} \frac{n_H^2(r)}{\left(r^2 + r_\odot^2 - 2 r r_\odot \cos\theta \right) \left({R_c^{\rm cl}}^2 + r^2 \right)^{\frac{3}{2}}} \\ &\quad \times \int {\rm d}M_{\rm cl}\, M_{\rm cl}^{-\alpha} d_t^2 \,(d_t + d_s) \left\{ \frac{(d_t + d_s)^3}{d_s^3} - 1 \right\} \\ &= \frac{4\pi}{3} \frac{{\rm d}N}{{\rm d}E} \langle\sigma v\rangle n_{\rm cl}^0 M_H^\alpha {R_c^{\rm cl}}^3 \int_0^{r_t} {\rm d}r \int_0^\pi {\rm d}\theta \frac{n_H^2(r) r^2 \sin\theta}{\left(r^2 + r_\odot^2 - 2 r r_\odot \cos\theta \right) \left({R_c^{\rm cl}}^2 + r^2 \right)^{\frac{3}{2}}} \\ &\quad \times \int_0^{\eta M_H} {\rm d}M_{\rm cl}\, M_{\rm cl}^{-\alpha} d_t^2 \,(d_t + d_s) \left\{ \frac{(d_t + d_s)^3}{d_s^3} - 1 \right\} \end{aligned} \tag{B.39}$$

$$
\begin{aligned}
\mathcal{F} &= \frac{4\pi}{3}\frac{\mathrm{d}N}{\mathrm{d}E}\langle\sigma v\rangle n_{\mathrm{cl}}^0 M_H^\alpha {R_c^{\mathrm{cl}}}^3 \int_0^{r_t}\mathrm{d}r\int_{-1}^{1}\mathrm{d}x\,\frac{n_H^2(r)r^2}{\left(r^2+r_\odot^2-2rr_\odot x\right)\left({R_c^{\mathrm{cl}}}^2+r^2\right)^{\frac{3}{2}}} \\
&\quad\times\int_0^{\eta M_H}\mathrm{d}M_{\mathrm{cl}}\,M_{\mathrm{cl}}^{-\alpha}d_t^2\left(d_t+d_s\right)\left\{\frac{\left(d_t+d_s\right)^3}{d_s^3}-1\right\} \\
&\quad\text{with }\int_{-1}^{1}\mathrm{d}x\,\frac{1}{r^2+r_\odot^2-2rr_\odot x}=\frac{1}{rr_\odot}\ln\frac{r+r_\odot}{|r-r_\odot|} \\
&= \frac{4\pi}{3}\frac{\mathrm{d}N}{\mathrm{d}E}\langle\sigma v\rangle n_{\mathrm{cl}}^0 M_H^\alpha \frac{{R_c^{\mathrm{cl}}}^3}{r_\odot}\int_0^{r_t}\mathrm{d}r\,\frac{n_H^2(r)r}{\left({R_c^{\mathrm{cl}}}^2+r^2\right)^{\frac{3}{2}}}\ln\frac{r+r_\odot}{|r-r_\odot|} \\
&\quad\times\int_0^{\eta M_H}\mathrm{d}M_{\mathrm{cl}}\,M_{\mathrm{cl}}^{-\alpha}d_t^2\left(d_t+d_s\right)\left\{\frac{\left(d_t+d_s\right)^3}{d_s^3}-1\right\} \\
&\quad\text{with }\ n_H(r)=\frac{N_0 r_s^3}{\left(r+r_s\right)^2} \\
&= \frac{4\pi}{3}\frac{\mathrm{d}N}{\mathrm{d}E}\langle\sigma v\rangle N_0^2 n_{\mathrm{cl}}^0 M_H^\alpha \frac{r_s^6{R_c^{\mathrm{cl}}}^3}{r_\odot}\int_0^{r_t}\mathrm{d}r\,\frac{1}{r\left(r+r_s\right)^4\left({R_c^{\mathrm{cl}}}^2+r^2\right)^{\frac{3}{2}}}\ln\frac{r+r_\odot}{|r-r_\odot|} \\
&\quad\times\int_0^{\eta M_H}\mathrm{d}M_{\mathrm{cl}}\,M_{\mathrm{cl}}^{-\alpha}d_t^2\left(d_t+d_s\right)\left\{\frac{\left(d_t+d_s\right)^3}{d_s^3}-1\right\} \\
&\quad,\text{where }\ d_t=d_t\left(r,M_{\mathrm{Cl}}\right)
\end{aligned}
$$

Neither the radial nor the mass integral can be solved exactly. Instead an approximated solution can be found by utilising the previously made assumptions $d_t \gg d_s$, $r_t \gg r_\odot$, and $r_t \gg R_c^{\mathrm{cl}}$.

$$
\begin{aligned}
\mathcal{F} &= \frac{4\pi}{3}\frac{\mathrm{d}N}{\mathrm{d}E}\langle\sigma v\rangle n_{\mathrm{cl}}^0 M_H^\alpha \frac{{R_c^{\mathrm{cl}}}^3}{r_\odot}\int_0^{r_t}\mathrm{d}r\,\frac{n_H^2(r)r}{\left({R_c^{\mathrm{cl}}}^2+r^2\right)^{\frac{3}{2}}}\ln\frac{r+r_\odot}{|r-r_\odot|} \\
&\quad\times\int_0^{\eta M_H}\mathrm{d}M_{\mathrm{cl}}\,M_{\mathrm{cl}}^{-\alpha}d_t^2\left(d_t+d_s\right)\left\{\frac{\left(d_t+d_s\right)^3}{d_s^3}-1\right\} \\
&\quad\text{with }\ d_t^2\left(d_t+d_s\right)\left\{\frac{\left(d_t+d_s\right)^3}{d_s^3}-1\right\}\approx\frac{d_t^6}{d_s^3} \\
&= \frac{4\pi}{3}\frac{\mathrm{d}N}{\mathrm{d}E}\langle\sigma v\rangle n_{\mathrm{cl}}^0 M_H^\alpha \frac{{R_c^{\mathrm{cl}}}^3}{r_\odot d_s^3}\int_0^{r_t}\mathrm{d}r\,\frac{n_H^2(r)r}{\left({R_c^{\mathrm{cl}}}^2+r^2\right)^{\frac{3}{2}}}\ln\frac{r+r_\odot}{|r-r_\odot|}\int_0^{\eta M_H}\mathrm{d}M_{\mathrm{cl}}\,M_{\mathrm{cl}}^{-\alpha}d_t^6 \qquad \text{(B.40)} \\
&\quad\text{with }\ d_t=d_t(r,M_{\mathrm{Cl}})\approx\sqrt[3]{\frac{M_{\mathrm{Cl}}}{8\pi n_H(r)M_X}} \\
&= \frac{1}{48\pi}\frac{\mathrm{d}N}{\mathrm{d}E}\langle\sigma v\rangle n_{\mathrm{cl}}^0 \frac{M_H^\alpha}{M_X^2}\frac{{R_c^{\mathrm{cl}}}^3}{r_\odot d_s^3}\int_0^{r_t}\mathrm{d}r\,\frac{r}{\left({R_c^{\mathrm{cl}}}^2+r^2\right)^{\frac{3}{2}}}\ln\frac{r+r_\odot}{|r-r_\odot|}\int_0^{\eta M_H}\mathrm{d}M_{\mathrm{cl}}\,M_{\mathrm{cl}}^{2-\alpha} \\
&= \frac{1}{48\pi}\frac{\mathrm{d}N}{\mathrm{d}E}\langle\sigma v\rangle n_{\mathrm{cl}}^0 \frac{\eta^{3-\alpha}M_H^3}{(3-\alpha)M_X^2}\frac{{R_c^{\mathrm{cl}}}^3}{r_\odot d_s^3}\int_0^{r_t}\mathrm{d}r\,\frac{r}{\left({R_c^{\mathrm{cl}}}^2+r^2\right)^{\frac{3}{2}}}\ln\frac{r+r_\odot}{|r-r_\odot|}
\end{aligned}
$$

$$\text{with} \int_0^{r_t} \mathrm{d}r \, \frac{r}{\left(R_c^{\mathrm{cl}\,2} + r^2\right)^{\frac{3}{2}}} \ln \frac{r + r_\odot}{|r - r_\odot|}$$

$$= \frac{1}{\sqrt{r_\odot^2 + R_c^{\mathrm{cl}\,2}}} \ln \left(1 + \frac{2 r_\odot r_t}{\sqrt{R_c^{\mathrm{cl}\,2} + r_\odot^2} \sqrt{R_c^{\mathrm{cl}\,2} + r_t^2} + R_c^{\mathrm{cl}\,2} - r_\odot r_t} \right)$$

$$\mathcal{F} = \frac{1}{48\pi} \frac{\mathrm{d}N}{\mathrm{d}E} \langle \sigma v \rangle n_{\mathrm{cl}}^0 \frac{\eta^{3-\alpha} M_H^3}{(3-\alpha)\, M_X^2} \frac{R_c^{\mathrm{cl}\,3}}{r_\odot d_s^3 \sqrt{r_\odot^2 + R_c^{\mathrm{cl}\,2}}}$$

$$\times \ln \left(1 + \frac{2 r_\odot r_t}{\sqrt{R_c^{\mathrm{cl}\,2} + r_\odot^2} \sqrt{R_c^{\mathrm{cl}\,2} + r_t^2} + R_c^{\mathrm{cl}\,2} - r_\odot r_t} \right)$$

$$\text{with } \ln \left(1 + \frac{2 r_\odot r_t}{\sqrt{R_c^{\mathrm{cl}\,2} + r_\odot^2} \sqrt{R_c^{\mathrm{cl}\,2} + r_t^2} + R_c^{\mathrm{cl}\,2} - r_\odot r_t} \right) \approx \ln \left(1 + \frac{2 r_\odot}{\sqrt{R_c^{\mathrm{cl}\,2} + r_\odot^2} - r_\odot} \right)$$

$$= \frac{1}{48\pi} \frac{\mathrm{d}N}{\mathrm{d}E} \langle \sigma v \rangle n_{\mathrm{cl}}^0 \frac{\eta^{3-\alpha} M_H^3}{(3-\alpha)\, M_X^2} \frac{R_c^{\mathrm{cl}\,3}}{r_\odot d_s^3 \sqrt{r_\odot^2 + R_c^{\mathrm{cl}\,2}}} \ln \left(1 + \frac{2 r_\odot}{\sqrt{R_c^{\mathrm{cl}\,2} + r_\odot^2} - r_\odot} \right)$$

7.1 Calculation of the integral used in the calculation

$$\mathcal{I} = \int_0^{r_t} \mathrm{d}r \frac{r}{\left(R_c^{\mathrm{cl}\,2} + r^2\right)^{\frac{3}{2}}} \ln \frac{r + r_\odot}{|r - r_\odot|} \tag{B.41}$$

$$= \underbrace{\int_0^{r_t} \mathrm{d}r \frac{r \ln (r + r_\odot)}{\left(R_c^{\mathrm{cl}\,2} + r^2\right)^{\frac{3}{2}}}}_{\text{(I)}} - \underbrace{\int_0^{r_\odot} \mathrm{d}r \frac{r \ln (r_\odot - r)}{\left(R_c^{\mathrm{cl}\,2} + r^2\right)^{\frac{3}{2}}}}_{\text{(II)}} - \underbrace{\int_{r_\odot}^{r_t} \mathrm{d}r \frac{r \ln (r - r_\odot)}{\left(R_c^{\mathrm{cl}\,2} + r^2\right)^{\frac{3}{2}}}}_{\text{(III)}}$$

Calculation of contribution (I) to integral $\mathcal{I}$

$$(I) = \int_0^{r_t} \mathrm{d}r \frac{r \ln (r + r_\odot)}{\left(R_c^{\mathrm{cl}\,2} + r^2\right)^{\frac{3}{2}}}$$

$$= -\frac{\ln (r + r_\odot)}{\sqrt{R_c^{\mathrm{cl}\,2} + r^2}} \Bigg|_0^{r_t} - \int_0^{r_t} \mathrm{d}r \left(-\frac{1}{\sqrt{R_c^{\mathrm{cl}\,2} + r^2}} \right) \frac{1}{r + r_\odot}$$

$$= -\frac{\ln (r + r_\odot)}{\sqrt{R_c^{\mathrm{cl}\,2} + r^2}} \Bigg|_0^{r_t} + \int_0^{r_t} \mathrm{d}r \frac{1}{(r + r_\odot) \sqrt{R_c^{\mathrm{cl}\,2} + r^2}} \tag{B.42}$$

$$\text{with } t = \frac{1}{r + r_\odot} \Rightarrow \frac{\mathrm{d}t}{\mathrm{d}r} = -\frac{1}{(r + r_\odot)^2} \Rightarrow \mathrm{d}r = -\frac{\mathrm{d}t}{t^2}$$

$$= -\frac{\ln (r + r_\odot)}{\sqrt{R_c^{\mathrm{cl}\,2} + r^2}} \Bigg|_0^{r_t} - \int_{\frac{1}{r_\odot}}^{\frac{1}{r_t + r_\odot}} \mathrm{d}t \frac{1}{t \sqrt{R_c^{\mathrm{cl}\,2} + r^2}}$$

$$\text{with } r + r_\odot = \frac{1}{t} \Rightarrow r = \frac{1}{t} - r_\odot$$

$$
\begin{aligned}
(I) &= -\frac{\ln\left(r+r_\odot\right)}{\sqrt{{R_c^{\mathrm{cl}}}^2+r^2}}\Bigg|_0^{r_t} - \int_{\frac{1}{r_\odot}}^{\frac{1}{r_t+r_\odot}} \mathrm{d}t \frac{1}{t\sqrt{{R_c^{\mathrm{cl}}}^2+\frac{1}{t^2}-\frac{2r_\odot}{t}+r_\odot^2}} \\
&= -\frac{\ln\left(r+r_\odot\right)}{\sqrt{{R_c^{\mathrm{cl}}}^2+r^2}}\Bigg|_0^{r_t} - \int_{\frac{1}{r_\odot}}^{\frac{1}{r_t+r_\odot}} \mathrm{d}t \frac{1}{\sqrt{\left({R_c^{\mathrm{cl}}}^2+r_\odot^2\right)t^2-2r_\odot t+1}} \\
&\quad \text{with } \int \mathrm{d}t \frac{1}{\sqrt{at^2+bt+c}} = \frac{1}{\sqrt{a}}\ln\left(2\sqrt{a}\sqrt{at^2+bt+c}+2at+b\right) \\
&= -\frac{\ln\left(2\sqrt{\left({R_c^{\mathrm{cl}}}^2+r_\odot^2\right)}\sqrt{\left({R_c^{\mathrm{cl}}}^2+r_\odot^2\right)t^2-2r_\odot t+1}+2\left({R_c^{\mathrm{cl}}}^2+r_\odot^2\right)t-2r_\odot\right)}{\sqrt{\left({R_c^{\mathrm{cl}}}^2+r_\odot^2\right)}}\Bigg|_{\frac{1}{r_\odot}}^{\frac{1}{r_t+r_\odot}} \\
&\quad - \frac{\ln\left(r+r_\odot\right)}{\sqrt{{R_c^{\mathrm{cl}}}^2+r^2}}\Bigg|_0^{r_t} \\
&= -\frac{\ln\left(r_t+r_\odot\right)}{\sqrt{{R_c^{\mathrm{cl}}}^2+r_t^2}} + \frac{\ln r_\odot}{R_c^{\mathrm{cl}}} \\
&\quad - \frac{\ln\left(2\sqrt{\left({R_c^{\mathrm{cl}}}^2+r_\odot^2\right)}\sqrt{\frac{{R_c^{\mathrm{cl}}}^2+r_\odot^2}{\left(r_t+r_\odot\right)^2}-\frac{2r_\odot}{r_t+r_\odot}+1}+\frac{2\left({R_c^{\mathrm{cl}}}^2+r_\odot^2\right)}{r_t+r_\odot}-2r_\odot\right)}{\sqrt{\left({R_c^{\mathrm{cl}}}^2+r_\odot^2\right)}} \\
&\quad + \frac{\ln\left(2\sqrt{\left({R_c^{\mathrm{cl}}}^2+r_\odot^2\right)}\sqrt{\frac{{R_c^{\mathrm{cl}}}^2+r_\odot^2}{r_\odot^2}-\frac{2r_\odot}{r_\odot}+1}+\frac{2\left({R_c^{\mathrm{cl}}}^2+r_\odot^2\right)}{r_\odot}-2r_\odot\right)}{\sqrt{\left({R_c^{\mathrm{cl}}}^2+r_\odot^2\right)}} \\
&= -\frac{\ln\left(r_t+r_\odot\right)}{\sqrt{{R_c^{\mathrm{cl}}}^2+r_t^2}} + \frac{\ln r_\odot}{R_c^{\mathrm{cl}}} - \frac{\ln\left(2\frac{\sqrt{{R_c^{\mathrm{cl}}}^2+r_\odot^2}\sqrt{{R_c^{\mathrm{cl}}}^2+r_t^2}+\left({R_c^{\mathrm{cl}}}^2-r_\odot r_t\right)}{r_t+r_\odot}\right)}{\sqrt{{R_c^{\mathrm{cl}}}^2+r_\odot^2}} \\
&\quad + \frac{\ln\left(2\sqrt{{R_c^{\mathrm{cl}}}^2+r_\odot^2}\frac{R_c^{\mathrm{cl}}}{r_\odot}+\frac{2{R_c^{\mathrm{cl}}}^2}{r_\odot}\right)}{\sqrt{{R_c^{\mathrm{cl}}}^2+r_\odot^2}}
\end{aligned}
$$

Calculation of contribution (II) to integral $\mathcal{I}$

$$
\begin{aligned}
(II) &= \int_0^{r_\odot} \mathrm{d}r \frac{r\ln\left(r_\odot-r\right)}{\left({R_c^{\mathrm{cl}}}^2+r^2\right)^{\frac{3}{2}}} \\
&= -\frac{\ln\left(r_\odot-r\right)}{\sqrt{{R_c^{\mathrm{cl}}}^2+r^2}}\Bigg|_0^{r_\odot} - \int_0^{r_\odot} \mathrm{d}r \left(-\frac{1}{\sqrt{{R_c^{\mathrm{cl}}}^2+r^2}}\right)\left(-\frac{1}{r_\odot-r}\right) \qquad \text{(B.43)} \\
&= -\frac{\ln\left(r_\odot-r\right)}{\sqrt{{R_c^{\mathrm{cl}}}^2+r^2}}\Bigg|_0^{r_\odot} - \int_0^{r_\odot} \mathrm{d}r \frac{1}{\left(r_\odot-r\right)\sqrt{{R_c^{\mathrm{cl}}}^2+r^2}}
\end{aligned}
$$

$$\text{with } t = \frac{1}{r_\odot - r} \Rightarrow \frac{\mathrm{d}t}{\mathrm{d}r} = \frac{1}{(r_\odot - r)^2} \Rightarrow \mathrm{d}r = \frac{\mathrm{d}t}{t^2}$$

$$(II) = -\frac{\ln(r_\odot - r)}{\sqrt{{R_c^{\mathrm{cl}}}^2 + r^2}}\Bigg|_0^{r_\odot} - \int_{\frac{1}{r_\odot}}^{\infty} \mathrm{d}t \frac{1}{t\sqrt{{R_c^{\mathrm{cl}}}^2 + r^2}}$$

$$\text{with } r_\odot - r = \frac{1}{t} \Rightarrow r = r_\odot - \frac{1}{t}$$

$$= -\frac{\ln(r_\odot - r)}{\sqrt{{R_c^{\mathrm{cl}}}^2 + r^2}}\Bigg|_0^{r_\odot} - \int_{\frac{1}{r_\odot}}^{\infty} \mathrm{d}t \frac{1}{t\sqrt{{R_c^{\mathrm{cl}}}^2 + \frac{1}{t^2} - \frac{2r_\odot}{t} + r_\odot^2}}$$

$$= -\frac{\ln(r_\odot - r)}{\sqrt{{R_c^{\mathrm{cl}}}^2 + r^2}}\Bigg|_0^{r_\odot} - \int_{\frac{1}{r_\odot}}^{\infty} \mathrm{d}t \frac{1}{\sqrt{\left({R_c^{\mathrm{cl}}}^2 + r_\odot^2\right)t^2 - 2r_\odot t + 1}}$$

$$\text{with } \int \mathrm{d}t \frac{1}{\sqrt{at^2 + bt + c}} = \frac{1}{\sqrt{a}} \ln\left(2\sqrt{a}\sqrt{at^2 + bt + c} + 2at + b\right)$$

$$= -\frac{\ln\left(2\sqrt{\left({R_c^{\mathrm{cl}}}^2 + r_\odot^2\right)}\sqrt{\left({R_c^{\mathrm{cl}}}^2 + r_\odot^2\right)t^2 - 2r_\odot t + 1} + 2\left({R_c^{\mathrm{cl}}}^2 + r_\odot^2\right)t - 2r_\odot\right)}{\sqrt{\left({R_c^{\mathrm{cl}}}^2 + r_\odot^2\right)}}\Bigg|_{\frac{1}{r_\odot}}^{\infty}$$

$$- \frac{\ln(r_\odot - r)}{\sqrt{{R_c^{\mathrm{cl}}}^2 + r^2}}\Bigg|_0^{r_\odot}$$

$$= -\frac{\ln(r_\odot - r)}{\sqrt{{R_c^{\mathrm{cl}}}^2 + r^2}}\Bigg|_{r=r_\odot} + \frac{\ln r_\odot}{R_c^{\mathrm{cl}}}$$

$$- \frac{\ln\left(2\sqrt{\left({R_c^{\mathrm{cl}}}^2 + r_\odot^2\right)}\sqrt{\left({R_c^{\mathrm{cl}}}^2 + r_\odot^2\right)t^2 - 2r_\odot t + 1} + 2\left({R_c^{\mathrm{cl}}}^2 + r_\odot^2\right)t - 2r_\odot\right)}{\sqrt{\left({R_c^{\mathrm{cl}}}^2 + r_\odot^2\right)}}\Bigg|_{t=\infty}$$

$$+ \frac{\ln\left(2\sqrt{\left({R_c^{\mathrm{cl}}}^2 + r_\odot^2\right)}\sqrt{\frac{{R_c^{\mathrm{cl}}}^2 + r_\odot^2}{r_\odot^2} - \frac{2r_\odot}{r_\odot} + 1} + \frac{2\left({R_c^{\mathrm{cl}}}^2 + r_\odot^2\right)}{r_\odot} - 2r_\odot\right)}{\sqrt{\left({R_c^{\mathrm{cl}}}^2 + r_\odot^2\right)}}$$

$$= -\frac{\ln(r_\odot - r)}{\sqrt{{R_c^{\mathrm{cl}}}^2 + r^2}}\Bigg|_{r=r_\odot} + \frac{\ln r_\odot}{R_c^{\mathrm{cl}}} + \frac{\ln\left(2\sqrt{{R_c^{\mathrm{cl}}}^2 + r_\odot^2}\frac{R_c^{\mathrm{cl}}}{r_\odot} + \frac{2{R_c^{\mathrm{cl}}}^2}{r_\odot}\right)}{\sqrt{{R_c^{\mathrm{cl}}}^2 + r_\odot^2}}$$

$$- \frac{\ln\left(2\sqrt{\left({R_c^{\mathrm{cl}}}^2 + r_\odot^2\right)}\sqrt{\left({R_c^{\mathrm{cl}}}^2 + r_\odot^2\right)t^2 - 2r_\odot t + 1} + 2\left({R_c^{\mathrm{cl}}}^2 + r_\odot^2\right)t - 2r_\odot\right)}{\sqrt{\left({R_c^{\mathrm{cl}}}^2 + r_\odot^2\right)}}\Bigg|_{t=\infty}$$

Calculation of contribution (III) to integral $\mathcal{I}$

$$
\begin{aligned}
(III) &= \int_{r_\odot}^{r_t} \mathrm{d}r \frac{r \ln\left(r - r_\odot\right)}{\left(R_c^{\mathrm{cl}\,2} + r^2\right)^{\frac{3}{2}}} \\
&= -\frac{\ln\left(r - r_\odot\right)}{\sqrt{R_c^{\mathrm{cl}\,2} + r^2}}\Bigg|_{r_\odot}^{r_t} - \int_{r_\odot}^{r_t} \mathrm{d}r \left(-\frac{1}{\sqrt{R_c^{\mathrm{cl}\,2} + r^2}}\right) \frac{1}{r - r_\odot} \\
&= -\frac{\ln\left(r - r_\odot\right)}{\sqrt{R_c^{\mathrm{cl}\,2} + r^2}}\Bigg|_{r_\odot}^{r_t} + \int_{r_\odot}^{r_t} \mathrm{d}r \frac{1}{\left(r - r_\odot\right)\sqrt{R_c^{\mathrm{cl}\,2} + r^2}} \\
&\quad \text{with } t = \frac{1}{r - r_\odot} \Rightarrow \frac{\mathrm{d}t}{\mathrm{d}r} = -\frac{1}{\left(r - r_\odot\right)^2} \Rightarrow \mathrm{d}r = -\frac{\mathrm{d}t}{t^2} \\
&= -\frac{\ln\left(r - r_\odot\right)}{\sqrt{R_c^{\mathrm{cl}\,2} + r^2}}\Bigg|_{r_\odot}^{r_t} - \int_{\infty}^{\frac{1}{r_t - r_\odot}} \mathrm{d}t \frac{1}{t\sqrt{R_c^{\mathrm{cl}\,2} + r^2}} \\
&\quad \text{with } r - r_\odot = \frac{1}{t} \Rightarrow r = r_\odot + \frac{1}{t} \\
&= -\frac{\ln\left(r - r_\odot\right)}{\sqrt{R_c^{\mathrm{cl}\,2} + r^2}}\Bigg|_{r_\odot}^{r_t} + \int_{\frac{1}{r_t - r_\odot}}^{\infty} \mathrm{d}t \frac{1}{t\sqrt{R_c^{\mathrm{cl}\,2} + \frac{1}{t^2} + \frac{2r_\odot}{t} + r_\odot^2}} \\
&= -\frac{\ln\left(r - r_\odot\right)}{\sqrt{R_c^{\mathrm{cl}\,2} + r^2}}\Bigg|_{r_\odot}^{r_t} + \int_{\frac{1}{r_t - r_\odot}}^{\infty} \mathrm{d}t \frac{1}{\sqrt{\left(R_c^{\mathrm{cl}\,2} + r_\odot^2\right) t^2 + 2r_\odot t + 1}} \qquad \text{(B.44)} \\
&\quad \text{with } \int \mathrm{d}t \frac{1}{\sqrt{at^2 + bt + c}} = \frac{1}{\sqrt{a}} \ln\left(2\sqrt{a}\sqrt{at^2 + bt + c} + 2at + b\right) \\
&= \frac{\ln\left(2\sqrt{R_c^{\mathrm{cl}\,2} + r_\odot^2}\sqrt{\left(R_c^{\mathrm{cl}\,2} + r_\odot^2\right) t^2 + 2r_\odot t + 1} + 2\left(R_c^{\mathrm{cl}\,2} + r_\odot^2\right) t + 2r_\odot\right)}{\sqrt{R_c^{\mathrm{cl}\,2} + r_\odot^2}}\Bigg|_{\frac{1}{r_t - r_\odot}}^{\infty} \\
&\quad - \frac{\ln\left(r - r_\odot\right)}{\sqrt{R_c^{\mathrm{cl}\,2} + r^2}}\Bigg|_{r_\odot}^{r_t} \\
&= -\frac{\ln\left(r_t - r_\odot\right)}{\sqrt{R_c^{\mathrm{cl}\,2} + r_t^2}} + \frac{\ln\left(r - r_\odot\right)}{\sqrt{R_c^{\mathrm{cl}\,2} + r^2}}\Bigg|_{r=r_\odot} \\
&\quad + \frac{\ln\left(2\sqrt{R_c^{\mathrm{cl}\,2} + r_\odot^2}\sqrt{\left(R_c^{\mathrm{cl}\,2} + r_\odot^2\right) t^2 + 2r_\odot t + 1} + 2\left(R_c^{\mathrm{cl}\,2} + r_\odot^2\right) t + 2r_\odot\right)}{\sqrt{R_c^{\mathrm{cl}\,2} + r_\odot^2}}\Bigg|_{t=\infty} \\
&\quad - \frac{\ln\left(2\sqrt{R_c^{\mathrm{cl}\,2} + r_\odot^2}\sqrt{\frac{R_c^{\mathrm{cl}\,2} + r_\odot^2}{\left(r_t - r_\odot\right)^2} + \frac{2r_\odot}{r_t - r_\odot} + 1} + \frac{2\left(R_c^{\mathrm{cl}\,2} + r_\odot^2\right)}{r_t - r_\odot} + 2r_\odot\right)}{\sqrt{R_c^{\mathrm{cl}\,2} + r_\odot^2}}
\end{aligned}
$$

$$(III) = -\frac{\ln(r_t - r_\odot)}{\sqrt{R_c^{\mathrm{cl}\,2} + r_t^2}} + \frac{\ln(r - r_\odot)}{\sqrt{R_c^{\mathrm{cl}\,2} + r^2}}\Bigg|_{r=r_\odot} - \frac{\ln\left(2\frac{\sqrt{R_c^{\mathrm{cl}\,2}+r_\odot^2}\sqrt{R_c^{\mathrm{cl}\,2}+r_t^2}+R_c^{\mathrm{cl}\,2}+r_\odot r_t}{r_t - r_\odot}\right)}{\sqrt{R_c^{\mathrm{cl}\,2} + r_\odot^2}}$$
$$+ \frac{\ln\left(2\sqrt{R_c^{\mathrm{cl}\,2} + r_\odot^2}\sqrt{\left(R_c^{\mathrm{cl}\,2} + r_\odot^2\right)t^2 + 2r_\odot t + 1} + 2\left(R_c^{\mathrm{cl}\,2} + r_\odot^2\right)t + 2r_\odot\right)}{\sqrt{R_c^{\mathrm{cl}\,2} + r_\odot^2}}\Bigg|_{t=\infty}$$

Final solution for the integral

$$\begin{aligned}
\mathcal{I} = &-\frac{\ln(r_t + r_\odot)}{\sqrt{R_c^{\mathrm{cl}\,2} + r_t^2}} + \frac{\ln r_\odot}{R_c^{\mathrm{cl}}} + \frac{\ln(r_\odot - r)}{\sqrt{R_c^{\mathrm{cl}\,2} + r^2}}\Bigg|_{r=r_\odot} - \frac{\ln r_\odot}{R_c^{\mathrm{cl}}} + \frac{\ln(r_t - r_\odot)}{\sqrt{R_c^{\mathrm{cl}\,2} + r_t^2}} - \frac{\ln(r - r_\odot)}{\sqrt{R_c^{\mathrm{cl}\,2} + r^2}}\Bigg|_{r=r_\odot} \\
&- \frac{\ln\left(2\frac{\sqrt{R_c^{\mathrm{cl}\,2}+r_\odot^2}\sqrt{R_c^{\mathrm{cl}\,2}+r_t^2}+\left(R_c^{\mathrm{cl}\,2}-r_\odot r_t\right)}{r_t + r_\odot}\right)}{\sqrt{R_c^{\mathrm{cl}\,2} + r_\odot^2}} + \frac{\ln\left(2\sqrt{R_c^{\mathrm{cl}\,2} + r_\odot^2}\frac{R_c^{\mathrm{cl}}}{r_\odot} + \frac{2R_c^{\mathrm{cl}\,2}}{r_\odot}\right)}{\sqrt{R_c^{\mathrm{cl}\,2} + r_\odot^2}} \\
&- \frac{\ln\left(2\sqrt{R_c^{\mathrm{cl}\,2} + r_\odot^2}\frac{R_c^{\mathrm{cl}}}{r_\odot} + \frac{2R_c^{\mathrm{cl}\,2}}{r_\odot}\right)}{\sqrt{R_c^{\mathrm{cl}\,2} + r_\odot^2}} + \frac{\ln\left(2\frac{\sqrt{R_c^{\mathrm{cl}\,2}+r_\odot^2}\sqrt{R_c^{\mathrm{cl}\,2}+r_t^2}+R_c^{\mathrm{cl}\,2}+r_\odot r_t}{r_t - r_\odot}\right)}{\sqrt{R_c^{\mathrm{cl}\,2} + r_\odot^2}} \\
&+ \frac{\ln\left(2\sqrt{\left(R_c^{\mathrm{cl}\,2} + r_\odot^2\right)}\sqrt{\left(R_c^{\mathrm{cl}\,2} + r_\odot^2\right)t^2 - 2r_\odot t + 1} + 2\left(R_c^{\mathrm{cl}\,2} + r_\odot^2\right)t - 2r_\odot\right)}{\sqrt{\left(R_c^{\mathrm{cl}\,2} + r_\odot^2\right)}}\Bigg|_{t=\infty} \\
&- \frac{\ln\left(2\sqrt{R_c^{\mathrm{cl}\,2} + r_\odot^2}\sqrt{\left(R_c^{\mathrm{cl}\,2} + r_\odot^2\right)t^2 + 2r_\odot t + 1} + 2\left(R_c^{\mathrm{cl}\,2} + r_\odot^2\right)t + 2r_\odot\right)}{\sqrt{R_c^{\mathrm{cl}\,2} + r_\odot^2}}\Bigg|_{t=\infty} \qquad \text{(B.45)} \\
= &-\frac{\ln(r_t + r_\odot)}{\sqrt{R_c^{\mathrm{cl}\,2} + r_t^2}} + \frac{\ln(r_t - r_\odot)}{\sqrt{R_c^{\mathrm{cl}\,2} + r_t^2}} - \frac{\ln\left(2\frac{\sqrt{R_c^{\mathrm{cl}\,2}+r_\odot^2}\sqrt{R_c^{\mathrm{cl}\,2}+r_t^2}+\left(R_c^{\mathrm{cl}\,2}-r_\odot r_t\right)}{r_t + r_\odot}\right)}{\sqrt{R_c^{\mathrm{cl}\,2} + r_\odot^2}} \\
&+ \frac{\ln\left(2\frac{\sqrt{R_c^{\mathrm{cl}\,2}+r_\odot^2}\sqrt{R_c^{\mathrm{cl}\,2}+r_t^2}+R_c^{\mathrm{cl}\,2}+r_\odot r_t}{r_t - r_\odot}\right)}{\sqrt{R_c^{\mathrm{cl}\,2} + r_\odot^2}} \\
= &\frac{1}{\sqrt{R_c^{\mathrm{cl}\,2} + r_t^2}}\left\{\ln\frac{r_t - r_\odot}{r_t + r_\odot} - \ln\left(2\frac{\sqrt{R_c^{\mathrm{cl}\,2} + r_\odot^2}\sqrt{R_c^{\mathrm{cl}\,2} + r_t^2} + R_c^{\mathrm{cl}\,2} - r_\odot r_t}{r_t + r_\odot}\right)\right. \\
&\left. + \ln\left(2\frac{\sqrt{R_c^{\mathrm{cl}\,2} + r_\odot^2}\sqrt{R_c^{\mathrm{cl}\,2} + r_t^2} + R_c^{\mathrm{cl}\,2} + r_\odot r_t}{r_t - r_\odot}\right)\right\}
\end{aligned}$$

$$\mathcal{I} = \frac{1}{\sqrt{{R_c^{\rm cl}}^2 + r_t^2}} \ln \frac{\sqrt{{R_c^{\rm cl}}^2 + r_\odot^2}\sqrt{{R_c^{\rm cl}}^2 + r_t^2} + {R_c^{\rm cl}}^2 + r_\odot r_t}{\sqrt{{R_c^{\rm cl}}^2 + r_\odot^2}\sqrt{{R_c^{\rm cl}}^2 + r_t^2} + {R_c^{\rm cl}}^2 - r_\odot r_t}$$

$$= \frac{1}{\sqrt{{R_c^{\rm cl}}^2 + r_t^2}} \ln \left(1 + \frac{2 r_\odot r_t}{\sqrt{{R_c^{\rm cl}}^2 + r_\odot^2}\sqrt{{R_c^{\rm cl}}^2 + r_t^2} + {R_c^{\rm cl}}^2 - r_\odot r_t} \right)$$

Appendix C

Moore-Profile

1. The normalisation constant for the density profile can be calculated by integrating the density profile over the volume of the dark matter halo and solving the resulting equation for the normalisation constant.

$$
\begin{aligned}
M_H &= \int d^3\vec{r}\, n_H(r) M_X \\
&\quad \text{with } n_H(r) = \frac{N_0 r_s^{\frac{3}{2}}}{r^{\frac{3}{2}}\left(1+\left(\frac{r}{r_s}\right)^{\frac{3}{2}}\right)} \\
&= \int d^3\vec{r}\, \frac{N_0 M_X r_s^{\frac{3}{2}}}{r^{\frac{3}{2}}\left(1+\left(\frac{r}{r_s}\right)^{\frac{3}{2}}\right)} \\
&= 4\pi N_0 M_X r_s^{\frac{3}{2}} \int_0^{r_t} \mathrm{d}r\, \frac{\sqrt{r}}{1+\left(\frac{r}{r_s}\right)^{\frac{3}{2}}} \qquad \text{(C.1)} \\
&\quad \text{with } x = \left(\frac{r}{r_s}\right)^{\frac{3}{2}} \Rightarrow \mathrm{d}r = \frac{2}{3}\frac{r_s^{\frac{3}{2}}}{\sqrt{r}}\mathrm{d}x \\
&= \frac{8\pi}{3} N_0 M_X r_s^3 \int_0^{\left(\frac{r_t}{r_s}\right)^{\frac{3}{2}}} \mathrm{d}x\, \frac{1}{1+x} \\
&= \frac{8\pi}{3} N_0 M_X r_s^3 \ln\left(1+\left(\frac{r_t}{r_s}\right)^{\frac{3}{2}}\right) \\
\Rightarrow N_0 &= \frac{3M_H}{8\pi M_X r_s^3 \ln\left(1+\left(\frac{r_t}{r_s}\right)^{\frac{3}{2}}\right)}
\end{aligned}
$$

For $r_t \gg r_s$ this exact result can be slightly simplified. This approximation does not eliminate any of the parameters and only slightly decreases the computational

complexity.

$$
\begin{aligned}
N_0 &= \frac{3M_H}{8\pi M_X r_s^3 \ln\left(1+\left(\frac{r_t}{r_s}\right)^{\frac{3}{2}}\right)} \\
&\quad \text{with } \ln\left(1+\left(\frac{r_t}{r_s}\right)^{\frac{3}{2}}\right) \approx \ln\left(\frac{r_t}{r_s}\right)^{\frac{3}{2}} = \frac{3}{2}\ln\frac{r_t}{r_s} \\
&\approx \frac{M_H}{4\pi M_X r_s^3 \ln\frac{r_t}{r_s}}
\end{aligned}
\tag{C.2}
$$

2. A solution for the decay flux from the smooth DM component can now be derived by solving the spatial integral over the normalised number density in the following equation.

$$
\begin{aligned}
\mathcal{F} &= 2\frac{\mathrm{d}N}{\mathrm{d}E}\Gamma_X \int \mathrm{d}^3\vec{r}\,\frac{n_H(r)}{4\pi\left|\vec{r}-\vec{r}_\odot\right|^2} \\
&\quad \text{with } n_H(r) = \frac{N_0 r_s^3}{r^{\frac{3}{2}}\left(r^{\frac{3}{2}}+r_s^{\frac{3}{2}}\right)} \\
&= \frac{1}{2\pi}\frac{\mathrm{d}N}{\mathrm{d}E}\Gamma_X \int \mathrm{d}^3\vec{r}\,\frac{N_0 r_s^3}{\left(r^2+r_\odot^2-2rr_\odot\cos\theta\right) r^{\frac{3}{2}}\left(r^{\frac{3}{2}}+r_s^{\frac{3}{2}}\right)} \\
&= \frac{\mathrm{d}N}{\mathrm{d}E}\Gamma_X N_0 r_s^3 \int_0^{r_t}\mathrm{d}r \int_0^{\pi}\mathrm{d}\theta\,\frac{\sqrt{r}\sin\theta}{\left(r^2+r_\odot^2-2rr_\odot\cos\theta\right)\left(r^{\frac{3}{2}}+r_s^{\frac{3}{2}}\right)} \\
&= \frac{\mathrm{d}N}{\mathrm{d}E}\Gamma_X N_0 r_s^3 \int_0^{r_t}\mathrm{d}r \int_{-1}^{1}\mathrm{d}x\,\frac{\sqrt{r}}{\left(r^2+r_\odot^2-2rr_\odot x\right)\left(r^{\frac{3}{2}}+r_s^{\frac{3}{2}}\right)} \\
&\quad \text{with } \int_{-1}^{1}\mathrm{d}x\,\frac{1}{r^2+r_\odot^2-2rr_\odot x} = \frac{1}{rr_\odot}\ln\frac{r+r_\odot}{|r-r_\odot|} \\
&= \frac{\mathrm{d}N}{\mathrm{d}E}\Gamma_X N_0 \frac{r_s^3}{r_\odot}\int_0^{r_t}\mathrm{d}r\,\ln\frac{r+r_\odot}{|r-r_\odot|}\,\frac{1}{\sqrt{r}\left(r^{\frac{3}{2}}+r_s^{\frac{3}{2}}\right)}
\end{aligned}
\tag{C.3}
$$

The integration over the two angular parameters can be solved by applying basic techniques but the radial integral cannot be solved exactly.

3. The annihilation flux from the smooth DM component is calculated similar to the decay flux by integration of the square of the number density over the volume of the halo.

$$
\begin{aligned}
\mathcal{F} &= 2\frac{\mathrm{d}N}{\mathrm{d}E}\langle\sigma v\rangle \int \mathrm{d}^3\vec{r}\,\frac{n_H^2(r)}{4\pi\left|\vec{r}-\vec{r}_\odot\right|^2} \\
&\quad \text{with } n_H(r) = \frac{N_0 r_s^3}{r^{\frac{3}{2}}\left(r^{\frac{3}{2}}+r_s^{\frac{3}{2}}\right)} \\
&= \frac{1}{2\pi}\frac{\mathrm{d}N}{\mathrm{d}E}\langle\sigma v\rangle \int \mathrm{d}^3\vec{r}\,\frac{N_0^2 r_s^6}{\left(r^2+r_\odot^2-2rr_\odot\cos\theta\right) r^3\left(r^{\frac{3}{2}}+r_s^{\frac{3}{2}}\right)^2}
\end{aligned}
\tag{C.4}
$$

$$
\begin{aligned}
\mathcal{F} &= \frac{\mathrm{d}N}{\mathrm{d}E}\langle\sigma v\rangle N_0^2 r_s^6 \int_0^{r_t} \mathrm{d}r \int_0^{\pi} \mathrm{d}\theta \, \frac{\sin\theta}{r\left(r^2 + r_\odot^2 - 2rr_\odot\cos\theta\right)\left(r^{\frac{3}{2}} + r_s^{\frac{3}{2}}\right)^2} \\
&= \frac{\mathrm{d}N}{\mathrm{d}E}\langle\sigma v\rangle N_0^2 \int_0^{r_t} \mathrm{d}r \int_{-1}^{1} \mathrm{d}x \, \frac{1}{r\left(r^2 + r_\odot^2 - 2rr_\odot x\right)\left(r^{\frac{3}{2}} + r_s^{\frac{3}{2}}\right)^2} \\
&\quad \text{with } \int_{-1}^{1} \mathrm{d}x \, \frac{1}{r^2 + r_\odot^2 - 2rr_\odot x} = \frac{1}{rr_\odot} \ln\frac{r + r_\odot}{|r - r_\odot|} \\
&= \frac{\mathrm{d}N}{\mathrm{d}E}\langle\sigma v\rangle N_0^2 \frac{r_s^6}{r_\odot} \int_0^{r_t} \mathrm{d}r \, \frac{1}{r^2\left(r^{\frac{3}{2}} + r_s^{\frac{3}{2}}\right)^2} \ln\frac{r + r_\odot}{|r - r_\odot|}
\end{aligned}
$$

As for the decay flux the angular integrals can be solved but the radial integral does not have a closed form.

4. For numerical simulations it is more convenient to simulate the mass of a substructure than its tidal radius. Therefore it is necessary to normalise the subclump density profile integrating the subclump profile over the volume of the subclump.

$$
\begin{aligned}
M_{\mathrm{cl}} &= \int \mathrm{d}^3\vec{d} \, M_X n_X(d, r) \\
&\quad \text{with } n_X(d, r) = \frac{d_t^{\frac{3}{2}}\left(d_t^{\frac{3}{2}} + d_s^{\frac{3}{2}}\right)}{d^{\frac{3}{2}}\left(d^{\frac{3}{2}} + d_s^{\frac{3}{2}}\right)} n_H(r) \\
&= \int \mathrm{d}^3\vec{d} \, M_X \frac{d_t^{\frac{3}{2}}\left(d_t^{\frac{3}{2}} + d_s^{\frac{3}{2}}\right)}{d^{\frac{3}{2}}\left(d^{\frac{3}{2}} + d_s^{\frac{3}{2}}\right)} n_H(r) \\
&= 4\pi M_X n_H(r) \frac{d_t^{\frac{3}{2}}\left(d_t^{\frac{3}{2}} + d_s^{\frac{3}{2}}\right)}{d_s^{\frac{3}{2}}} \int_0^{d_t} \mathrm{d}d \, \frac{\sqrt{d}}{1 + \left(\frac{d}{d_s}\right)^{\frac{3}{2}}} \qquad \text{(C.5)} \\
&\quad \text{with } x = \left(\frac{d}{d_s}\right)^{\frac{3}{2}} \Rightarrow \mathrm{d}d = \frac{2}{3}\frac{d_s^{\frac{3}{2}}}{\sqrt{d}}\mathrm{d}x \\
&= \frac{8\pi}{3} M_X n_H(r) d_t^{\frac{3}{2}}\left(d_t^{\frac{3}{2}} + d_s^{\frac{3}{2}}\right) \int_0^{\left(\frac{d_t}{d_s}\right)^{\frac{3}{2}}} \mathrm{d}x \, \frac{1}{1 + x} \\
&= \frac{8\pi}{3} M_X n_H(r) d_t^{\frac{3}{2}}\left(d_t^{\frac{3}{2}} + d_s^{\frac{3}{2}}\right) \ln\left(1 + \left(\frac{d_t}{d_s}\right)^{\frac{3}{2}}\right)
\end{aligned}
$$

5. By integrating the square of the subclump number distribution over the volume of the subclump the annihilation rate inside a subclump can be derived.

$$
\begin{aligned}
\mathcal{R}(r, M_{\mathrm{cl}}) &= \langle\sigma v\rangle \int \mathrm{d}^3\vec{d} \, n_X^2(d, r) \\
&\quad \text{with } n_X(d, r) = \frac{d_t^{\frac{3}{2}}\left(d_t^{\frac{3}{2}} + d_s^{\frac{3}{2}}\right)}{d^{\frac{3}{2}}\left(d^{\frac{3}{2}} + d_s^{\frac{3}{2}}\right)} n_H(r) \qquad \text{(C.6)} \\
&= \langle\sigma v\rangle \int \mathrm{d}\vec{d} \, \frac{d_t^3\left(d_t^{\frac{3}{2}} + d_s^{\frac{3}{2}}\right)^2}{d^3\left(d^{\frac{3}{2}} + d_s^{\frac{3}{2}}\right)^2} n_H(r)
\end{aligned}
$$

$$\mathcal{R}(r, M_{\rm cl}) = 4\pi\langle\sigma v\rangle n_H^2(r) d_t^3 \left(d_t^{\frac{3}{2}} + d_s^{\frac{3}{2}}\right)^2 \left\{ \int_0^{d_c} \mathrm{d}d \frac{d^2}{d_c^3 \left(d_c^{\frac{3}{2}} + d_s^{\frac{3}{2}}\right)^2} + \int_{d_c}^{d_t} \mathrm{d}d \frac{1}{d\left(d^{\frac{3}{2}} + d_s^{\frac{3}{2}}\right)^2} \right\}$$

$$\text{with } \int_{d_c}^{d_t} \mathrm{d}d \frac{1}{d\left(d^{\frac{3}{2}} + d_s^{\frac{3}{2}}\right)^2} = \frac{2}{3}\left(3\ln\frac{d_t}{d_c} - \ln\frac{d_t^{\frac{3}{2}} + d_s^{\frac{3}{2}}}{d_c^{\frac{3}{2}} + d_s^{\frac{3}{2}}} + \frac{d_s^{\frac{3}{2}}}{d_t^{\frac{3}{2}} + d_s^{\frac{3}{2}}} - \frac{d_s^{\frac{3}{2}}}{d_c^{\frac{3}{2}} + d_s^{\frac{3}{2}}}\right)$$

$$= \frac{4\pi}{3}\langle\sigma v\rangle n_H^2(r) \frac{d_t^3 \left(d_t^{\frac{3}{2}} + d_s^{\frac{3}{2}}\right)^2}{d_s^3} \left\{ 2\ln\frac{d_t^3 \left(d_c^{\frac{3}{2}} + d_s^{\frac{3}{2}}\right)}{d_c^{\frac{3}{2}} \left(d_t^{\frac{3}{2}} + d_s^{\frac{3}{2}}\right)} + \frac{2d_s^{\frac{3}{2}}}{d_t^{\frac{3}{2}} + d_s^{\frac{3}{2}}} - \frac{2d_c^{\frac{3}{2}} d_s^{\frac{3}{2}} + d_s^3}{\left(d_c^{\frac{3}{2}} + d_s^{\frac{3}{2}}\right)^2} \right\}$$

6. The subclump distribution is independent of the profile of the subclumps and the calculations to normalise the subclump distribution are identical to those performed for the NFW-profile. For a detailed derivation please refer to step 6 from Appendix B.

7. Finally, the annihilation flux from the clumped DM component is calculated.

$$\begin{aligned}
\mathcal{F} &= \frac{\mathrm{d}N}{\mathrm{d}E} \int \mathrm{d}^3\vec{r} \frac{1}{2\pi\left|\vec{r} - \vec{r}_\odot\right|^2} \int_{M_{\rm min}}^{M_{\rm max}} \mathrm{d}M_{\rm cl} n_{\rm cl}(r, M_{\rm cl}) \mathcal{R}(r, M_{\rm cl}) \\
&= \frac{\mathrm{d}N}{\mathrm{d}E} \int_0^{r_t} \mathrm{d}r \int_0^{\pi} \mathrm{d}\theta \frac{r^2 \sin\theta}{r^2 + r_\odot^2 - 2rr_\odot\cos\theta} \int_0^{\eta M_H} \mathrm{d}M_{\rm cl} n_{\rm cl}(r, M_{\rm cl}) \mathcal{R}(r, M_{\rm cl}) \\
&= \frac{\mathrm{d}N}{\mathrm{d}E} \int_0^{r_t} \mathrm{d}r \int_{-1}^{1} \mathrm{d}x \frac{r^2}{r^2 + r_\odot^2 - 2rr_\odot x} \int_0^{\eta M_H} \mathrm{d}M_{\rm cl}\, n_{\rm cl}(r, M_{\rm cl}) \mathcal{R}(r, M_{\rm cl}) \qquad \text{(C.7)} \\
&\quad \text{with } \int_{-1}^{1} \mathrm{d}x \frac{1}{r^2 + r_\odot^2 - 2rr_\odot x} = \frac{1}{rr_\odot} \ln\frac{r + r_\odot}{|r - r_\odot|} \\
&= \frac{\mathrm{d}N}{\mathrm{d}E} \frac{1}{r_\odot} \int_0^{r_t} \mathrm{d}r\, r \ln\frac{r + r_\odot}{|r - r_\odot|} \int_0^{\eta M_H} \mathrm{d}M_{\rm cl}\, n_{\rm cl}(r, M_{\rm cl}) \mathcal{R}(r, M_{\rm cl}) \\
&\quad \text{with } n_{\rm cl}(r, M_{\rm cl}) = n_{\rm cl}^0 \left(\frac{M_H}{M_{\rm cl}}\right)^{\alpha} \left(1 + \left(\frac{r}{R_c^{\rm cl}}\right)^2\right)^{-\frac{3}{2}}
\end{aligned}$$

Appendix D

Constant Density Subclumps

All subclumps have a constant density core that is arbitrarily chosen to be equal to a fraction ν of the density of the Sun.

$$\rho_X = \nu\rho_\odot \tag{D.1}$$

$$n_X = \frac{\rho_X}{M_X} = \nu\frac{\rho_\odot}{M_X} \tag{D.2}$$

The behaviour of the unclumped component of the dark matter halo is not affected by the assumption on the clumped component. Therefore only the calculations for the clumped component are of interest.
1. As previously mentioned it is more convenient to simulate the mass of a subclump than its core radius. Therefore the core radius of the i-th subclump is derived from the equation for the cluster. Due to the constant density a simple result for the core radius is found.

$$\begin{aligned} M_{\mathrm{cl}}^{(i)} &= \int \mathrm{d}^3\vec{d}\,\rho_X \\ &\quad \text{with } \rho_X = \nu\rho_\odot \\ &= \int \mathrm{d}^3\vec{d}\,\nu\rho_\odot \\ &= 4\pi\nu\rho_\odot \int_0^{d_{\mathrm{cl}}^{(i)}} \mathrm{d}d\, d^2 \\ &= \frac{4\pi}{3}\nu\rho_\odot {d_{\mathrm{cl}}^{(i)}}^3 \\ \Rightarrow d_{\mathrm{cl}}^{(i)} &= \sqrt[3]{\frac{3M_{\mathrm{cl}}^{(i)}}{4\pi\nu\rho_\odot}} \end{aligned} \tag{D.3}$$

2. With the core radius and therefore the volume of the subclump known it is easy to calculate the annihilation rate in the i-the subclump. The annihilation rate for the subclump system of a galaxy can trivially be found by adding the contributions

of all subclumps.

$$
\begin{aligned}
\mathcal{R}\Big(M_{\rm cl}^{(i)}\Big) &= \langle\sigma v\rangle \int \mathrm{d}^3\vec{d}\, n_X^2 \\
&\quad \text{with } n_X = \nu\frac{\rho_\odot}{M_X} \\
&= \langle\sigma v\rangle \int \mathrm{d}^3\vec{d}\,\frac{\nu^2\rho_\odot^2}{M_X^2} \\
&= 4\pi\langle\sigma v\rangle\frac{\nu^2\rho_\odot^2}{M_X^2}\int_0^{d_{\rm cl}^{(i)}} \mathrm{d}d\, d^2 \\
&= \frac{4\pi}{3}\langle\sigma v\rangle\frac{\nu^2\rho_\odot^2}{M_X^2}{d_{\rm cl}^{(i)}}^3 \\
&\quad \text{with } d_{\rm cl}^{(i)} = \sqrt[3]{\frac{3M_{\rm cl}^{(i)}}{4\pi\nu\rho_\odot}} \\
&= \langle\sigma v\rangle\frac{\nu\rho_\odot M_{\rm cl}^{(i)}}{M_X^2} \\
\Rightarrow \mathcal{R}_{\rm tot}\Big(M_{\rm cl}^{(i)}\Big) &= \langle\sigma v\rangle\frac{\nu\rho_\odot}{M_X^2}\sum_i M_{\rm cl}^{(i)}
\end{aligned}
\tag{D.4}
$$

3. At last, the annihilation flux from a pointlike subclump distribution with constant density core is derived.

$$
\begin{aligned}
\mathcal{F} &= \frac{\mathrm{d}N}{\mathrm{d}E}\int \mathrm{d}^3\vec{r}\,\frac{1}{2\pi\left|\vec{r}-\vec{r}_\odot\right|^2} n_{\rm cl}(r_i)\mathcal{R}_{\rm tot}\Big(M_{\rm cl}^{(i)}\Big) \\
&\quad \text{with } \mathcal{R}_{\rm tot}\Big(M_{\rm cl}^{(i)}\Big) = \langle\sigma v\rangle\frac{\nu\rho_\odot}{M_X^2}\sum_i M_{\rm cl}^{(i)} \\
&\qquad\qquad n_{\rm cl}(r_i) = \delta(\vec{r}-\vec{r}_i) \\
&= \frac{\mathrm{d}N}{\mathrm{d}E}\int \mathrm{d}^3\vec{r}\,\frac{1}{2\pi\left|\vec{r}-\vec{r}_\odot\right|^2}\langle\sigma v\rangle\frac{\nu\rho_\odot}{M_X^2}\sum_i M_{\rm cl}^{(i)}\delta(\vec{r}-\vec{r}_i) \\
&= \frac{1}{2\pi}\frac{\mathrm{d}N}{\mathrm{d}E}\langle\sigma v\rangle\frac{\nu\rho_\odot}{M_X^2}\sum_i M_{\rm cl}^{(i)}\int \mathrm{d}^3\vec{r}\,\frac{\delta(\vec{r}-\vec{r}_i)}{\left|\vec{r}-\vec{r}_\odot\right|^2} \\
&= \frac{1}{2\pi}\frac{\mathrm{d}N}{\mathrm{d}E}\langle\sigma v\rangle\frac{\nu\rho_\odot}{M_X^2}\sum_i \frac{M_{\rm cl}^{(i)}}{\left|\vec{r}_i-\vec{r}_\odot\right|^2} \\
&\quad \text{with } r_i = \vec{r}_i - \vec{r}_\odot \\
&= \frac{1}{2\pi}\frac{\mathrm{d}N}{\mathrm{d}E}\langle\sigma v\rangle\frac{\nu\rho_\odot}{M_X^2}\sum_i \frac{M_{\rm cl}^{(i)}}{r_i^2}
\end{aligned}
\tag{D.5}
$$

References

[1] A.A. Watson, Ultra High Energy Cosmic Rays: The present position and the need for mass composition measurements, in: Thinking, Observing and Mining the Universe, G. Miele and G. Longo (eds.), World Scientific Publ. Co., Singapore 2004, p. 277

[2] M.T. Dova, M.E. Mancenido, A.G. Mariazzi, T.P. McCauley, A.A. Watson, New constraints on the mass composition of cosmic rays above 10^{17} eV from Volcano Ranch measurements, Astropart. Phys. 21, 597 (2004)

[3] A.V. Olinto, Highest Energy Cosmic Rays, AIP Conference Proceedings 745, 48 (2005)

[4] J.F. Navarro, C.S. Frenk, S.D.M. White, Mon. Not. R. Astron. Soc. 275, 720-740 (1995);
Astrophys. J. 462, 563-575 (1996)

[5] B. Moore, C. Calceano-Rodan, J. Stadel, T. Quinn, G. Lake, S. Ghigna, F. Governato, Dark matter in Draco and the Local Group: Implications for direct detection experiments, Phys. Rev. D 64, 063508

[6] C.J. Peterson, I.R. King, The structure of stars. VI. Observed radii and structural parameters in globular clusters, Astron. J. 80, 427 (1975)

[7] S. Ghigna, B. Moore, G. Lake, T. Quinn, J. Stadel, Density profiles and substructure of dark matter halos: converging results at ultra-high numerical resolution, Astrophys. J. 544, 616-628 (2000)

[8] P. Colin, A. Klypin, O. Valenzuela, S. Gottlöber, Dwarf dark matter halos, ASPN 327, 28 (2004)

[9] Y. Ascasibar, G. Yepes, S. Gottlöber, V. Müller, On the physical origin of dark matter density profiles, Mon. Not. R. Astron. Soc. 352, 1109 (2004)

[10] S. Kazantzidis, L. Mayer, C. Mastropietro, J. Diemand, J. Stadel, B. Moore, Density Profiles Of Cold Dark Matter Substructure: Implications For The Missing Satellites Problem, Astrophys. J. 608, 663 (2004)

[11] S. LeBohec *et al.*, Search for a WIMP annihilation signature in the core of the globular cluster M15, Proceedings of the 28th International Cosmic Ray Conference, 2521 (2003)

[12] A. Tasitsiomi, J. Gaskins, A.V. Olinto, Gamma-ray and synchrotron emission from neutralino annihilation in the Large Magellanic Cloud, Astropart. Phys. 21, 637 (2004)

[13] E. Hayashi, J.F. Navarro, J.E. Taylor, J. Stadel, T. Quinn, Astrophys. J. 584, 541 (2003)

[14] L. Bergström, Dark Matter Constituents, Nucl. Phys. Proc. Suppl. 138, 123 (2005)

[15] M. Oguri, K. Takahashi, H. Ohno, K. Kotake, Decaying Cold Dark Matter and the Evolution of the Cluster Abundance, Astrophys. J. 597, 645 (2003)

[16] F.J. Sanchez-Salcedo, Unstable Cold Dark Matter and the Cuspy Halo Problem in Dwarf Galaxies, Astrophys. J. 591, L107 (2003)

[17] V.V. Vassiliev *et al.*, Search for TeV annihilation radiation from supersymmetric dark matter in nearby galaxies, Proceedings of the 28th International Cosmic Ray Conference, 2679 (2003)

[18] K. Kosack *et al.*, TeV Observations of the Galactic Center, Proceedings of the 28th International Cosmic Ray Conference, 2679 (2003)

[19] K. Greisen, Phys. Rev. Lett. 16, 748 (1966)
G.T. Zatsepin, V.A. Kuzmin, JETP Lett. 4, 78 (1966)

[20] J.B. Hartle, Gravity - An Introduction to Einstein's General Relativity, Addison Wesley, (2003)

[21] W.E. Harris, A Catalog of parameters for Globular Clusters in the Milky Way, Astron. J. 112, 1487 (1996)

[22] G. Piotto *et al.*, HST Observation of High-Density Globular Clusters, 23rd meeting of the IAU, Joint Discussion 15, 32 (1997)

[23] P. Cote, D.E. McLaughlin, J.D. Cohen, J.P. Blakeslee, Dynamics of the Globular Cluster System Associated with M49 (NGC4472): Cluster Orbital Properties and the Distribution of Dark Matter, Astrophys. J. 591, 850 (2003)

[24] R.G. Gratton, E. Carretta, G. Clementini, Distances and Ages of Globular Clusters using HIPPARCOS Parallaxes of Local Subdwarfs, Post-Hipparcos cosmic candles, Boston: Kluwer Academic Publisher, 89 (1999)

[25] C.J. Walcher, R.P. van der Marel, D. McLaughlin, H.-W. Rix, T. Böker, N. Häring, L.C. Ho, M. Sarzi, J.C. Shields, Masses of Star Clusters in the Nuclei of Bulgeless Spiral Galaxies, Astrophys. J. 618, 237 (2005)

[26] B. Willman *et al.*, A New Milky Way Companion: Unusual Globular Cluster or Extreme Dwarf Satellite?, Astron. J. 129, 2692 (2005)

[27] G. Cresci, L. Vanzi, M. Sauvage, The star cluster population of NGC 5253, Astron. Astroph. 433, 447 (2005)

[28] S. Mashchenko, A. Sills, Globular Clusters with Dark Matter Halos I. Initial Relaxation, Astrophys. J. 619, 243 (2005)

[29] S. Mashchenko, A. Sills, Globular Clusters with Dark Matter Halos II. Evolution in a Tidal-Field, Astrophys. J. 619, 258 (2005)

[30] S.S. Larsen *et al.*, Structure and Mass of a Young Globular Cluster in NGC 6946, Astrophys. J. 556, 801 (2001)

[31] T.B. Williams, N.A. Bahcall, Brightness, density and color profiles of Three Globular Clusters: NGC6440, 6541, and 7099, Astrophys. J. 232, 754 (1979)

[32] T. Böker, S. Laine, R.P. van der Marel, M. Sarzi, H.-W. Rix, L.C. Ho, J.C. Shields, A Hubble Space Telescope Census of Nuclear Star Clusters in Late-Type Spiral Galaxies. I. Observations and Image Analysis, Astron. J. 123, 1389 (2002)

[33] T. Böker, M. Sarzi, D.E. McLaughlin, R.P. van der Marel, H.-W. Rix, L.C. Ho, J.C. Shields, A Hubble Space Telescope Census of Nuclear Star Clusters in Late-Type Spiral Galaxies. II. Cluster Sizes and Structural Parameter Correlations, Astron. J. 127, 105 (2004)

[34] R. Genzel, The Nuclear Star Cluster and the Massive Black Hole at the Centre of the Milky Way, AGM Abstracts, Abstracts of Talks and Posters presented at the International Conference of the AG at Heidelberg 2000, talk #16 (2000)

[35] H. Baumgardt, J. Makino, P. Hut, Which Globular Clusters contain Intermediate-Mass Black Holes?, Astrophys. J. 620, 238 (2005)

[36] P. Blasi, R. Dick, E.W. Kolb, Ultra-high energy cosmic rays from annihilation of superheavy dark matter, Astropart. Phys., 18, 57 (2002)

[37] R. Dick, K.M. Hopp, K.E. Wunderle, Ultrahigh energy cosmic rays from collisional annihlation revisited, Can. J. Phys. 83, 1141 (2005)

[38] M. Abramowitz, I.S. Stegun, Handbook of Mathematical Functions, Dover Publications, Inc., seventh printing, 556 (1965)